Abstract

PIERSON, DAVID MICHAEL. Buried-Object Detection Using Time-Reversed Acoustics. (Under the direction of David Aspnes.)

The work presented here is a comprehensive study of using time reversal to detect objects located in an inhomogeneous environment using backscattered signals with an emphasis on littoral environments. Time reversal of acoustic signals in the ocean has been studied for more than two decades with the emphasis on the use of the forward scattered field. All studies share similar geometries where both the acoustical source and an adjacent array of transducers are placed in the water column. This configuration, known as a time-reversal mirror (TRM), is not practical when detecting an object that is located in a different environment than the TRM, such as beneath the ocean floor. Little work has been done to study the efficacy of a single transceiver performing the time-reversal operation on the backscattered signals from targets buried beneath the ocean floor. Here, I start by presenting the theory for such a system in both time and frequency domains for scattering by a sphere. Then by using simulations I show that time reversal of backscattered signals provides a robust method to detect targets buried in an acoustically inhomogeneous sediment using a point transceiver in the water column several meters above the sea floor. Effects of the time-reversal window (TRW) on the iterative time-reversal operation are also presented. I define a signal-to-noise ratio (SNR) that treats the return with the sphere as the signal and the return without the sphere as noise to quantify improvements to the sphere returns. I consider two different sediment models and angle of incidence to

show that the TRO operates independently of the sediment type and transceiver orientation. Theoretical analysis reveals that the time-reversal of backscattered signals converges to a subset of waveforms defined by the target and time-reversal window, not the initial pulse. Analysis further reveals that the time-reversal operator detects the sphere after only two iterations of the TRO, with more iterations enhancing the sphere return through the non-linear filtering property of the TRO. Through this work, I demonstrate that time reversal is a robust method to detect objects.

BURIED-OBJECT DETECTION USING TIME-REVERSED ACOUSTICS

BY

David Michael Pierson

A DISSERTATION SUBMITTED TO THE GRADUATE FACULTY OF
NORTH CAROLINA STATE UNIVERSITY
IN PARTIAL FULFILLMENT OF THE
REQUIREMENTS FOR THE DEGREE OF
DOCTOR OF PHILOSOPHY

DEPARTMENT OF PHYSICS

RALEIGH, NC

December 2003

APPROVED BY:

CHAIR OF ADVISORY COMMITTEE	

Biography

I was born on December 14, 1970 in Springfield, MA to Mr. and Mrs. John Pierson. I started my career in physics at the University of Missouri - St. Louis where I received a B. S. in 1992 and M. S. in 1994 where I studied the phenomenon of stochastic resonance under Dr. Frank Moss. I entered the graduate program at North Carolina State University in 1995. December 19, 2003 I completed the requirement for a Ph. D. by defending this work.

Acknowledgments

I would like to thank the following people for their support and assistance at all stages of this work. Dr. David Aspnes for his guidance, assistance, and encouragement leading to the completion of this work. Dr. Thomas Drake for his guidance, support, and experience with the near shore environment allowing me to pursue this project from the beginning. Dr. Tony Clark for his encouragement, support, and expertise with Naval operations. Mr. Kenneth Dial for his investment in a young scientist, who will forever be in his debt. Dr. Helena Mitasova for her support through the latter half of this project. My parents, grandfather, and aunt whose encouragement was needed on several occasions. And finally, my wife, Dianne, who was supportive from the beginning and never backed down while I was working on this project. She has my never-ending gratitude and love.

Table of Contents

List of Figures

List of Tables

Chapter 1

Buried Object Detection Using Time-reversed Acoustics

1.1 Introduction

Location of objects by remote sources has been the subject of the work of many people in many areas both civilian and military. The term "remote sensing" gives the impression of aerial photos, radar towers, satellites, and sonar systems on ships. But this is not that different than tracking deposition of various substances on a particular substrate. The goal is to be able to accurately measure some quantity using any method appropriate for the object being located and the environment in which the object is located. For example, use of echo location may not be the best option to find an airplane 50 km away since sound does not propagate efficiently in the atmosphere.

For the ocean environment there are two techniques available, one is based on optical methods [1] and the other on acoustical methods. For example, the optical system developed by Moore et. al. [2], [3], uses a 532 nm Nd:YAG laser to illuminate the seafloor and a camera to record the image. Since it uses a laser the spatial (up to 0.6 mm at 10 m) and depth resolution (up to 10 cm at 10 m) is high resulting in high quality maps of the seafloor. The primary disadvantage of this and any optical

system is it cannot penetrate the seafloor to find buried objects. This leads to the other approach for the ocean environment, which is based on acoustics. There are three regions where an object (the terms *object* and *target* are used interchangeably throughout the literature) can be located: within the water column, on the ocean floor, or beneath the ocean floor. For a target in the water column, the problem is relatively easy since the target and the source are in the same environment. This does not mean that the problem is trivial since the water column can vary greatly in depth and range [4], [5]. Since the variation in the acoustic properties of the water column varies more rapidly in depth than in range, acoustical systems are used to locate targets from 1 m to several hundred kilometers. When an object is located on the seafloor, it poses a similar problem since it is still visible to the detector in the water column. To make the target more difficult to find, it is usually camouflaged to look like a rock or is made to blend into the surrounding seafloor. Also the object can become buried by the entrained sediment and scour effects leading to the next region of interest and the main focus of this study.

Acoustic location systems have been studied and used with some success for targets buried beneath the ocean floor [6]. Marine mammals are still the most effective method [7], [8]. Of the man-made systems, two are widely used and can locate buried objects remotely are the chirp sonar and the side-scan sonar systems. Chirp sonar sends a wave packet composed of frequencies ranging from 1 Hz to 1 MHz at normal incidence to the seafloor and gives a detailed picture of the underlying volume. If the system is not in direct contact with the seafloor, it can scan an area approximately 5.7 km^2 in a day assuming an average ship speed of 9.3 km/h and 5 km scan lines separated by 100 m operating eight hours in that day. If the system is in direct physical contact with the seafloor the scan rate will be much slower as the device is prone to getting buried in the sediment or damaged by the seafloor. With either configuration the main difficulty in rapidly mapping the seafloor is that only one line can be scanned at a time.

In theory it is possible to use chirp sonar to locate buried objects. However, the

problems in using chirp sonar for target detection and location make this impractical. These are:

- The seabed attenuates the signal as a function of frequency limiting the resolution as a function of depth. This makes chirp sonar ineffective for locating small objects.
- Chirp sonar is a *look-down* approach, meaning that the sound wave intercepts the seafloor at normal incidence. The result is that the area is mapped by line scans, which can take several days to cover an area of more than ten square kilometers.
- Typical chirp sonar systems cannot selectively tune the output signal. If there is a target of interest, another system must be used to focus on it.

Hence a chirp sonar system is not the best platform to detect buried objects, especially when the time to map a large area is critical.

Side-scan sonar is a different type of sonar system. As the name suggests, it looks out to the sides and maps the seafloor. Most side-scan sonar systems use a smaller range of frequencies (100 kHz to 500 kHz) to image the seafloor [9]. The resolution is about 1.5 cm for 100 kHz and 0.3 cm for 500 kHz assuming a mean sound speed in water of 1520 m/s. Since it is side looking the area of insonification is large. The optical analog is known as dark-field microscopy where the incident field illuminates the region of interest. A good parallel to imagine is a flashlight in a dark room. If you point the beam straight down, you illuminate a smaller area than if you tilt the flashlight slightly in front of you. However, like the flashlight, side-scan sonar reflects specularly from the surface and most of the energy is scattered in the forward direction.

As with any detection method that depends on waves interacting with a medium, there is a relationship between wavelength of the probing signal, resolution, and range. The smaller the wavelength the higher the resolution, which results in the detection of smaller targets. However, higher frequencies are more prone to degradation, as will be discussed, next.

The three main causes of signal degradation are geometrical spreading, attenuation from the propagating environment, and noise. Geometrical spreading comes from the inverse-distance relationship of propagation and results in a weakening of the signal, because the amplitude of the signal falls as the inverse of the distance between the source and the wavefront. There are methods available to minimize this effect, such as beam focusing and the use of solitons.

Attenuation is caused by the direct interaction of the sound field with the environment by absorption and scattering in the propagation direction by the environment. In practice, there is no way to distinguish the two causes of attenuation so it is treated as one cause. Since the environment can vary in space and time, these effects will exhibit a spatio-temporal dependence. It is generally accepted that the attenuation from the propagating environment is a function of frequency described by $e^{-\alpha|f|}$ where α is a positive constant and f is the frequency [5], [4]. For example, attenuation in seawater has a range from 10^{-2} to 10^{2} dB/km over the frequency range 10 Hz to 100 kHz. Obviously, lower frequencies propagate much farther than higher frequencies, but at the cost of lower resolution. To compensate for this type of attenuation, models are used to predict these environmental effects. All models require *a priori* knowledge of the environment, which may be difficult to obtain depending on the information needed. In practice there is no method to distinguish the effects of geometrical spreading and attenuation from the environment. As a result both are considered one effect.

Noise is also present in the ocean with causes either natural or man-made. Natural causes include wind-ocean-surface, biological, and tidal interactions over differing frequency bands. Man-made noise is primarily from shipping and the occasional experiment. Even though natural and man-made noise can cover different frequency bands, in practice they are treated as one source of noise.

It has been discovered recently that under certain conditions the signal from side-scan sonar penetrates the surface of the seafloor up to a few meters [10], opening the possibility of using side-scan sonar to locate objects buried relatively near the

surface. As with any new technique there are problems to be addressed. Two of these problems are target detection and identification, both of which are studied in this work. Current techniques such as matched field processing or inversion require some *a priori* knowledge of the environment, which as stated earlier, presents a new layer of problems. One of these methods, matched field processing (MFP), uses a model to calculate the field from a source to the receiver by moving the source in the model until the field from the simulation matches what is recorded from the real source. The other method, called inversion, uses a model of the environment to negate the effects of the environment by back-propagating the recorded signal. The term *inversion* comes from matrix algebra because back-propagation of the signal from the receiver to the source is the same as multiplying the recorded signal by the inverse of the propagation matrix. Both techniques require a certain amount of prior knowledge of the environment which may not be available, and since the ocean environment is complicated, these techniques can be computationally involved.

Time reversal is another promising approach that does not depend on models of the environment nor prior knowledge of the environment [11], [12]. Time reversal takes advantage of the spatial reciprocity of the propagating medium by transmitting a signal in reverse temporal order. The important restriction is that the environment must change slowly compared to the time of propagation of the signal. Time reversal has been studied for several years for target detection within the water column [13], [14], underwater communications [15], [16], medical ultrasound [12], and toxic waste barrel location [17]. The efficacy of time reversal through random media [18], [19], [20], and how time-varying media affect time reversal [21], [22], [23], have all been studied. The basic geometry for these studies is shown in Fig. 1.1, where a source is located in some medium, either homogeneous or random, a distance away from an array of transceivers. This array does not need to be coaxial with the source or have a flat geometry, and can be located orthogonally to the source relative to the environment as long as its location and shape remain fixed. As the initial pulse propagates from the source to the time reversal mirror (TRM), the signal will be scattered within

the medium by scatterers of varying geometries and composition. When the signal reaches the TRM information about the path and scatterers is included in the time record. Since the paths are reciprocal in space, transmitting the time-reversed signal recorded by the TRM will focus the original pulse at the source location.

Time reversal has its basis in phase conjugation in which the complex field is recorded after which the complex conjugate of the field is transmitted. If the temporal part of the field is defined via complex phases $e^{i\omega t}$, phase conjugation reduces to reversing the signal in time. Phase conjugation has been studied both in acoustics [24] and optics [25], but the only similarity between the two is the end result of transmission of the phase-conjugated signal. Acoustical phase conjugation (APC) can be performed using transducers that reverse the temporal order of the received signal upon transmission. This is possible because the technology has progressed to the point where the sampling rates of current recording systems greatly exceed the frequencies of interest. In contrast optical phase conjugation (OPC) uses electromagnetic waves whose frequencies greatly exceed sampling rates possible with optical detectors. As a result, OPC must be performed in frequency space by taking advantage of the indifference of the complex conjugation of the exponential function. This is accomplished by using nonlinear terms, second order for three-wave mixing and third for four-wave mixing, of the susceptibility of the material used as the phase conjugator. Three-wave mixing (TWM) is used for forward propagation of the phase-conjugated field while four-wave mixing (FWM) is used for phase-conjugation mirrors. Since acoustical time reversal uses a time-reversal mirror, the optical analog is performed by four-wave mixing. The four waves in FWM are the incident field (E_p), the conjugate wave (E_c), and two pump waves (E_1 and E_2) that are incident on a slab of material whose third-order susceptibility can generate the conjugate field. In the case of the mirror, optimal conjugation occurs when the frequencies of the two pump fields equals the frequency of the incident field, resulting in a conjugate field that is identical to the incident field in every respect, including polarization, with the exception that the conjugate field has a wave vector anti-parallel to the incident wave

vector. This conjugate field is the time-reversed representation of the incident field. Unlike in acoustics, the optical time-reversal mirror generates fields in the forward direction away from the source.

Two points worth mentioning concerning the configuration in Fig. 1.1 are that the source and TRM are in the same medium and implications of the physical size of the TRM. The minimal requirement that the array be in surface contact with the medium in which the source/target is located poses an unnecessary constraint to the problem that has not been addressed until now. The fact that the TRM is of fixed size is not a problem unless the dimension of the array is larger than the dimension of the region it is located. A single transducer can be used to detect a target and the range of the target with improvements in resolution by using synthetic-aperture techniques. Synthetic-aperture sonar (SAS) [26] uses a single transducer or a small array of transducers in one body, which moves with respect to the target (Fig. 1.2). The sonar sends a ping at location A and receives the scattered field at a point B, which creates an aperture that is dependent on the distance traveled. Since TRMs will return the signal to the source location, in this configuration the sonar must transmit the time-reversed signal and then return to the location of the original ping before the time reversed signal arrives. Because this movement is impractical on the time scales involved, a second identical sonar system must remain at the original ping location turning the SAS to a fixed TRM. No work has been done using time reversal with a single transducer except for Draeger and Fink [27], Chambers [28], [29], and the present investigation.

The theory of time reversal has been treated on the basis of its Fourier transform of the temporal space. This has inherent problems since the time-reversal process is an operation on a windowed set of the signal, resulting in errors due to frequency cutoff. It also eliminates any insight as to how time reversal functions in the time domain. Time reversal has another effect on the backscattered signal when the operation is performed iteratively. As the signal travels through the medium, it undergoes a convolution operation with the propagating environment in the forward and then

the backscattered directions. Iteratively performing the time-reversal operation on the backscattered signal averages out the effects of the propagating medium in the backscattered return by selectively tuning to the frequencies that correspond to the impulse reponse of the acoustically strongest scatterer. However, any environmental effects left over from the first return are still present as seen by the attenuation of certain frequencies.

Here I present the theory of the time-reversal operator in the time domain and show that time reversal in the backscattered direction functions only in a finite temporal sub-space. As a result, aliasing of the signal is built into time-reversal. This point is not obvious in approaches that use the Fourier transform of the time-reversal operator [28], [29], [30]. Filtering can help to some degree, but it must be changed with each iteration of the time-reversal operator. I will also show that for any target, iterative time reversal of the backscattered signal will not reproduce the original pulse shape, but converges to a backscattered waveform with minimal environmental effects. It also does this without increasing the SNR over the temporal sampling of the return. However, it does increase the SNR for certain frequencies that are related to the field scattered from the target. This allows a limited amount of information to be obtained about the target, specifically the distance to the surface of the target and the target size. Finally, this work will show that the time-reversal procedure can be used for a target that is not on the normal axis defined by the transceiver and seafloor, demonstrating that it can be used with side-scan sonar systems.

I approach time reversal by studying the configuration consisting of a single-point transducer where the target is located in a second inhomogeneous medium, as shown in Fig. 1.3. The software package Bottom Response from Inhomogeneities and Surface Roughness (BoRIS) [31], [32], [33] is used to calculate the backscattered return of the situation in Fig. 1.3. The software was modified to allow the a target to be placed anywhere in the bottom and to use time reversal.

Finally, possible directions for further studies based on this work are discussed. These can range from improving the model, experimental verification of the present

work, and possibly to investigate the use of other models or signal improvement techniques in conjunction with time reversal to negate effects that can cause problems if the time-reversal operator is used alone. One such problem for time reversal occurs when the propagating medium changes on the time scale of the total time of travel of the return [21]. Another is to use time reversal with side-scan sonar systems. Applications for this capability range from the location of lost shipwrecks such as *Queen Anne's Revenge* off the coast of North Carolina to the location of mines buried in the ocean floor. Since the seafloor itself is dynamic, the sediment that makes up the seabed can scatter the targets from an original central location to anywhere along the beach. This has posed problems for historic sites such as *Queen Anne's Revenge* as a result of massive storms off the coast. Since side-scan sonar systems are far more efficient at covering large areas of seafloor, these targets can be located rapidly. In addition time reversal gives a clearer image of the target, minimizing false identifications. For buried naval mines this is of utmost importance.

1.2 Figures

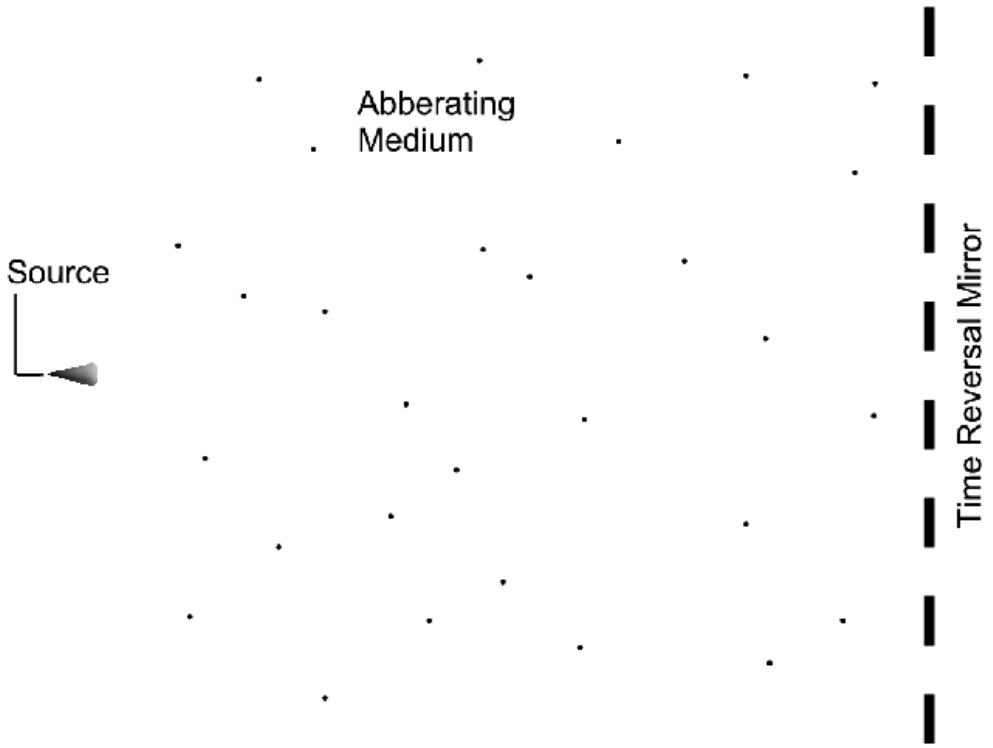

Figure 1.1: Configuration of a forward-scattering time-reversal mirror (TRM). The source is located in a medium with randomly located scatterers a distance away from the fixed TRM. The TRM does not need to be located directly across from the source. Since the above is the forward-scattering geometry, the TRM will here reproduce the original signal at the location of the source.

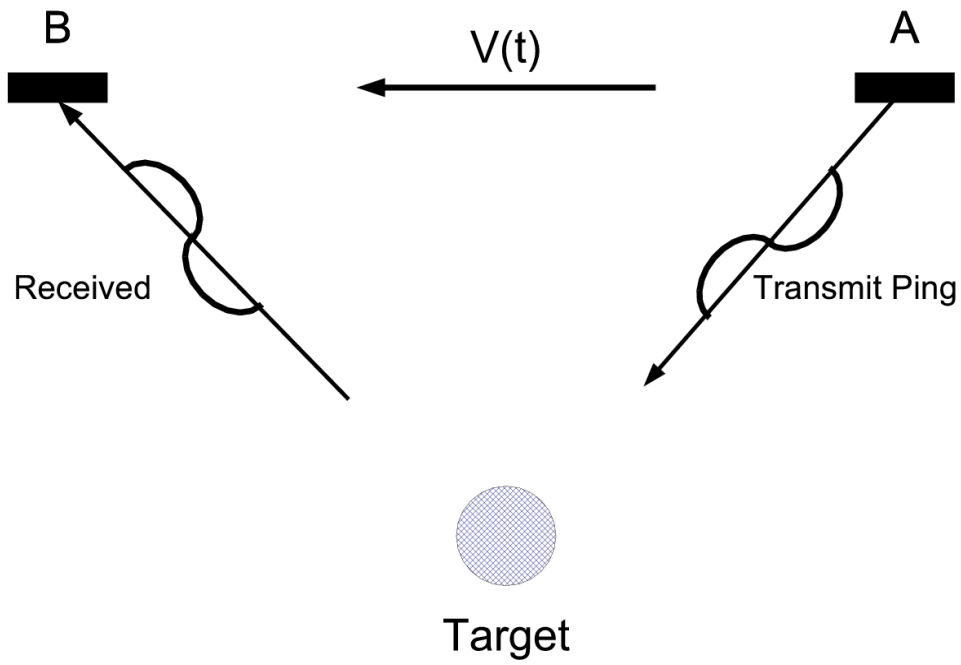

Figure 1.2: Geometry of synthetic-aperture sonar (SAS). The target is pinged by the transducer at A and the field scattered by the target is recorded when the transducer is at B. TRMs would focus the ping back at A from B. However the transducer may not be able to return to location A in the time the time-reversed signal returns to point A.

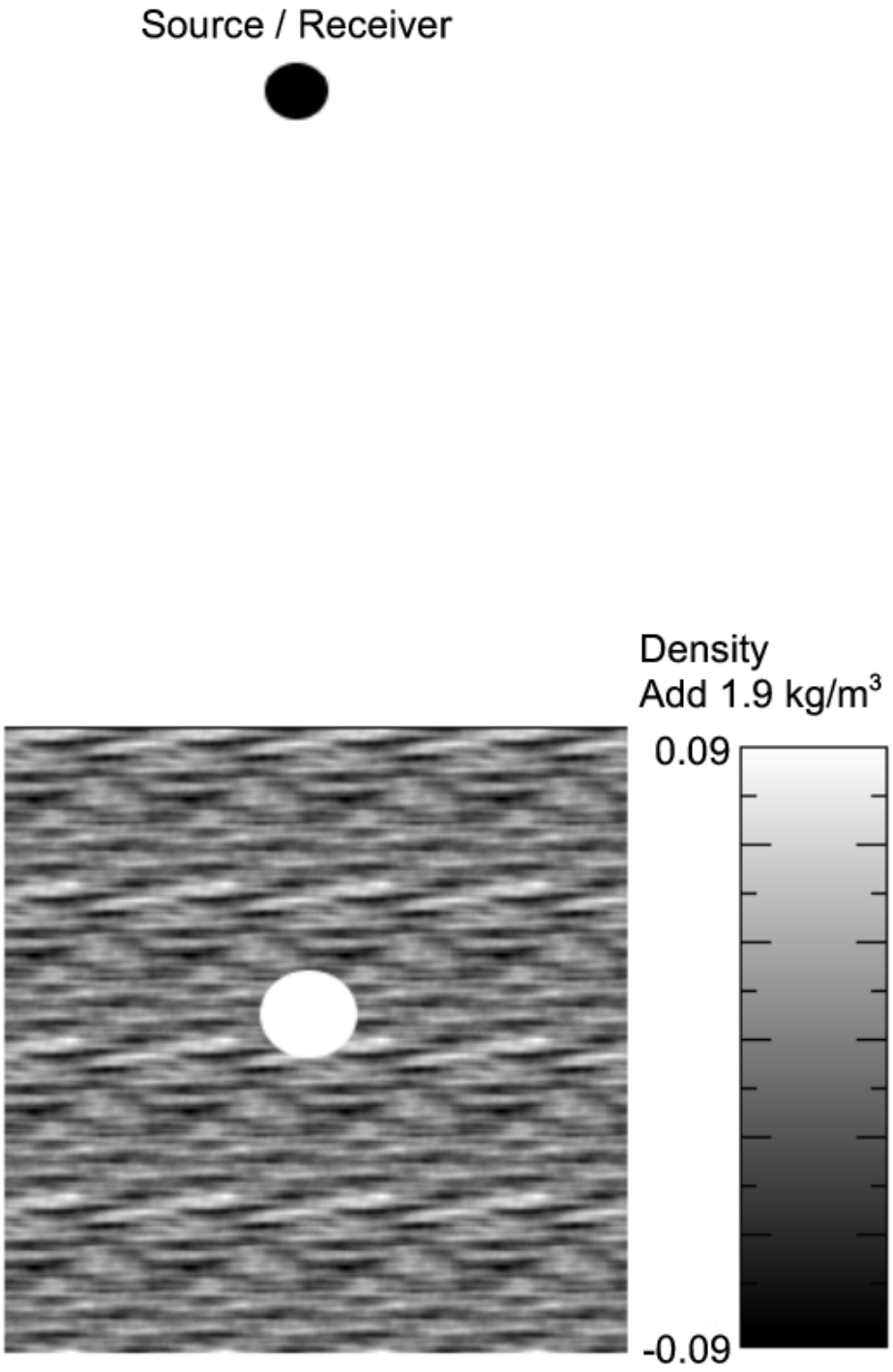

Figure 1.3: The geometry used in the simulations. The transceiver is located in the water column while the target is located at a depth d below the surface of a sediment that has an acoustically inhomogeneous profile.

Chapter 2

Theory: An Acoustics Primer

2.1 Introduction

Acoustics is the study of sound. To be exact, it is the study of how mechanical waves propagate through a material. All materials exhibit longitudinal, also called compressional, waves and transverse, sometimes referred to shear, waves in response to an external force. The two waves are orthogonal and propagate at different speeds. If the medium of study is a fluid or gas, the problem is made tractable by assuming that the fluid is irrotational. In contrast, the fluid dynamicist assumes the fluid is incompressible. The irrotational assumption allows the acoustic equations to be solved using a scalar potential. If the medium is a solid, then the shear forces must be taken into account, which introduces a vector potential.

The problem of time reversal to be addressed here involves a point source receiver in a homogeneous fluid medium insonifying a solid sphere in an inhomogeneous solid-like medium. I focus on applications in the littoral zone, so the second solid-like medium will be treated as a lossy fluid with a density greater than the homogeneous fluid. From physical and geometrical standpoints, the transverse waves generated by the scattering of the sound wave by the seafloor can be ignored.

2.1.1 Linear Wave Equation

The linear wave equation is derived from the fundamental equations of fluid dynamics. The full derivation is presented in Appendix A. The linear wave equation used for all derivations in this document is

$$\nabla^2\psi(\vec{r},t) - \frac{1}{c^2}\frac{\partial^2\psi(\vec{r},t)}{\partial t^2} = -f(\vec{r},t), \tag{2.1}$$

where $-f(\vec{r},t)$ is the forcing term and $\vec{v} = \nabla\psi$ is the velocity potential, since $\vec{v} = -\nabla\psi$. Pressure is related to ψ by

$$p = -\rho_0\frac{\partial\psi(\vec{r},t)}{\partial t}. \tag{2.2}$$

Equation (2.1) is a Sturm-Liouville equation allowing me to use separation of variables to obtain a solution. From Appendix B.1 the solutions will be of the form

$$\psi(\vec{r},t) = \sum_{k=-\infty}^{\infty} A_k R(\vec{r}) e^{(ikct)}. \tag{2.3}$$

with exact solutions to Eq. (2.1) found using a Green's function approach as described in Appendix B.1.1.

To illustrate the general form of the solutions, I will assume a point transceiver located at $\vec{r}_O$ in a fluid-filled half-space. The transceiver emits a delta-function pulse at time t_O. The velocity potential, as derived in Appendix B.1.1 is given by

$$\psi(\vec{r},t) = A\frac{\delta(t - t' - |\vec{r} - \vec{r}_O|/c)}{|\vec{r} - \vec{r}_O|}. \tag{2.4}$$

The second-half space is the ocean floor. Since ocean sediments are not rigid, the transverse sound speed is about one order of magnitude smaller than the longitudinal sound speed (see table B.1). Thus I will treat the ocean floor as a fluid with a higher density and sound speed than the fluid in which the transceiver is located. The next section outlines the general approach leading to a solution for two homogeneous fluid-filled half-spaces. For completeness and to justify why a fluid-fluid model applies to buried-target detection, the fluid-solid case is explained in Appendix B.2.2.

2.2 Half-space Solutions

The number of permutations on a source transmitting in a fluid-filled half-space solutions are infinite. These range from reflecting off an impermeable half-space [34], [35] to interaction with a semi-permeable inhomogeneous half-space with random surface roughness [33]. To illustrate how two seemingly unrelated problems lead to similar solutions, I solve here for the backscattered field from a point impulse source reflecting off a fluid-fluid interface; a fluid-solid interface is discussed in Appendix B.2.2. Both use the geometry shown in Fig. 2.1.

2.2.1 Fluid-Fluid Interface

Consider a point source located at $\vec{r}_O$ in a fluid-filled half-space adjacent to a second fluid-filled half-space, Fig. 2.1. The source fluid has density ρ_1 with constant sound speed c_1 and the adjacent fluid has a higher density ρ_2 and a higher sound speed c_2. The boundary conditions are:

- The normal component of the velocity is continuous across the interface.
- The pressure is continuous across the interface.

There is also a time constraint at the interface that ensures that causality is preserved. Since the geometry exhibits azimuthal symmetry, I can use cylindrical coordinates. The total potential of the source in the source fluid is therefore

$$\psi_1(\vec{r},t) = \frac{A\delta\left(t - t_O - \frac{\sqrt{(r-r_O)^2+(z-z_O)^2}}{c_1}\right)}{\sqrt{(r-r_O)^2+(z-z_O)^2}} + \frac{B\delta\left(t - t_O - \frac{\sqrt{(r-r_O)^2+(z+z_O)^2}}{c_1}\right)}{\sqrt{(r-r_O)^2+(z+z_O)^2}} \tag{2.5}$$

where the first and second terms refer to the potentials associated with the direct and reflected components of the potential. The case $A = B$ is that of an impenetrable

second medium. The velocity potential in the second medium can be written

$$\psi_2(\vec{r},t) = \frac{D\delta\left(t - t_O - \frac{\sqrt{(r-r_T)^2+(z-z_T)^2}}{c_2}\right)}{\sqrt{(r-r_T)^2+(z-z_T)^2}}, \tag{2.6}$$

where the subscript T denotes the location of the virtual transmitting source. The time the source emits the pulse, t_O, will be the same for all potentials. Setting the time the pulses reach the boundary equal I get the condition for the time at which the pulse arrives at the boundary to be

$$t(r_O,z_O)\Big|_{Z=0} = t_O + \frac{\sqrt{(r-r_O)^2+z_O^2}}{c_1} = t_O + \frac{\sqrt{(r-r_T)^2+z_T^2}}{c_2}, \tag{2.7}$$

regardless of the start time t_O. Rearranging terms gives the relationship between the source and image as

$$c_2\sqrt{(r-r_O)^2+z_O^2} = c_1\sqrt{(r-r_T)^2+z_T^2}. \tag{2.8}$$

Pressure conservation at the boundary gives

$$p_1 = p_2 \Rightarrow \rho_1\frac{\partial\psi_1}{\partial t} = \rho_2\frac{\partial\psi_2}{\partial t} \tag{2.9}$$

$$\Rightarrow \rho_1\frac{(A+B)}{\sqrt{(r-r_O)^2+z_O^2}} = \rho_2\frac{D}{\sqrt{(r-r_T)^2+z_T^2}}, \tag{2.10}$$

which after applying Eq. (2.8) gives the relationship between the coefficients

$$D = \frac{\rho_1 c_2}{\rho_2 c_1}(A+B). \tag{2.11}$$

The continuity condition on $\widehat{n}\cdot\vec{v}$ at the interface yields

$$\vec{v}_1\cdot\widehat{z} = \vec{v}_2\cdot\widehat{z} \Rightarrow \frac{\partial\psi_1}{\partial z} = \frac{\partial\psi_2}{\partial z}, \tag{2.12}$$

and after using the definitions for ψ I obtain

$$\begin{aligned}\frac{(A-B)z_O}{((r-r_O)^2+z_O^2)^{3/2}} &= \frac{Dz_T}{((r-r_T)^2+z_T^2)^{3/2}} \\ \Rightarrow (A-B)z_O &= \left(\frac{c_1}{c_2}\right)^3 Dz_T.\end{aligned} \tag{2.13}$$

If I set $B = \mathfrak{R}A$ where $\mathfrak{R}$ is the reflection coefficient and set $D = \mathfrak{T}A$ where $\mathfrak{T}$ is the transmission coefficient I get for Eq. (2.11)

$$\mathfrak{T} = \frac{\rho_1 c_2}{\rho_2 c_1}(1 + \mathfrak{R}) \tag{2.14}$$

and Eq. (2.13) becomes

$$z_T = \frac{(1 - \mathfrak{R})}{\mathfrak{T}} \left(\frac{c_2}{c_1}\right)^3 z_O \tag{2.15}$$

It is interesting to note that the observer in the second medium sees the source at a location behind the physical location of the source. Also the transmission coefficient has a weighting factor that depends on the sound speeds and densities of the two fluids.

Setting the tangential components of the velocity equal across the boundary gives

$$\vec{v}_1 \cdot \hat{r} = \vec{v}_2 \cdot \hat{r} \Rightarrow \frac{\partial \psi_1}{\partial r} = \frac{\partial \psi_2}{\partial r}. \tag{2.16}$$

Using the definition of ψ with the constants B and D replaced with $\mathfrak{R}A$ and $\mathfrak{T}A$ gives

$$\frac{(1 + \mathfrak{R})(r - r_O)}{((r - r_O)^2 + z_O^2)^{3/2}} = \frac{\mathfrak{T}(r - r_T)}{((r - r_T)^2 + z_T^2)^{3/2}}. \tag{2.17}$$

I now define the angle γ_i as the angle between the observation point on the surface and the normal going through the source point:

$$\sin \gamma_i = \frac{r - r_i}{\sqrt{(r - r_i)^2 + z_i^2}}, \tag{2.18}$$

where i is either O or T. Using this relation and Eqs. (2.8), (2.14), and (2.17), the above equation becomes

$$\begin{aligned} (1 + \mathfrak{R}) \sin \gamma_O &= \mathfrak{T} \left(\frac{c_1}{c_2}\right)^2 \sin \gamma_T \\ \Rightarrow \frac{\sin \gamma_O}{\rho_1 c_1} &= \frac{\sin \gamma_T}{\rho_2 c_2}, \end{aligned} \tag{2.19}$$

which is Snell's law. Using Eq. (2.14) and

$$\cos \gamma_i = \frac{z_i}{\sqrt{(r - r_i)^2 + z_i^2}} \tag{2.20}$$

for i equal to either O or T, I get for Eq. (2.15)

$$\frac{\cos\gamma_O}{\rho_1 c_1} = \left(\frac{1+\mathfrak{R}}{1-\mathfrak{R}}\right)\frac{\cos\gamma_T}{\rho_2 c_2}. \tag{2.21}$$

This is "Snell's law", but for cosines.

Combining Eqs. (2.8) and (2.14) with the transmitted velocity potential (2.6) gives

$$\psi_2(\vec{r},t) = (1+\mathfrak{R})\frac{\rho_1}{\rho_2}\frac{A\delta\left(t - t_O - \frac{\sqrt{(r-r_O)^2+(z-z_O)^2}}{c_1}\right)}{\sqrt{(r-r_O)^2+(z-z_O)^2}}, \tag{2.22}$$

which expresses $\psi_2(\vec{r},t)$ in terms of the source location $\vec{r}_O$ and the surface reflection coefficient $\mathfrak{R}$.

2.2.2 Scattering From a Sphere

To derive the scattered field from a solid sphere located in a solid medium, I will ignore the transverse waves since c_T/c_L is much less than 1. An observer located at the source position $\vec{r}_O$ would see the sphere centered at $\vec{r}_c$ lying on the axis connecting the two. As a result I only need to concern myself with the longitudinal wave in the solid [36], [37] and the monopole response off the sphere.

Impulse Response

Using the impulse function described by Eq. (2.6) and assuming a homogeneous environment, I have

$$\psi_{inc}(\vec{r},t) = D\frac{\delta\left(t - t_O - \frac{|\vec{r}-\vec{r}_O|}{c}\right)}{|\vec{r}-\vec{r}_O|} \tag{2.23}$$

where

$$D = A(1+\mathfrak{R})\frac{\rho_1}{\rho_2}, \tag{2.24}$$

c_1 is the sound speed in the medium surrounding the source, and ρ_1 and ρ_2 are the densities of the source and target fluids respectively. From now on I will drop the subscript 1 on the speed of sound in the source medium. Setting $\vec{r}-\vec{r}_O$ equal to

$\vec{r} - \vec{r}_c + \vec{r}_c - \vec{r}_O$ allows me to expand the field about the point $\vec{r}_c$. Using the triangle inequality yields

$$|\vec{r} - \vec{r}_c + \vec{r}_c - \vec{r}_O| \leq |\vec{r}_c| + d, \tag{2.25}$$

where $\vec{r}_c$ and d are shown in Fig. 2.2. This allows me to write the incident potential as

$$\psi_{inc}(\vec{r}, t) = D \frac{\delta\left(t - t_O - \frac{|\vec{r}_c|+d}{c}\right)}{|\vec{r}_c| + d} \tag{2.26}$$

Using the geometry shown in Fig. 2.2, the total potential in the second medium will be of the form

$$\psi(\vec{r}, t) = \psi_{inc}(\vec{r}, t) + \psi_{sc}(\vec{r}, t) \tag{2.27}$$

where ψ_{inc} is the potential of the incident field given by Eq. (2.26) and ψ_{sc} is the potential scattered by the sphere. It is standard to expand the scattered potential as

$$\psi_{sc}(\vec{r}, t) = \sum_{k=-\infty}^{\infty} \sum_{n=0}^{\infty} \sum_{m=-n}^{n} A_{k,n}^{(c),m} h_n(kr_c) Y_n^m(\theta_c, \phi_c) e^{ikct} \tag{2.28}$$

where the subscript c denotes the expansion about the center of the sphere as shown in Fig. 2.2. The next step is to write the expansion of the incident field about the center of the sphere. Assuming $d \geq r_c$ gives

$$\psi_{inc}(\vec{r}, t) = \frac{D}{\sqrt{4\pi}} \sum_{k=-\infty}^{\infty} \sum_{l=0}^{\infty} \sum_{s=-l}^{l} \frac{1}{2l+1} \frac{r_c^l}{d^{l+1}} Y_l^s(\theta_c, \phi_c) e^{ikc\left[t - \left(t_O + \frac{|\vec{r}_c|+d}{c}\right)\right]} \tag{2.29}$$

where the subscript c denotes the location of the center of the sphere while c_L is the longitudinal sound speed in the medium. The boundary condition on the sphere is given by

$$\left(\frac{\partial \psi}{\partial n} + i\sigma\psi\right)\Bigg|_S = 0 \tag{2.30}$$

where σ is the acoustical admittance of the sphere. This can be set equal to 0 for any reasonably acoustically hard medium relative to the surrounding sediment, for example an iron sphere, and to ∞ for any infinitely acoustically soft medium.

Applying the boundary conditions at the surface of the sphere $r_c = a$, I obtain for the potential

$$\psi\Big|_S = \sum_{k=-\infty}^{\infty}\sum_{l=0}^{\infty}\left(\frac{D}{\sqrt{4\pi}}\frac{1}{2l+1}\frac{a^l}{d^{l+1}}e^{ikc\left[t-\left(t_O+\frac{d+a}{c}\right)\right]} + A_{k,l}h_l(ka)e^{ikct}\right). \tag{2.31}$$

The normal derivative is

$$\frac{\partial\psi}{\partial r_c}\Big|_S = \sum_{k=-\infty}^{\infty}\sum_{l=0}^{\infty}\left(\frac{D}{\sqrt{4\pi}}\frac{1}{2l+1}\frac{a^l}{d^{l+1}}\left[\frac{l}{a}+ik\right]e^{ikc\left[t-\left(t_O+\frac{d+a}{c}\right)\right]} + A_{k,l}kh_l\,'(ka)e^{ikct}\right) \tag{2.32}$$

where the term ik comes from the derivative of the exponential in the incident field. Substituting the above two equations into the boundary condition gives

$$A_{k,l}e^{ikct}[kh_l\,'(ka) + i\sigma h_l(ka)] = -\frac{D}{\sqrt{4\pi}}\frac{1}{2l+1}\frac{a^l}{d^{l+1}}\left[\frac{l}{a}+i(k+\sigma)\right]e^{ikc\left[t-\left(t_O+\frac{d+a}{c}\right)\right]} \tag{2.33}$$

for each l in the expansion. Solving Eq. (2.33) for the coefficient $A_{k,l}$ gives

$$A_{k,l} = -\frac{D}{\sqrt{4\pi}}\frac{1}{2l+1}\frac{a^l}{d^{l+1}}\frac{[(l/a)+i(k+\sigma)]}{[kh_l\,'(ka)+i\sigma h_l(ka)]}e^{-ikc\left(t_O+\frac{d+a}{c}\right)}. \tag{2.34}$$

Using Eq. (2.34) in Eq. (2.28) and substituting the result in Eq. (2.26) gives

$$\begin{aligned}\psi(\vec{r},t) = \sum_{k=-\infty}^{\infty}\sum_{l=0}^{\infty}\sum_{s=-l}^{l}\frac{D}{\sqrt{4\pi}}\frac{1}{2l+1}\frac{Y_l^s(\theta_c,\phi_c)}{d^{l+1}}e^{ikc\left(t-\left(t_O+\frac{d}{c}\right)\right)} \\ \times\left[r_c^l e^{ik|\vec{r}_c|} - \frac{a^l[(l/a)+i(k+\sigma)]}{[kh_l\,'(ka)+i\sigma h_l(ka)]}h_l(kr_c)e^{ika}\right].\end{aligned} \tag{2.35}$$

As expected the total scattered potential contains geometrical information about the sphere in the spherical Hankel functions. The impulse response from a sphere is the multipole expansion of the potential. This result also depends on the term ka in the expansion, providing in principle information about the target. At the source location, $\vec{r_O}$, the target will appear as a monopole. Assuming the sphere is acoustically infinitely hard, $\sigma = 0$, and setting $t_0 = 0$, the return signal at the source is

$$\psi(\vec{r}_O,t) = \sum_{k=-\infty}^{\infty}\frac{D}{d}e^{ikct}\left[1 - i\frac{h_0(kd)}{h_0\,'(ka)}e^{ik(d-a)}\right] \tag{2.36}$$

with D given by Eq. (2.24). Setting the time equal to the total time of travel for the pulse, $ct = 2(d-a)$, sets Eq. (2.36) to

$$\psi\left(\vec{r}_O, \frac{2(d-a)}{c}\right) = \sum_{k=-\infty}^{\infty} \frac{D}{d} e^{ik(d-a)} \left[e^{ik(d-a)} + i\frac{h_0(kd)}{h_1(ka)}\right] \tag{2.37}$$

where I have used the relation that $h_0\,'(x) = -h_1(x)$. This expression shows that the impulse response will give the location of the surface of the sphere as in Fig. 2.3. Here, I keep the separation between the surface of the sphere and the detector fixed at 10 m while varying the sphere radius from 0.05 m to 0.5 m. The fluctuations in the amplitudes are from the mixing of the exponential functions with the spherical Hankel functions in Eq.(2.37). When the radius of the sphere is fixed and the sphere is moved away from the source the quasi-periodic behavior of the amplitude of the impulse is apparent, as in Fig. 2.4, which is the result of the mixing of the two exponentials an the Hankel functions in Eq. (2.37).

One-Cycle Cosine Pulse

A more practical signal is the one-cycle cosine pulse from a source located at $\vec{(}r)_c$. The pulse is defined as

$$\psi(\vec{r}_c, t) = \begin{cases} 0 & t < 0 \\ \cos(\omega_0 t - k_0(d - r_c)) & 0 \le t \le \frac{2\pi}{\omega_0} \\ 0 & t > \frac{2\pi}{\omega_0} \end{cases} \tag{2.38}$$

where d is the location of the scattering target and ω_0 is the frequency defined as $\omega_0 = 2\pi/T$. The above function can be rewritten in terms of a convolution with a rectangular pulse as

$$\psi(\vec{r}_c, t) = \cos(\omega_0 t - k_0(d - r_c)) \circledast rect\left[\frac{t - T/2}{T}\right]. \tag{2.39}$$

In the above equation $\circledast$ represents convolution with respect to time, *rect* is the rectangle function defined by

$$rect\left[\frac{t-T/2}{T}\right] = \begin{cases} 0 & t<0 \\ 1 & 0 \le t \le T \\ 0 & t>T \end{cases} \tag{2.40}$$

This function sets the cosine to one cycle, and T is the period of the signal. Using the above potential for the incident potential the total monopole potential with the scattered potential will be of the form

$$\begin{aligned} \psi_{monopole}(r_c,t) = \sum_{k=-\infty}^{\infty} & \cos(\omega_0 t - k_0(d-r_c)) \circledast rect\left[\frac{t-T/2}{T}\right] \\ & + \sin(\omega_0 t - k_0(d-r_c)) \circledast rect\left[\frac{t-T/2}{T}\right] \frac{k_0}{k}\frac{h_0(kr_c)}{h_1(ka)} \end{aligned} \tag{2.41}$$

where I have already set the derivative of the zeroth order spherical Hankel function equal to the negative of the first order spherical Hankel function. At the source location, $r_c = d$, the above return simplifies to

$$\begin{aligned} \psi_{monopole}(r_c=d,t) = \sum_{k=-\infty}^{\infty} & \cos(\omega_0 t) \circledast rect\left[\frac{t-T/2}{T}\right] \\ & + \sin(\omega_0 t) \circledast rect\left[\frac{t-T/2}{T}\right] \frac{k_0}{k}\frac{h_0(kd)}{h_1(ka)}. \end{aligned} \tag{2.42}$$

The convolution operation with the rectangle function above sets the limits of integration on the Fourier transform of the above with gives

$$\psi_{monopole}(r_c=d,t) = \sum_{\omega=-\infty}^{\infty}\sum_{k=-\infty}^{\infty} \frac{2e^{i\pi\omega/\omega_0}\sin(\pi\omega/\omega_0)}{\sqrt{2\pi}(\omega^2-\omega_0^2)}\left[\omega + i\omega_0\frac{k_0}{k}\frac{h_0(kd)}{h_1(ka)}\right]. \tag{2.43}$$

By setting $\omega = kc$, I finally get the total monopole potential scattered by a sphere as

$$\psi_{monopole}(r_c=d,t) = \sum_{k=-\infty}^{\infty} \frac{2e^{i\pi k/k_0}\sin(\pi k/k_0)k}{\sqrt{2\pi}c(k^2-k_0^2)}\left[1 + i\frac{h_0(kd)}{h_1(ka)}\right]. \tag{2.44}$$

The above equation is the spatial Fourier expansion of the response of the sphere to the incident potential given by Eq. (2.39). What should be apparent from Eq. (2.44)

is that the scattered potential pulse retains some of the incident pulse shape. Figure 2.5 shows the response from spheres of radii ranging from 5 cm to 50 cm centered 10 m away from the source from an incident potential pulse with a duration of 100 μs. The original pulse shape remains between the two horns on the top of each pulse. The horns themselves are due to the rectangular window used to limit the duration of the pulse. The location of the surface of the sphere is determined by the left side of the pulse, which is to be expected from the ratios of the spherical Hankel functions in Eq. (2.44). Changing the duration of the incident pulse does not change the ability to locate the surface of the sphere, as shown in Fig. 2.6, where I have plotted the response from the same geometry of that of Fig. 2.5, but changed the duration of the pulse from 100 μs to 10 μs. The incident potential pulse shape is not present because the time step used for these figures was 1 μs. There is a complex behavior between the location of the center of the sphere and its radius, although the main dependence on the amplitude of the return is on the radius of the sphere as shown by comparing Figs. 2.5 and 2.7. Figure 2.5 shows a clear dependence of the amplitude of the return on the radius of the spheres; the larger the sphere the greater the return, which is consistent with scattering theory. In contrast, Fig. 2.7 shows that moving the sphere results in little change in the amplitude of the returns. The difference between the two results can be explained by the ratio of the spherical Hankel functions in Eq. (2.44). Since the radius of the sphere is at least one order of magnitude smaller than the separation between the source and the sphere, or as in the case of Fig. 2.7, the radius of the sphere is about twenty times smaller than the distance between the source and the sphere, the spherical Hankel function of the radius will vary more than that which depends on the distance.

2.3 Time Reversal

2.3.1 General Time Reversal of Signals

Closer examination of the linear acoustic equation (2.1) shows that it is reciprocal in both space and time. Replacing r with $-r$ or t with $-t$ will give the same equation. The same conclusion can be made by using the complex conjugate of the solution to solve for Eq. (2.1). Performing the same replacement of variables with Eq. (B.8) will leave the left hand side intact with the only concern being the properties of the forcing term. Since the free-space acoustic equation has this spatio-temporal reciprocity, it is possible to create an acoustical time-reversal mirror to negate the effects of the propagating medium [24], [12]. Time reversal in acoustics is the performed by placing an array of transceivers away from an acoustical source. These transceivers record the signal from the source that is obscured by the propagating medium. The signal is then transmitted in reverse temporal order. Assuming that the medium has not changed during the recording and time reversal period, the field will focus at the location of the source. Consider the following example similar to Fink, *et. al.* [12] where a source located at $\vec{r}_O$ emits a forcing term at time t_O given by $f(\vec{r}-\vec{r}_O, t-t_O)$. The potential field generated is defined by

$$\psi(\vec{r},t) = \iiint d^3r' \int dt' G(\vec{r},t;\vec{r}\,',t') f(\vec{r}\,' - \vec{r}_O, t' - t_O) \tag{2.45}$$

where $G(\vec{r},t;\vec{r}\,',t')$ is the Green's function that includes all the properties of the propagating medium. At the location of the time reversal mirror (TRM), the field is recorded over the time interval T and transmitted in reverse temporal order. This gives

$$\psi_2(\vec{r},t) = \psi(\vec{r},T-t) = \iiint d^3r' \int dt' G(\vec{r},T-t;\vec{r}\,',t') f(\vec{r}\,' - \vec{r}_O, t' - t_O) \tag{2.46}$$

$$\square\psi_2(\vec{r},t)\cdot\hat{n} = \square\psi(\vec{r},T-t)\cdot\hat{n} \tag{2.47}$$

where I have used

$$\square = \nabla + \frac{i}{c}\frac{\partial}{\partial t} \tag{2.48}$$

to simplify the notation in the equations. Transmission of $\psi_2(\vec{r},t)$ is written as

$$\psi_{tr}(\vec{r}_1,t_1) = \iint d^2r \int dt[G(\vec{r}_1,t_1;\vec{r},t)\Box\psi_2(\vec{r},t) - \psi_2(\vec{r},t)\Box G(\vec{r}_1,t_1;\vec{r},t)] \cdot \hat{n} \quad (2.49)$$

which becomes

$$\psi_{tr}(\vec{r}_1,t_1) = \iiint d^3r \int dt[G(\vec{r}_1,t_1;\vec{r},t)\Box^2\psi(\vec{r},T-t) - \psi(\vec{r},T-t)\Box^2 G(\vec{r}_1,t_1;\vec{r},t)] \quad (2.50)$$

after substitution of $\psi(\vec{r},T-t)$ and the use of a time-dependent Green's second identity given by

$$\iiint d^3r \int dt[\phi\Box^2\psi - \psi\Box^2\phi] = \iint d^2r \int dt[\phi\Box\psi - \psi\Box\phi] \cdot \hat{n}. \quad (2.51)$$

Recall that the definition of a Green's function is

$$\Box^2 G(\vec{r},t;\vec{r}\,',t') = -4\pi\delta(\vec{r}-\vec{r}\,')\delta(t-t'). \quad (2.52)$$

Using the above in the second term of Eq. (2.50) yields

$$\iiint d^3r \int dt\psi(\vec{r},T-t)\Box^2 G(\vec{r}_1,t_1;\vec{r},t) = \psi(\vec{r}_1,T-t_1). \quad (2.53)$$

Using the definition of $\psi(\vec{r},t)$ from Eq. (2.45) in Eq. (2.50) yields

$$\begin{aligned}
&\iiint d^3r \int dt G(\vec{r}_1,t_1;\vec{r},t)\Box^2\psi(\vec{r},T-t) \\
&= \iiint d^3r \int dt G(\vec{r}_1,t_1;\vec{r},t)\Box^2 \iiint d^3r' \int dt' G(\vec{r},t;\vec{r}\,',t')f(\vec{r}\,'-\vec{r}_O,t'-t_O) \\
&= -4\pi \iiint d^3r \int dt G(\vec{r}_1,t_1;\vec{r},t) \iiint d^3r' \int dt'\delta(\vec{r}-\vec{r}\,')\delta(t-t')f(\vec{r}\,'-\vec{r}_O,t'-t_O) \\
&= -4\pi \iiint d^3r \int dt G(\vec{r}_1,t_1;\vec{r},t)f(\vec{r}\,'-\vec{r}_O,T-t-t_O)
\end{aligned} \quad (2.54)$$

Combining Eqs. (2.53) and (2.54) in Eq. (2.50) yields

$$\psi_{tr}(\vec{r}_1,t_1) = 4\pi[\psi(\vec{r}_1,T-t_1) - \iiint d^3r \int dt G(\vec{r}_1,t_1;\vec{r},t)f(\vec{r}'-\vec{r}_O,T-t-t_O)] \quad (2.55)$$

for the time reversed field. This can be thought of as the superposition of incoming and outgoing waves with respect to the source location.

Another approach to time reversal of acoustical signals is to use the temporal Fourier transform of the signals. In this case the time reversed wave is calculated by calculating the complex conjugate of the incident wave in temporal Fourier space

$$f(x,t) = \sum_{\omega=-\infty}^{\infty} F(x,\omega)e^{-i\omega t} \underset{\text{TR}}{\Rightarrow} \sum_{\omega=-\infty}^{\infty} F^*(x,\omega)e^{i\omega t} \tag{2.56}$$

where $F(x,\omega)$ is assumed real. Figure 2.8 is a simple illustration of this phenomena. Consider a simple example of a temporal signal being time reversed by the use of a time-reversal mirror as in Fig. 1.1. The mirror records

$$f_1(t) = \int g(t')G(t-t')dt' \tag{2.57}$$

where $g(t')$ is the original pulse shape and $G(t-t')$ is the propagation Green's function. After the time-reversal operation and transmission the signal at the source point is given by

$$f_2(t) = \int G(\omega)g(\omega)G(-\omega)(e)^{-i\omega t}d\omega \tag{2.58}$$

in the frequency domain. After N iterations of this process, two results are measured depending whether N is odd or even. For an odd number of iterations, the resulting function is

$$f_{Nodd}(t) = \int G^{(N-1)/2}(\omega)g(\omega)G^{(N+1)/2}(-\omega)e^{-i\omega t} \tag{2.59}$$

while for an even number of iterations the signal is

$$f_{Neven}(t) = \int G^{N/2}(\omega)g(\omega)G^{N/2}(-\omega)e^{-i\omega t}. \tag{2.60}$$

From the above results, which are consistent with the current theories such as Prada [30] and Chambers [28].

The problems that are inherent in time reversal in acoustics are:

- Waveforms that are recorded for a finite amount of time lead to aliasing of the time-reversed wave.

- The success of time reversal in a dynamical medium is limited. It is usually assumed that the medium is not a function of time, so the spatial reciprocity of the medium is not violated.
- Time-reversal mirrors (TRMs) oriented to receive the forward-scattered signal lose the backscattered signal.

2.3.2 Time reversal for backscattered signals

Now I consider a single transceiver located at $\vec{r}_O$ and a target of arbitrary shape centered at $\vec{r}_C$. I define the distance from transceiver to target as $d = |\vec{r}_C - \vec{r}_O|$, and set this distance to be much larger than the dimension of both the transceiver and the target. Furthermore, I set the transceiver dimension to be much smaller than the median dimension of the target so I can treat the source-receiver as a point. I set the sound speed of the medium enclosing both to c. The basic geometry is shown in Fig. 2.2 for a spherical target and a point transceiver, both located away from the origin point "O". The velocity potential from the transceiver can be written as

$$\psi(\vec{r}, t) = G_f(\vec{r}, t; \vec{r}_O, t_O) \circledast f(\vec{r}_O, t_O) \tag{2.61}$$

where $G_f(\vec{r}, t; \vec{r}_O, t_O)$ is the forward-propagating Green's function, $f(\vec{r}_O, t_O)$ is the forcing function from the source, and $\circledast$ represents the integration, which is a convolution over time and space. From this point on all propagating Green's functions will use the notation that the time on the left hand side of the semicolon is the time on the right hand side with the added term. I define a scattering operator $S(\vec{r}_C, t)$ that does not affect time, i.e., the scattering is instantaneous. Using this notation, I can write the backscattered signal measured by the transceiver as

$$\psi(\vec{r}_O, t) = G_b\left(\vec{r}_O, t + \frac{d}{c}; \vec{r}_O, t\right) \circledast S(\vec{r}_C, t) \circledast G_f\left(\vec{r}_C, t + \frac{d}{c}; \vec{r}_O, t_O\right) \circledast f(\vec{r}_O, t_O) \tag{2.62}$$

where G_b is the back-propagating Green's function which I assume not to be equal to G_f. I define the time-reversal operator (TRO) $R(T - t; t)$ with the following properties:

- Addition of a time delay, T, which manifests itself as a window for the signal, forcing the signal to be finite in time after this operation.
- The signal is transmitted in reverse temporal order from the order of reception forcing the wave to propagate backward through space.
- The above two conditions have the effect of creating a finite time space where the signal exists only in the range $T + t_O + \frac{d}{c}$ and $T + t_O + \frac{2d}{c}$. Figure 2.8 gives a simple illustration of this effect.
- Any additional gain to the signal is done with this operator by a multiplicative factor.

Using the TRO on Eq. (2.62) the target scatters the potential

$$\begin{aligned} \psi(\vec{r}_C, t) = G_f\left(\vec{r}_C, t - \frac{d}{c}; \vec{r}_O, t\right) \circledcirc R(T-t, t) \circledcirc \\ G_b\left(\vec{r}_O, t + \frac{d}{c}; \vec{r}_O, t\right) \circledast S(\vec{r}_C, t) \circledast G_f\left(\vec{r}_C, t + \frac{d}{c}; \vec{r}_O, t_O\right) \circledast f(\vec{r}_O, t_O) \end{aligned} \tag{2.63}$$

where I define $\circledcirc$ as convolution with respect to time only. After scattering by the target, the transceiver records potential given by

$$\begin{aligned} \psi(\vec{r}_O, t) = G_b\left(\vec{r}_O, t + \frac{d}{c}; \vec{r}_O, t\right) \circledast S(\vec{r}_C, t) \circledast G_f\left(\vec{r}_C, t - \frac{d}{c}; \vec{r}_O, t\right) \circledcirc R(T-t, t) \circledcirc \\ G_b\left(\vec{r}_O, t + \frac{d}{c}; \vec{r}_O, t\right) \circledast S(\vec{r}_C, t) \circledast G_f\left(\vec{r}_C, t + \frac{d}{c}; \vec{r}_O, t_O\right) \circledast f(\vec{r}_O, t_O). \end{aligned} \tag{2.64}$$

Performing another TRO iteration gives the signal recorded at the transceiver as

$$\begin{aligned} \psi(\vec{r}_O, t) = G_b\left(\vec{r}_O, t + \frac{d}{c}; \vec{r}_O, t\right) \circledast S(\vec{r}_C, t) \circledast G_f\left(\vec{r}_C, t - \frac{d}{c}; \vec{r}_O, t\right) \circledcirc R(T-t, t) \circledcirc \\ G_b\left(\vec{r}_O, t + \frac{d}{c}; \vec{r}_O, t\right) \circledast S(\vec{r}_C, t) \circledast G_f\left(\vec{r}_C, t - \frac{d}{c}; \vec{r}_O, t\right) \circledcirc R(T-t, t) \circledcirc \\ G_b\left(\vec{r}_O, t + \frac{d}{c}; \vec{r}_O, t\right) \circledast S(\vec{r}_C, t) \circledast G_f\left(\vec{r}_C, t + \frac{d}{c}; \vec{r}_O, t_O\right) \circledast f(\vec{r}_O, t_O). \end{aligned} \tag{2.65}$$

The pattern that is developing in the TRO allows me to define a new backscattered time-reversal operator (B_{TRO}) as

$$B_{TRO} = G_b\left(\vec{r}_O, t + \frac{d}{c}; \vec{r}_O, t\right) \circledast S(\vec{r}_C, t) \circledast G_f\left(\vec{r}_C, t - \frac{d}{c}; \vec{r}_O, t\right) \circledcirc R(T-t, t), \quad (2.66)$$

and after setting the first backscattered waveform to

$$\psi_{bs}(\vec{r}, t) = G_b\left(\vec{r}_O, t + \frac{d}{c}; \vec{r}_O, t\right) \circledast S(\vec{r}_C, t) \circledast G_f\left(\vec{r}_C, t + \frac{d}{c}; \vec{r}_O, t_O\right) \circledast f(\vec{r}_O, t_O) \quad (2.67)$$

I can write the general iterative time-reversal operation as

$$\psi_i(\vec{r}, t) = \prod_{i=0}^{N} \left(B_{TRO}\right)^i \circledcirc \psi_{bs}(\vec{r}, t) \quad (2.68)$$

where $\prod_{i=0}^{N}$ denotes that the convolution is to be performed for each iteration i. Note that unlike other time reversal experiments [11], [20], [30], and [17], this derivation uses the backscattered response only and is developed in the time domain, not in the frequency domain, as others [19].

It should be apparent that the initial backscattered response given by Eq. (2.67) is what is being time reversed, and not the original waveform. If time reversal can enhance a signal by recreating the original signal, it fails in the backscattered direction. To recreate the original pulse using the backscattered signal requires inverting the backscattered response using the relevant properties of the propagating medium and the scattering object. However, iterative time reversal can be used to clean up or improve the quality of the backscattered signal from the target, which can be used to classify the target.

As in the case of time-reversal mirrors in the previous section, it is instructive to perform the same analysis of the time-reversal procedure for backscattered signals in the frequency domain. I will consider a simple time-dependent pulse $g(t)$ originating from a point transducer which is normally incident on an arbitrary scatterer. The pulse propagates to the target according to

$$f(t) = \int_{\infty}^{\infty} dt' g(t') G(t - t') \quad (2.69)$$

where $G(t-t')$ is the propagation Green's function. The above signal is scattered by the target and the transducer records the backscattered response

$$f_1(t) = \int dt'' G(t-t') \int dt' g(t') G_S(t''-t') \tag{2.70}$$

where I have set the scattering operation to changing the propagation Green's function such that $G_S(t-t') \neq G(t-t')$. Equation (2.70) has an inverse Fourier transform of

$$F_1(\omega) = G(\omega) g(-\omega) G_S(\omega). \tag{2.71}$$

Time reversing Eq. (2.70) results in a second backscattered signal of the form

$$f_2(t) = \int dt'' G(t-t') \int dt' G_S(t''-t') f_1^+(t') \tag{2.72}$$

where the + denotes the time-reversal operation. In the frequency domain, $f_2(t)$ is

$$F_2(\omega) = G(-\omega) G(\omega) g(-\omega) G_S^2(\omega). \tag{2.73}$$

Performing the same procedure on $f_2(t)$ yields for the next recorded signal

$$f_3(t) = \int dt'' G(t-t') \int dt' G_S(t''-t') f_2^+(t') \tag{2.74}$$

with an inverse Fourier transform of

$$F_2(\omega) = G^3(\omega) g(\omega) G_S^3(-\omega). \tag{2.75}$$

This is a surprising result since I now have $g(\omega)$ instead of $g(-\omega)$ and the Green's functions are exhibiting a symmetry with respect to scattering. Performing another iteration of the time-reversal procedure on Eq. (2.74) yields

$$f_4(t) = \int dt'' G(t-t') \int dt' G_S(t''-t') f_3^+(t') \tag{2.76}$$

with the corresponding inverse transform of

$$F_4(\omega) = G(-\omega) G^3(\omega) g(\omega) G_S^3(-\omega) G_S(\omega), \tag{2.77}$$

which I can rewrite as

$$F_4(\omega) = G(-\omega)F_3(\omega)G_S(\omega). \tag{2.78}$$

Equation (2.77) shows that $F_3(\omega)$ is the waveform that the time-reversal operator converges to using backscattered signals. One more iteration yields

$$f_5(t) = \int dt'' G(t-t') \int dt' G_S(t''-t') f_4^+(t') \tag{2.79}$$

with the corresponding inverse transform of

$$F_5(\omega) = G^2(-\omega)G^3(\omega)g(\omega)G_S^3(-\omega)G_S^2(\omega), \tag{2.80}$$

which I can rewrite as

$$F_5(\omega) = G^2(-\omega)F_3(\omega)G_S^2(\omega). \tag{2.81}$$

After N iterations, the transceiver will record, in inverse Fourier space

$$F_N(\omega) = G^{N-3}(-\omega)F_3(\omega)G_S^{N-3}(\omega). \tag{2.82}$$

This is a remarkable result for two reasons. First, convergence to a single waveform occurs after two iterations of the time-reversal operator, which means that once the third return is recorded we have detected the target if there is one present. Secondly, this shows that the time-reversal operator acts as a nonlinear filter to the signal by multiplying each iteration after the third by $G(\omega)G_S(-\omega)$. Therefore, each iteration of the time-reversal operator after the second will enhance the return from the target. This analysis is the same as that that yields Eq. (2.68), but the behavior of the time-reversal operator is more transparent.

A simple example of the behavior of the iterative time-reversal operator on backscattered signals is demonstrated by considering the impulse response of a scatterer located in a lossless medium. I define the initial impulse signal as $g(t) = g_0\delta(t)$ and the scattering Green's function as

$$G(t,t') = u\left(t - \frac{d}{c} - t'\right) e^{(t-d/c-t')/\tau} \tag{2.83}$$

where u is the unit step function required for causality, d is the distance from the source to the scatterer, and c is the speed of sound in the medium. Using a lossless medium, an observer will measure

$$f_1(t) = \int_{\infty}^{\infty} dt' g(t') G(t,t') = g_0 e^{-(t-2d/c)/\tau} u\left(t - \frac{2d}{c}\right). \tag{2.84}$$

The time-reversal operator will set a window in the time-domain that I define starting at t_1 and ending at t_2. With this condition in mind, the time-reversal operator acting on Eq. (2.84) yields for the signal incident on the scatterer

$$g_1(t') = g_0 u\left(t' - \left(t_1 + \frac{d}{c}\right)\right) e^{-(t'-(t_1+d/c))/\tau} u\left(t_2 + \frac{d}{c} - t'\right) \tag{2.85}$$

where the unit step functions are used to turn on the signal at t_1 and turn off the signal at t_2, $t_1 < t_2$. Performing the convolution with the scattering Green's function of Eq. (2.83) on Eq. (2.85) yields

$$\begin{aligned} f_2(t) = \int_{\infty}^{\infty} dt' g_0 u\left(t' - \left(t_1 + \frac{d}{c}\right)\right) e^{-(t'-(t_1+d/c))/\tau} u\left(t_2 + \frac{2d}{c} - t'\right) \\ u\left(t - \frac{d}{c} - t'\right) e^{(t-(t'+d/c))/\tau}. \end{aligned} \tag{2.86}$$

The unit step functions define the limits of integration of all the equations of type Eq. (2.86), which range from $t_1 + \frac{d}{c}$ to the minimum of $t_2 + \frac{d}{c}$ and $t - \frac{d}{c}$. In order to use the same time-reversal window for each iteration, I use $t_2 + \frac{d}{c}$ as the upper limit of integration. This is a result of defining the time-reversal window by the interval between t_1 and t_2. This yields for the second return

$$\begin{aligned} f_2(t) &= g_0 u\left(t - \left(t_1 + \frac{2d}{c}\right)\right) \frac{\tau}{2} e^{-\frac{t+t_1}{\tau}} e^{\frac{2d}{c\tau}} \left[e^{\frac{2t_2}{\tau}} - e^{\frac{2t_1}{\tau}}\right] \\ &= g_0 A e^{-\frac{t+t_1}{\tau}} u\left(t - \left(t_1 + \frac{2d}{c}\right)\right) \end{aligned} \tag{2.87}$$

where I now define

$$A = \frac{\tau}{2} e^{\frac{2d}{c\tau}} \left[e^{\frac{2t_2}{\tau}} - e^{\frac{2t_1}{\tau}}\right]. \tag{2.88}$$

After using the time-reversal operator on Eq. (2.87) the field incident on the scatterer is

$$g_2(t') = g_0 A u\left(t' - \left(t_1 + \frac{d}{c}\right)\right) e^{-(t'-(t_1+d/c))/\tau} u\left(t_2 + \frac{d}{c} - t'\right). \tag{2.89}$$

Using Eq. (2.89) with Eq. (2.83) yields the scattered field for the observer as

$$f_3(t) = g_0 A^2 e^{\frac{2d}{c\tau}} e^{-\frac{t}{\tau}} u\left(t - \left(t_1 + \frac{2d}{c}\right)\right). \tag{2.90}$$

Equation (2.90) should be the stable waveform, which will be demonstrated by performing the time-reversal operation two more times on Eq. (2.90). The fourth return is

$$\begin{aligned} f_4(t) = g_0 A^3 e^{\frac{2d}{c\tau}} e^{-\frac{t}{\tau}} e^{-\frac{t_1+2d/c}{\tau}} u\left(t - \left(t_1 + \frac{2d}{c}\right)\right) \\ = f_3(t) A e^{\frac{t_1+2d/c}{\tau}}. \end{aligned} \tag{2.91}$$

And performing the time-reversal operation on $f_4(t)$ yields for the fifth return

$$\begin{aligned} f_5(t) = g_0 A^4 e^{\frac{2d}{c\tau}} e^{-\frac{t}{\tau}} \left(e^{-\frac{t_1+2d/c}{\tau}}\right)^2 u\left(t - \left(t_1 + \frac{2d}{c}\right)\right) \\ = f_3(t) \left(A e^{\frac{t_1+2d/c}{\tau}}\right)^2. \end{aligned} \tag{2.92}$$

Both Eq. (2.91) and Eq. (2.92) support the statement that the third return is the waveform that the time-reversal operator converges to using backscattered signals.

2.3.3 Time-Reversal for Spherical Target Backscatter

For the case of a solid sphere in a solid medium, I assume the transverse waves are negligible. Using the impulse response for the backscattered field I can use the backscattered field from Eq. (2.35),

$$\begin{aligned} \psi(\vec{r}, t) = \frac{-D}{\sqrt{4\pi} d} \sum_{k=-\infty}^{\infty} \sum_{l=0}^{\infty} \sum_{s=-l}^{l} \frac{Y_l^s(\theta_c, \phi_c)}{2l+1} \left(\frac{a}{d}\right)^l \left[\frac{(l/a) + i(k+\sigma)}{[k h_l{}'(ka) + i\sigma h_l(ka)]}\right] \\ h_l(kr_c) e^{ikc\left(t - \left(t_O + \frac{d+a}{c}\right)\right)}. \end{aligned} \tag{2.93}$$

The above signal is recorded over a time interval, T, then time reversed resulting in the transmitted signal

$$\psi(\vec{r}_O, T) = \frac{D}{\sqrt{4\pi}d} \sum_{k=-\infty}^{\infty} \sum_{l=0}^{\infty} \frac{(-1)^{l+1}}{2l+1} \left(\frac{a}{d}\right)^l \left[\frac{(l/a) + i(k+\sigma)}{[kh_l\,'(ka) + i\sigma h_l(ka)]}\right] h_l(kd)\, e^{ikc\left(-T + \left(t_O + \frac{2d+a}{c}\right)\right)}, \tag{2.94}$$

which I will rewrite as

$$\psi(\vec{r}_O, T) = \sum_{k=-\infty}^{\infty} B_{k,l}\, e^{ikc\left(t_O + \frac{2d+a}{c}\right)}. \tag{2.95}$$

where

$$B_{k,l} = \frac{D}{\sqrt{4\pi}d} \sum_{l=0}^{\infty} \frac{(-1)^{l+1}}{2l+1} \left(\frac{a}{d}\right)^l \left[\frac{(l/a) + i(k+\sigma)}{[kh_l\,'(ka) + i\sigma h_l(ka)]}\right] h_l(kd). \tag{2.96}$$

Propagation is accomplished by multiplication with the Green's function

$$G(\vec{r}_c, t) = \frac{\delta(t - \frac{|\vec{r}_c| + d}{c})}{|\vec{r}_c| + d}. \tag{2.97}$$

Performing the same expansion as was done to obtain Eq. (2.29) gives the time reversed field incident on the sphere as

$$\psi_{inc}(\vec{r}, t) = \sum_{k=-\infty}^{\infty} \sum_{n=0}^{\infty} \sum_{m=-n}^{n} B_{k,l} \frac{Y_n^m(\theta_c, \phi_c)}{\sqrt{4\pi}(2n+1)} \frac{r_c^n}{d^{n+1}} e^{ikc\left(t - \frac{|\vec{r}_c| + d}{c}\right)} e^{ikc\left(t_O + \frac{2d+a}{c}\right)}. \tag{2.98}$$

As in the analysis for the field scattered off a sphere, I write the scattered field as Eq. (2.28). Using the proper boundary condition and mathematics, the backscattered field becomes

$$\psi_{sc}(\vec{r}, t) = \sum_{k=-\infty}^{\infty} \sum_{n=0}^{\infty} \sum_{m=-n}^{n} -B_{k,l} \frac{Y_n^m(\theta_c, \phi_c)}{\sqrt{4\pi}(2n+1)} \frac{a^n}{d^{n+1}} \frac{(n/a) + i(k+\sigma)}{kh_n\,'(ka) + i\sigma h_n(ka)} h_n(kr_c) e^{ikc\left(t + t_O + \frac{d}{c}\right)}. \tag{2.99}$$

The transceiver records the above at its location over another time interval T

$$\psi(\vec{r}_O, T) = \sum_{k=-\infty}^{\infty} \sum_{n=0}^{\infty} \frac{B_{k,l}}{4\pi d} \frac{(-1)^{n+1}}{\sqrt{2n+1}} \left(\frac{a}{d}\right)^n \frac{(n/a) + i(k+\sigma)}{k h_n{}'(ka) + i\sigma h_n(ka)} \\ h_n(kd)\, e^{ikc\left(t_O + \frac{2d}{c}\right)}. \tag{2.100}$$

The important difference between Eq. (2.100) and Eq. (2.95), is that the radius of the sphere, a, is not in the exponent. It will return during the next time-reversal iteration, introducing a small oscillatory phase shift that will only occur when the sphere is present. With the expression for $B_{k,l}$ in mind, it appears that the amplitude of the field increases by multiplying with itself. This is not the case, but what is happening is the coefficients are being re-expanded during each iteration of the time-reversal operator. The end result is that the coefficients of the expansion converge to coefficients associated with the scatterers. This is a process of selection that is inherent in the time-reversal operator. From the structure of the returns it is the spatial components of the signal that are being enhanced, not the temporal components. The windowed effects as listed in (2.3.2) are apparent.

2.4 Figures

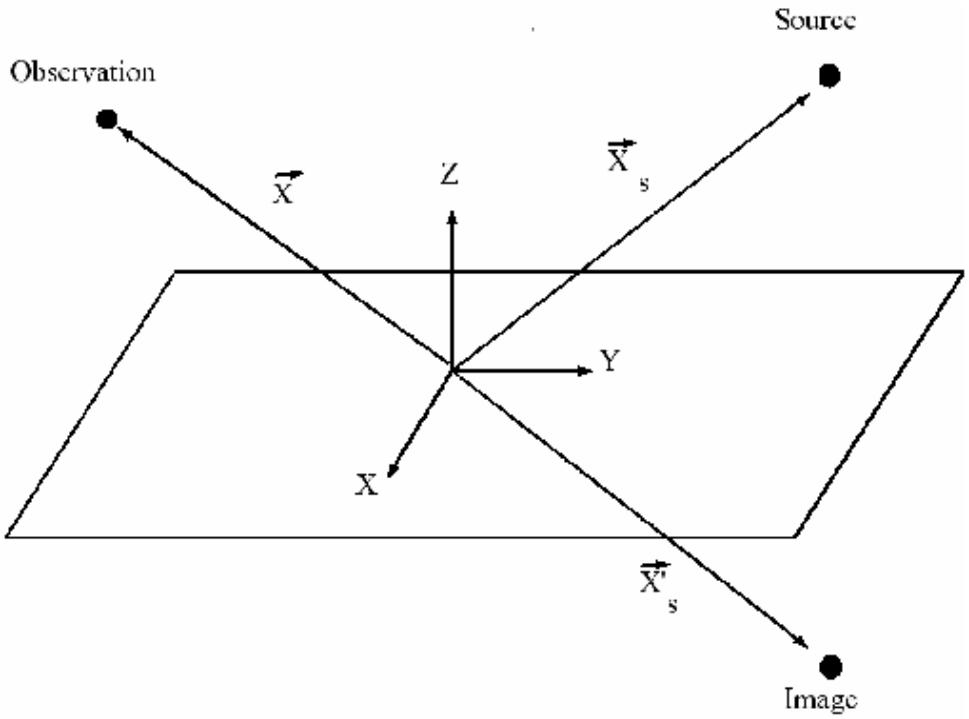

Figure 2.1: The geometry used in the calculations. The point source is always in the less dense medium. Because of the azimuthal symmetry of the medium, cylindrical coordinates provide the simplest description.

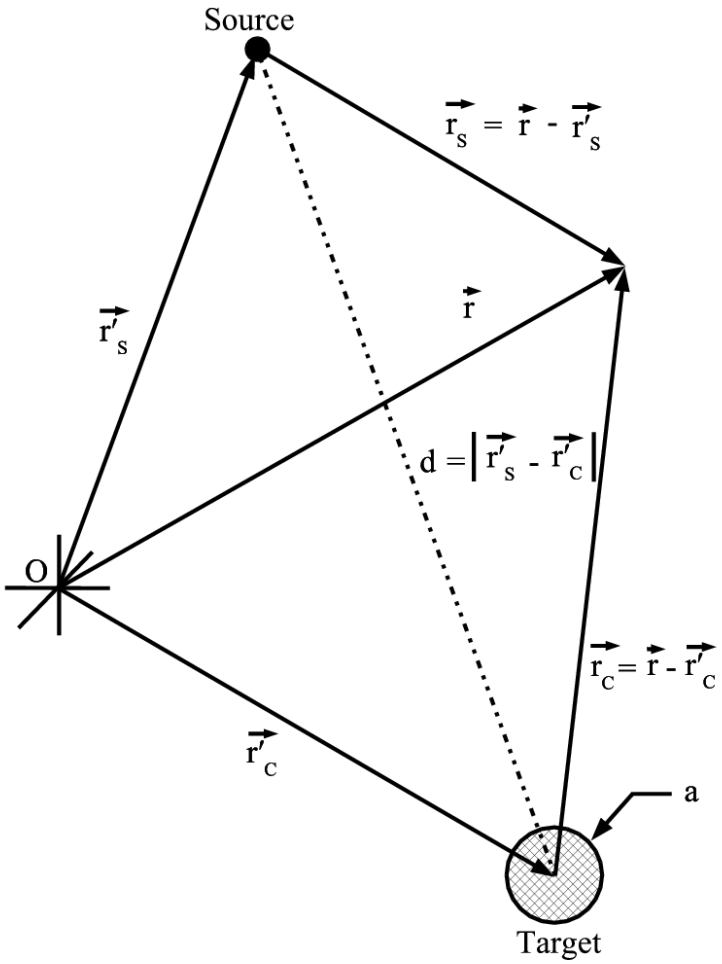

Figure 2.2: The geometry I use to calculate scattering from a sphere. Since I am interested in the response from the sphere at the source location, I only need to carry the calculations for the monopole term. Since I make the source omni-directional, normal incidence along the line between the center of the sphere and the source can be assumed.

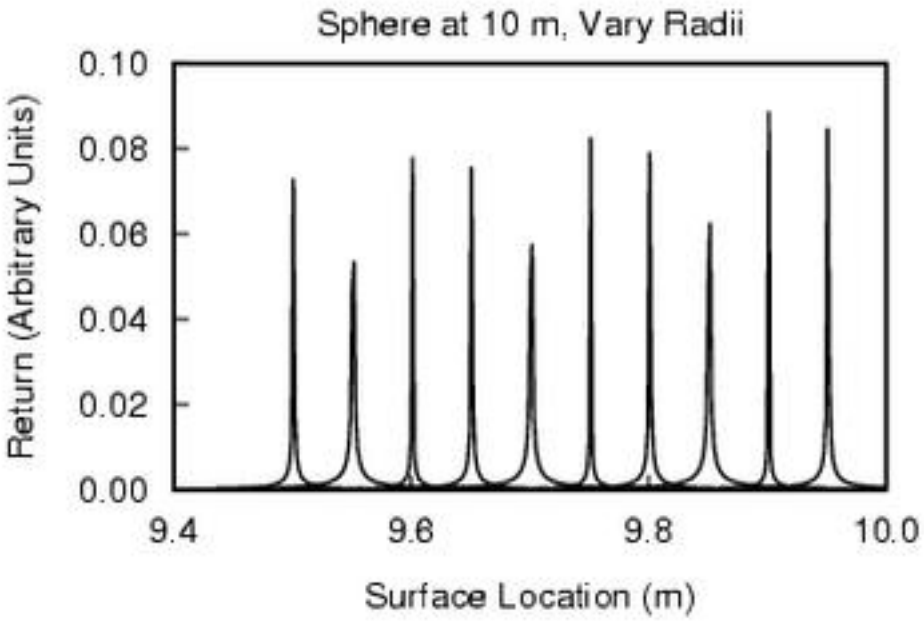

Figure 2.3: Responses with the separation between the center of the sphere and the detector fixed at 10 m while the radius of the sphere is varied from 0.05 m to 0.5 m. The results show that the impulse is created at the location of the surface of the sphere. The oscillations in the amplitudes are from the interaction of the exponentials and the spherical Hankel functions in Eq (2.37). Some peaks are defined by the term (d-a) in the exponentials and others by ratios of the spherical Hankel functions.

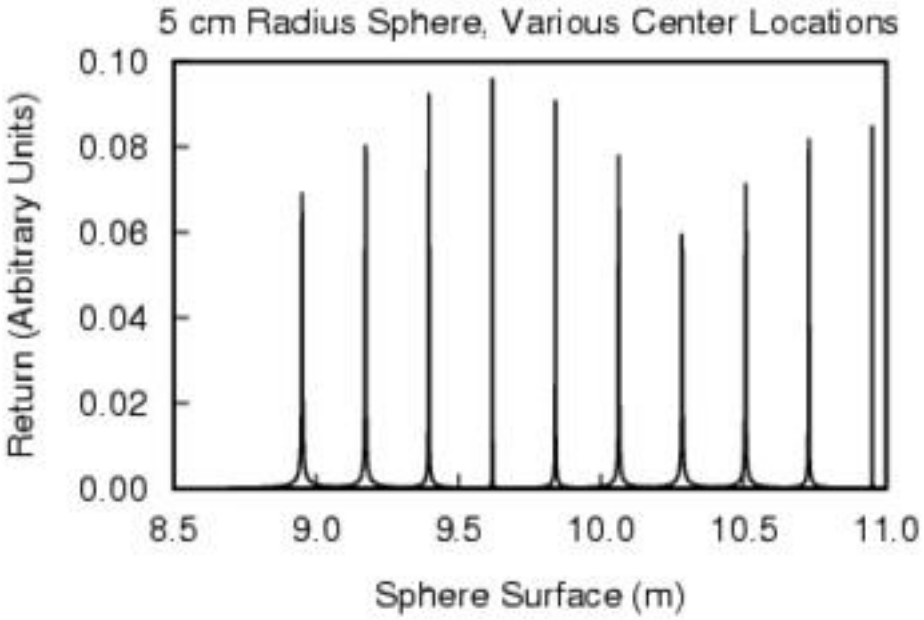

Figure 2.4: Responses for the radius of the sphere fixed at 5 cm while the center of the sphere is moved from 9.0 to 11.0 m. The results show that the surface closest to the sphere dominates. The oscillations in the amplitudes of the peaks are due to the spherical Hankel functions $h_0(kd)$.

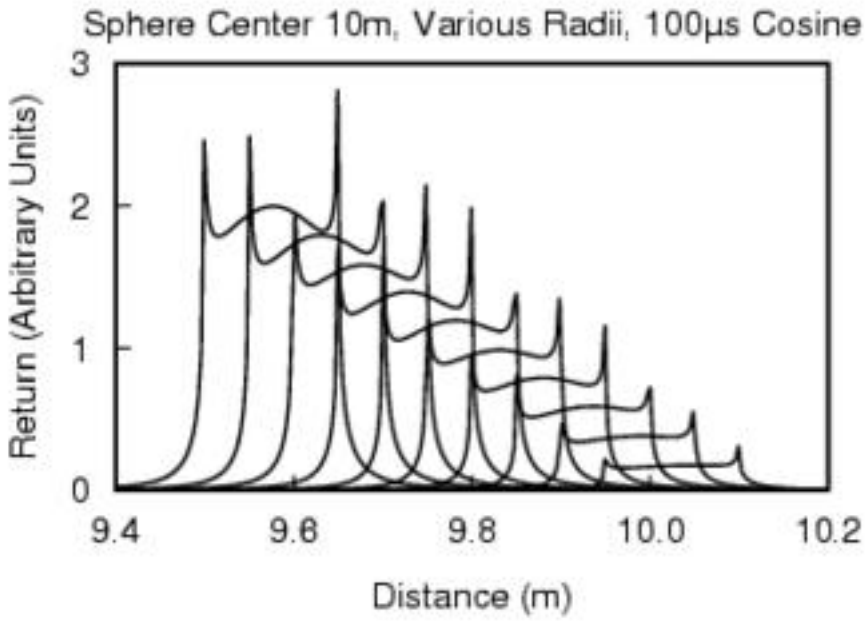

Figure 2.5: Responses with the location of the sphere centered at 10 m from the detector and the radius from 5 to 50 cm. These shapes result from a one cycle cosine pulse with a duration of 100 μs. Notice that the left side of the waveforms are at the location of the surface of the sphere. The small oscillation at the top of each waveform is due to the shape of the pulse.

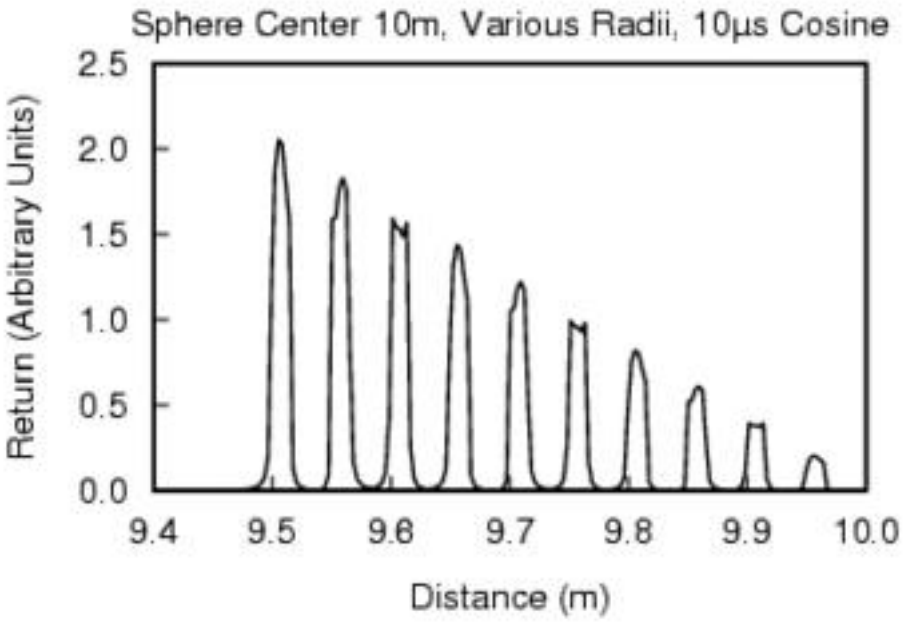

Figure 2.6: Response for the location of the sphere centered at 10 m from the detector and the radius varied from 5 to 50 cm while the duration of the pulse is changed from 100 to 10 μs. The results show that the ability to find the location of the surface of the sphere is not compromised. The small oscillation at the top of each waveform is not noticeable since the pulse duration has gone from 100 to 10 μs while the time step is kept at 1 μs.

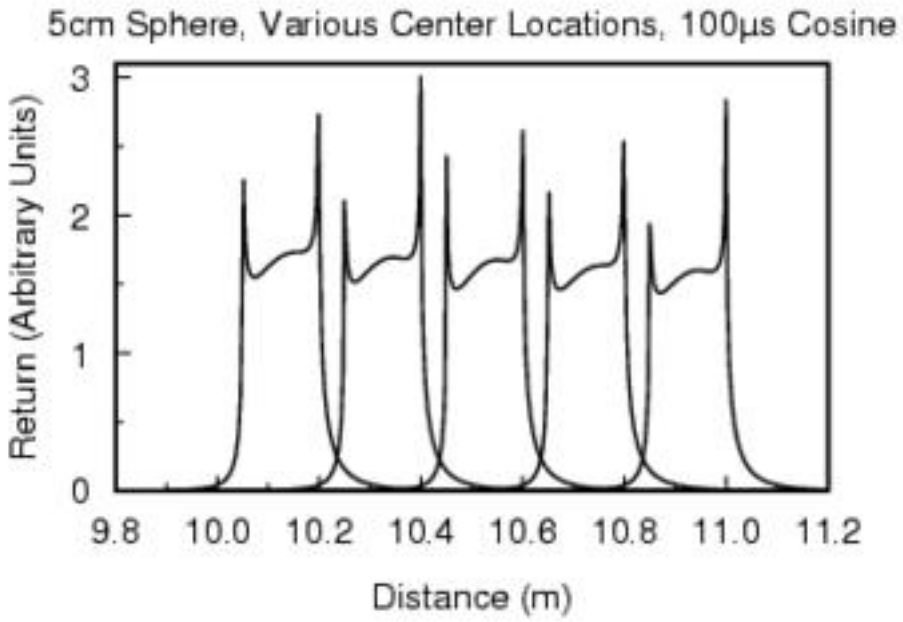

Figure 2.7: Responses with the radius of the sphere fixed at 5 cm and the center moved from 10.1 to 11 m in steps of 0.1 m. The 100 μs one-cycle cosine pulse again gives the distance to the surface of the sphere, as noted by the left edge of the responses above. The oscillation at the top of the returns is from the cosine pulse while the horns at the top of each pulse are from the rectangular window used to limit the length of the pulse.

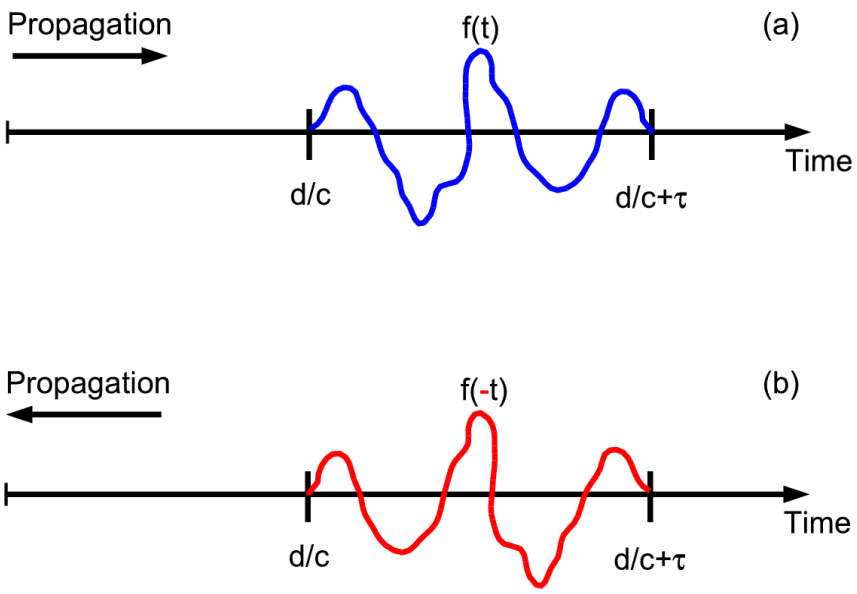

Figure 2.8: The basic idea behind time reversal is to transmit an as-received signal recorded by the time-reversal mirror in reverse temporal order. If the medium is aberrating, the original pulse shape will be recorded at the source location.

Chapter 3

Simulations and Interpretations

3.1 Introduction

Time reversal (TR) has been shown to be effective in the water column to focus an acoustic signal on a source [13], [16] and through inhomogeneous media [18], [19], [17] in the forward scattering direction. However, for the backscattered signal from a target it has not been studied. The work presented here shows that time reversal using a temporal segment of the signal, referred to as a window, of the acoustic return does not improve the signal-to-noise ratio of the backscattered return after the first iteration over all frequencies. However, windowed time-reversal operator (wTRO) can improve the signal-to-noise ratio over frequency ranges that contain the target information, and that enhancement can be tailored to match the frequency response of the system. A windowed iterative time-reversal operator (iTRO) further improves the quality of the return from a target. This chapter presents the results of simulations and the interpretation of the results. I also include a section to describe the model used for the simulations. As with any model and simulation, approximations are made so the calculation can be done numerically. However, I keep the assumptions as close as possible to what is reasonable for real world experiments.

This chapter is organized as follows. It begins with a brief section that describes the model and explains the assumptions used along with the modifications made so

it can be applied to this experiment. The next section describes the simulations and explains why this configuration was chosen. Then the data from the simulations will be presented followed by an explanation of the results. I will finish with a commentary on the results in conjunction with the theory presented in preceding chapter.

3.2 Model

The model used for these simulations was obtained from G. Canepa, O. Bergem, and E. Pouliquen [31]. It was tested by comparing the response from the seafloor of the Gulf of La Spezia, Italy [33]. Quite good results were obtained. The model is known as Bottom Response to Inhomogeneities and Surface (BoRIS) and uses the following assumptions and approximations:

- The seafloor surface and volume are composed of an infinite number of sub-elements that have periodic boundaries. This allows the model to use only a finite number of elements in order to calculate the backscattered return.
- The surface roughness satisfies the Kirchhoff approximation to avoid sharp corners causing shadow effects.
- The environment is not dynamical.
- The seafloor surface roughness and volume inhomogeneities are generated by stochastic fluctuations about median RMS values.
- The size of the inhomogeneities are described by correlation lengths in both the horizontal and vertical direction.
- The source and receiver are co-located and assumed to be a point.
- The returns are determined from a conic cross-section where the angles are represent the pitch, θ, and roll, ϕ, of the source. The pitch angle is along the east and the roll is along the north.
- The ocean environment has cylindrical symmetry so only vertical and horizontal directions need to be considered.

The simulations calculate the surface and volume returns separately. The units for the return are pressure normalized by 240 kPa at 1m.

For the simulations presented here, the temporal sampling of the returns was set to 1 MHz. 10 MHz was used for a few situations to test the model with the result that unnecessary noise was introduced in the returns. The smallest seafloor element had a size corresponding to 1 cm. Scatterers were treated as cubic elements with a side of 1 cm with the acoustic properties of the sediment. The acoustic properties of the sediment are treated as a multiplicative function to the response as

$$\mu\left(\vec{r}\right) = \frac{c\left(\vec{r}\right) - \bar{c}}{\bar{c}} + \frac{\rho\left(\vec{r}\right) - \bar{\rho}}{\bar{\rho}}. \tag{3.1}$$

In above equation $c\left(\vec{r}\right)$ and $\rho\left(\vec{r}\right)$ are the sound speed and density at location $\vec{r}$, respectively and $\bar{c}$ and $\bar{\rho}$ are the corresponding average values. The fluctuations in the volume are calculated based on correlation lengths that are entered by the user. In real environments the inhomogeneities in the seafloor vary more in the vertical direction than in the horizontal. As a result, Eq. (3.1) is calculated for each point based on the correlation lengths in both the vertical and horizontal directions entered by the user. Attenuation, β in the volume is assumed to be a function of frequency, f, as $\beta = |\alpha| f$ where α is a real constant attenuation term.

To introduce a target of known composition and geometry the model needed to be modified by inserting a different volume cube at a specific location. For the present work, the location of this alternate volume the center of the target relative to the point source. The target was inserted in a copy of the base volume element using Eq. (3.1) to describe its acoustic properties. To calculate μ of Eq. (3.1) for the target set I set $c\left(\vec{r}\right)$ and $\rho\left(\vec{r}\right)$ to the sound speed and density of the target while keeping the average values to those of the surrounding medium.

3.3 Simulation Parameters

For the simulations various pulses shown in Fig. 3.1 were tested. Most of the study used the one-cycle cosine pulse of 10 μs duration, which corresponds to the

lower frequency limit used for most side-scan sonar systems. Two sine pulses of one cycle were used; one of 10 μs duration to show that there is little difference between the two initial pulses after a few iterations of the time reversal operator, and the other with a duration of 100 μs. The 100 μs pulse shows that increasing the period of the initial pulse makes the target more difficult to detect, but after approximately 20 iterations the return from the sphere becomes similar to that seen with the 10 μs pulse. Two sine-squared pulses were used, one of a single cycle with a duration of 100 μs and the other with two cycles over the same time interval. One cycle was used in most scenarios since using more than one cycle would just increase the amount of power in the system without improving the understanding the process.

Two sediment types were studied. One was a mixture of 80% sand and 20% silt. Most of the studies were performed on this since it had contributions from two sediment types only. The other was a composition representing sediment from Harbor Station, which is near the Cape Fear Inlet in North Carolina [38] and is more geologically complex. The target was an iron sphere located so its surface was 10 cm beneath the surface of the seafloor. Iron was chosen since most artificial targets of interest contain either iron, steel, or some iron alloy. However, any target that is acoustically hard compared to the surrounding environment would provide similar results. A sphere was used as a first-order approximation to an artificial target, and the scattering theory for a sphere is well known [28], [29], [37], [39]. This is expected to capture the main results; modification of the spherical shape would be expected to result in only higher-order corrections. The depth was chosen since most objects that rest on the seafloor will eventually be covered by a layer of sediment approximately that thick. It also makes the problem more interesting since the backscattered signal will have contributions from both seafloor and the target.

Sphere diameters of 2, 6, and 10 cm were studied to test the limits of the efficacy of windowed time reversal to enhance the returned signal. In realistic situations, the target diameter will be greater than 10 cm [8]. Two source/target geometries were studied to contrast the case of normal incidence to non-normal incidence. In

both cases the average distance from the source to seafloor was 10 m. The normal-incidence study placed the target directly below the source while the non-normal geometry placed the center of the sphere 7.05 m horizontally away from the normal axis. This distance was chosen for two reasons: first, it sets the angle between the normal and the axis connecting the center of the sphere to the source at 35°. Second, this is very close to the angle for which there is no backscatter from the seafloor as described in Sec. B.2.2 and [40]. The conic section used to calculate the responses are for the pitch angle $-10° \leq \theta \leq 10°$ and the roll angle $-1.5° \leq \phi \leq 1.5°$. For normal incidence the region of insonification is an ellipse of 1.76 m along the east and 0.26 m along the north. For the 35° incidence the region is 5.34 m along east and 0.78 m along north. The penetration of the signal into the seabed was set to 1 m for all the simulations to ensure that there will be a backscattered response from the target.

3.3.1 80% Sand / 20% Silt

I chose a sediment of 80% sand and 20% silt to represent the average of most beaches with sandy seafloors. The response of the seafloor to a 10 μs single-cycle cosine pulse under normal incidence with no sphere present is shown in Fig. 3.2. The black line of Fig. 3.2 shows the first return and the red line is the result of nine iterations of the time-reversal operator (TRO) using the part of the signal bounded by the box labeled "TR Window". Recall the procedure for the TRO as follows:

1. Sample the return within the region in the box. The same region was used for each iteration of the windowed time reversal operator.

2. Reverse the temporal order of the signal.

3. Set the gain to counter any loss in power from propagation. For this work the gain was the inverse of the absolute maximum value, of the return, creating a unity-amplitude time-reversed pulse.

4. Transmit this new signal.

The window used for this series of time-reversal operations starts at 13.3893 ms of the signal and has a duration of 170 μs. This window ensures that the return from the spheres will be included with minimal contribution from the seafloor surface.

With a 10 cm diameter iron sphere buried 10 cm deep the return changes to the black line in Fig. 3.3. The sphere is clearly present as shown by the oscillatory return within the time-reversal window(TRW), but the envelope is not that expected from scattering theory. After nine iterations of the TRO using the 170 μs window the return has the waveform represented by the red line in Fig. 3.3, which does have the shape expected by the backscattered return from a sphere scattering an impulse function. The waveform of the tenth return of Fig. 3.3 as compared to Fig. 3.2 shows that the TRO detects the sphere. There are a few properties that need to be mentioned:

- The convergence waveform is independent of the initial pulse shape.
- The convergence waveform is also independent of the surrounding sediment properties.
- The start time for recording the TRO return and the duration of the time-reversal window determine the signal-to-noise ratio.
- The amplitude of the return from the sphere must be above the threshold of the transceiver and at least marginally greater than the return of the surrounding sediment.
- Performing a low-pass filter function on each iteration of the TRO only serves to decrease the signal-to-noise ratio.

Initial Pulse Shape

To determine what effect the initial pulse shape has on the returns, I used the pulses shown in Fig. 3.1. The 10 μs single-cycle cosine pulse is shown as the black line, the 10 μs single-cycle sine pulse is the red line. The reasoning to switch from cosine to sine was to minimize the oscillations in the first return, as in the black line in Fig. 3.3, which could have been an artifact of the discontinuity of the cosine envelope. However, by comparing the black line in Fig. 3.3 to that of Fig. 3.4 we find

that the oscillations are due to the wavelength of the pulse, which is approximately 1.6 cm using a sound speed of 1600 m/s. Thus both the 6 and 10 cm diameter spheres will be detected with these pulses. Using any of the 100 μs single-cycle pulses or the double-cycle pulse shows that the TRO allows the 10 cm sphere to be detected after a few iterations. This is demonstrated by Fig. 3.5, which shows the result of forty-nine iterations of the TRO using the 170 μs time-reversal window. Comparison of the red lines from Figs. 3.4 or 3.6 to 3.5 shows that the TRO improves the return from the sphere especially when the first return shows that it is barely detected. Figure 3.6 shows the first return from the 100 μs single-cycle sine pulse normally incident on the seafloor with the 10 cm sphere present, red line, and without, black line, showing that the sphere is barely discernible from the sediment. However, after forty-nine iterations of the TRO the sphere is easily distinguishable, as shown in Fig. 3.7. As in Fig. 3.6, the black line is the return of the sediment alone and the red is the return with the 10 cm diameter iron sphere present. This improvement in the target return can also be seen in the frequency spectra of the returns as shown in Fig. 3.8 where I plot the spectra from the first return of the 10 cm diameter iron sphere,black line, from Fig. 3.6 and the fiftieth return, red line, from Fig. 3.7. The peak in the spectra at 82 kHz is entirely from the sphere. Thus even though the initial pulse barely detects the target, the TRO eventually yields a strong target signal.

The reason why the iTRO generates the same waveform independent of the initial pulse is that during the iTRO the Fourier-Bessel components associated with the strongest scatterer, in this case the sphere when present, are being selected through re-expansion of the coefficients in the scattering process. Two factors limit what frequencies remain after each re-expansion, one is the sampling rate of the transducer which sets the high frequency limit. The other is absorption of certain frequencies by the propagating environment. The characteristics of the main scatterer dictate what components will be sorted out by the iTRO. Recall the derivation from Sec. 2.3.3, where I show that each iteration of the TRO yields a re-expansion of the Fourier-Bessel coefficients of the backscattered field. Those coefficients depend on the separation

between the source and the center of the sphere and the radius of the sphere.

Time Averaged SNR

To simplify the results of this study and quantify the improvement in the SNR I define the signal-to-noise ratio (SNR) as

$$SNR = \frac{\int_T (s(t) - n(t))^2 dt}{\int_T n^2(t) dt} \tag{3.2}$$

where s(t) is the return with the target sphere, n(t) is the return from the sediment without the sphere and T is the time over which to integrate. Using this definition of the SNR gives a more direct method to quantify the efficacy of the TRO without needing to generate plots for each iteration. Under normal incidence the 10 μs single-cycle cosine pulse results in SNR curves shown in Fig. 3.9 where the circles are for the 10 cm sphere and the diamonds are for the 6 cm sphere. The SNR for both the 6 and 10 cm diameter spheres appears to improve for the second and third returns after using the wTRO twice after which the SNR decreases. The normal incidence response from a 2 cm diameter sphere could not be detected, which is not surprising since 2 cm is of the order of the dimension of the inhomogeneities. Figure 3.10 shows the SNR for the 10 μs cosine pulse at 35° incidence and demonstrates that the wTRO improves the SNR independently of angle of incidence. The SNRs from Fig. 3.10 shows that the SNR qualitatively converges in the same manner independent of sphere diameter. The exception of the SNR from first return of the 10 cm sphere which is gives a strong response and then degrades due to the window duration. As shown in Fig. 3.11 the SNR converges rapidly as a function of return number and remains stable thereafter. The convergence to a single SNR value is also independent of initial pulse used as shown in Fig. 3.12 where I plot the SNR from the 10 μs and 100 μs single-cycle sine pulses normally incident on the 10 cm diameter sphere. Target size has the effect of changing the convergence value provided that the sphere can be detected. The oscillations at high return iteration numbers are from the interaction

of the exponentials and the spherical Hankel functions from the expansion given by Eq. (2.100) of Sec. 2.3.3.

Pulses and Filters

The various pulses shown in Fig. 3.1 all give SNRs that are similar to those shown in Fig. 3.11 since after several iterations of the wTRO the returns converge to similar waveforms independent of the initial pulse, as seen in Fig. 3.25. In Fig. 3.25 we have the SNR as defined by Eq. (3.2) for the 10 μs cosine pulse, black for full pass (FP) filtered and green for low pass (LP) filtered responses, and for the 10 μs sine pulse, red for FP filtered and blue for LP filtered using the 170 μs time reversal window in all cases. The low pass filter used a rectangle function in frequency space to 4.9 kHz then a half-cosine for 4.9 to 17.6 kHz. Use of this filter on the time-reversed signal lowers the SNR most noticeably for the cosine pulse, compare the black and green lines, because it removes all high frequency components from the time-reversed signal. The relative increase in the SNR when changing from the cosine pulse to the sine pulse is attributed to the window used to generate the initial pulse. Both pulses, as for all the pulses used in this study, use a rectangle convoluted with the continuous pulse train resulting in the cosine pulse starting fully on then decreasing while the sine pulse starts at zero and smoothly increases. This translates into a cleaner first return from the sine pulse as compared to the cosine pulse as shown in Fig. 3.25.

Increasing the period of the first pulse results in the need to increase the number of iterations of the time-reversal operator before the waveform converges to the waveform from the sphere. Comparing the SNR curves, as defined by Eq. (3.2), in Fig. 3.26 for the 10 μs one-cycle cosine pulse, solid black line, to those from a 100 μs one cycle sine pulse, solid red line, and 100 μs one and two-cycle squared sine, blue and green lines respectively, show that time reversal of the backscattered signal from the 10 cm diameter sphere does indeed improve the SNR from the sphere. Similar results are obtained with the low pass filter used in conjunction with the time reversal operator. Recalling the derivation that led to Eq. (2.68), each iteration of the time-reversal

operator results in a re-expansion of that signal in orthogonal functions over the frequency range defined by the temporal window duration and the temporal sampling rate. These functions will eventually converge to one solution that depends only on the radius of the sphere and to a lesser extent, the distance between the surface of the sphere and the location of the source.

Time-reversal Windows Effects

Since filtering the return after each iteration of the TRO has the effect of negating any benefits from the TRO, I chose to study the effects of changing the start time of the time-reversal window and the duration of the TRW. To do this I use two series of windows. One series is shown in Fig. 3.13, where I plot the response of the 10 cm sphere insonified by the 10 μs single-cycle cosine pulse with the three windows used for this part of the study. The blue box is the original 170 μs window described earlier. The green box is the window of duration of 270 μs starting at 13.3893 ms, and was chosen to study how a longer recording time affects the wTRO. The red box is a window of 99 μs starting at 13.4393 ms to study the effects of not having all the information about the target in the window. The corresponding SNRs using these windows are shown in Figs. 3.14 for the 10 cm diameter sphere and 3.15 for the 6 cm diameter sphere, both responding to the 10 μs single-cycle cosine pulse at normal incidence. Changing the duration of the time reversal window from 170 μs to 270 μs does not appreciably change the results for either the 10 cm sphere (Fig. 3.14) nor the 6 cm sphere (Fig. 3.15). This should be expected since the two windows include the leading edge of the target return, which is important for the time-reversal operator although it includes some information from the sediment above the target. Changing the window start time from 13.3893 ms for the 170 μs to 13.4393 ms for the 99 μs window shows quantitatively the same shape of the SNR for both the 10 cm (Fig. 3.14) and 6 cm (Fig. 3.15) spheres. The SNR is greater for the 99 μs window as compared to the 170 μs window, which can be explained using Figs. 3.13 and 3.16. Figure 3.13 shows that for the 99 μs window the first part of the time reversed signal

for the target changes more rapidly than the beginning of the 170 μs time reversed signal. This introduces higher frequency components and results in a second return for the 6 cm sphere that is in Fig. 3.16. Notice in Fig. 3.16 that the 170 μs and 270 μs windows produce nearly identical waveforms since the information from the sediment is present in the first part of the returns while the 99 μs window produces a waveform consisting of high frequency components that are consistent with scattering off the sphere.

Since the SNR used is defined by Eq. (3.2) we also need to see what is happening to the return from the sediment without a target for all the windows presented. Figure 3.17 shows the fifth return from the sediment without a target at normal incidence using the three windows. It is not surprising that the 170 μs and the 270 μs returns give nearly the same waveform since they both start at the same point in the return record and the 99 μs window gives a completely different result since it is not recorded until a later time than the other two windows. Comparison of Fig. 3.17 with the fifth return at normal incidence from the 6 cm sphere (Fig. 3.18) shows why the SNR is larger for the 99 μs window than for both the 170 μs and 270 μs windows. The 99 μs window in Fig. 3.18 contains less sediment return than the other two windows. From this discussion we can say that the SNR is affected by the start time for the TRO while it is relatively unaffected by the duration. In contrast, with the 10 cm diameter sphere the wTRO converges to nearly identical waveforms for the 99 μs window, red line, versus the 170 μs window, black line, as shown in Fig. 3.19. This is due to the size difference in the sphere relative to the duration of the window.

For the second wTRO study, I centered the windows about the same point in the time record at 13.4733 ms and set the length of the window at 50, 100, 150, and 170 μs. Figure 3.20 shows the windows used with respect to the first return from the 6 cm diameter iron sphere using the 10 μs single-cycle sine pulse at normal incidence. All windows include information about the sphere. The SNR for the 10 cm sphere insonified by the 100 μs single-cycle sine pulse at normal incidence, Fig. 3.21, shows that there is a strong dependence on window duration and SNR. The 50 μs window,

shown in red, shows the most complex behavior of the SNR due to the fact that this window contains only sphere location information with very little size information. As the windows become larger, more information about the sphere size is available. This trend continues until there is too much information about the sediment. This behavior is qualitatively independent of sphere size by comparing Fig. 3.22 for the 6 cm diameter sphere using the configuration as in Fig. 3.21. Both the 50 and 100 μs TRWs increase the SNR from the 6 cm sphere. If the window is too large, small spheres cannot be detected. This is shown in Fig. 3.23 where I plot the fiftieth return from the 6 cm sphere using the 100 μs single-cycle sine pulse. The black line uses the 150 μs TRW and the red is from the 50 μs TRW. This makes sense when you realize that the longer TRWs will record more of the sediment return when windows are centered about the same instant. Note that the wavelength of the 100 μs single-cycle sine pulse is more than twice as long as the diameter of the 6 cm sphere. This enforces the idea that the TRO can be used to locate targets whose dimensions are in principle too small to be detected as long as the TRO is centered near the center of the return from the target and has a minimal amount of return from the surrounding medium.

The 10 μs single-cycle sine pulse at normal incidence to the 6 cm sphere shows radically different behavior with window duration, as shown in Fig. 3.24. The 50 μs TRW gives similar results for both the 10 and 100 μs single-cycle sine pulses. The sphere is detected using either the 150 or 170 μs TRWs. TRWs that are greater than 50 μs should give new results for the smaller initial pulse since we now have an initial pulse wavelength that is of the order of the diameter of the target sphere. What is surprising is that the 150 μs window constantly decreases the SNR while all the other windows converge to one SNR value. The other windows converge to different SNR values based on window dimension, the longer the TRW the higher the SNR. This is just a result of the fact that the TRO is picking up more information about the target with each iteration as the window dimension increases.

Frequency Dependent SNR

Since the returns are oscillatory it is worth discussing what the windowed time-reversal operator is doing in frequency space. This will also assist in understanding why the wTRO does not improve the SNR for each iteration. Calculations of the absolute value of the Fourier transform of the returns shown in Figs. 3.2 and 3.3 show that for both the sediment and the target, in this case the 10 cm sphere, the wTRO affects only certain frequency components (Fig. 3.27). Indeed, the peak centered near 80 kHz from the first return of the sphere (green line) is strictly from the sphere while the small hump about 20 kHz is in first return from both the sediment and sphere. Nine iterations of the wTRO using the 170 μs window increases the 80 kHz peak from the sphere (blue line) and suppresses the two peaks co-centered about 20 kHz from the sediment (red line). This leads to the idea of using a frequency-dependent signal-to-noise ratio.

We define such a signal-to-noise ratio $SNR(B_i)$ as

$$SNR(B_i) = \frac{\int_{\nu_i}^{\nu_i+\Delta\nu}(S(\nu) - N(\nu))^2 d\nu}{\int_{\nu_i}^{\nu_i+\Delta\nu} N^2(\nu) d\nu} \tag{3.3}$$

where $B_i = \nu_i + \Delta\nu$ is the frequency interval, $S(\nu)$ and $N(\nu)$ are the Fourier transform of the returns with and without the sphere, respectively. Using Eq. (3.3) for the signal-to-noise ratio gives a surface where one axis is the iteration number, another is the normalized frequency, and the third is the SNR. Setting the frequency step to 5 kHz on the 170 μs wTRO returns using the 10 μs cosine pulse at normal incidence to the 10 cm sphere confirms that the wTRO does improve the SNR if a target is present (Fig. 3.28). The salient features that are present are shown in Fig. 3.27, namely the peak at 80 kHz, 16 on the Normalized Frequency axis, remains through all the iterations of the wTRO. The exception is in the first return where the sediment and sphere returns both share common features which the wTRO distinguishes for future returns. Changing the sphere diameter to 6 cm while keeping all the other variables constant gives a spectrum that makes the sphere much more difficult to distinguish

(Fig. 3.29). The wTRO picks out the peak in the tenth return from the sphere centered near 160 kHz, the blue line in Fig. 3.29, which emphasizes that the wTRO is good at enhancing information from a target in the backscattered signal. The frequency dependent SNR corresponding to Fig. 3.29 shows that the wTRO can be used as a filter to remove the higher frequency components from the SNR (Fig. 3.30). Figure 3.30 shows that the third and fourth returns are optimized to detect the 6 cm sphere. These returns have high frequency components from scattering off the sphere. As the number of iterations increase, the SNR decreases due to the fact that the sediment is absorbing these components since the duration of the time-reversal window is long enough to record more sediment than sphere return.

Off Axis Returns, 35° Incidence

We now consider the geometry where the target is off-axis. The leading surface of the target is still 10 cm beneath the surface, but is now 7.05 m off the normal axis due east relative to the source. This results in an angle of incidence of 35° while the roll and pitch angles, ϕ and θ, will remain the same as stated in Sec. 3.3. Angles greater than 35° result in total loss in the backscattered direction as a result of complete absorption by the second medium [40]. For this study the 10 μs cosine pulse was used and the wTRO was set to start recording at 13.3893 ms for a duration of 170 μs to allow comparisons with the same settings at normal incidence. The targets are again iron spheres with diameters of 2, 6, and 10 cm as in the normal incidence case. Using this geometry there are several differences. The return time of the signal is much longer since the absolute distance from the source to seafloor is now greater. Targets will also appear larger due to refraction of the sound wave. This is the same as the illusion that a quarter appears larger at the bottom of a pool when observed at non-normal incidence.

We recall Fig. 3.10 using the definition for the SNR of Eq. (3.2) for all three targets. As stated previously, this shows that the wTRO does not really improve the SNR over the recording time of the return signal using the definition Eq. (3.2). But the temporal

frequency plots from the first and tenth returns of the 10 cm sphere show that the wTRO does indeed improve the returns from the sediment and sphere (Fig. 3.31) at certain frequencies as in the normal incidence case. The red line in Fig. 3.31 is the tenth return from the sediment alone and has a peak centered approximately at 135 kHz. The blue peaks centered near 165 kHz and 250 kHz are the response from the 10 cm sphere after nine iterations of the 170 μs wTRO. The frequency shift in Fig. 3.31 as compared with Fig. 3.27 is from the refraction of the incident wave making the sphere appear bigger. It is this effect that allows the wTRO to isolate the 2 cm sphere from the surrounding medium. This is shown in Fig. 3.32 where the blue line is the tenth return from the sphere and the red line is the tenth return from the sediment only.

Performing the calculation of the SNR from Eq. (3.3) on the returns from the 10 cm sphere using the frequency step size of 5 kHz, Fig. 3.33, shows that the wTRO is not only stable for this angle of incidence, but keeps the target isolated from the sediment. This behavior is the same as for normal incidence, which leads to the conclusion that as long as there is a backscattered signal from a target in an inhomogeneous medium the wTRO can be used to improve the quality of the return from the target independent of the angle of incidence.

3.3.2 Harbor Station

Acoustic waves and their associated phenomenon are affected by the propagating medium, but the windowed time reversal operator should be independent of these effects. To show that this is the case, a second seafloor environment was modeled using the same 10 μs single cycle cosine pulse as for the 80% sand / 20% silt sediment of the previous section. The targets used are the same iron spheres with the same diameters except that the acoustic parameter $\mu(\vec{r})$ was changed to compensate for the changed values of the averaged sound speed and density of the sediment. Both normal and 35° incidence were studied. The sampling window for the wTRO was set to start at 13.2893 ms with a duration of 170 μs for comparisons between the

two sediments. The parameters from the seafloor to model Harbor Station in the Cape Fear Inlet in North Carolina [38] were used for this part of the study using the parameters listed in Tab. 3.1.

The SNR as defined by Eq. (3.2) shows behavior that is similar for both normal and non-normal (35°) incidence. Figure 3.34 is the SNR calculated over the entire time record for each return at normal incidence for both the 6 cm and 10 cm spheres. Again, the 2 cm sphere did not give a response that was distinguishable from the sediment returns. Figure 3.34 shows that as the number of iterations for the wTRO increases, the SNR increases until about the fifth or sixth return then drops off. This is consistent with the observation that the wTRO converges to a steady waveform for both the sediment and the target so the SNR will remain effectively constant. For the non-normal (35°) incidence, the SNR from Eq. (3.2) shows this same trend which confirms that the wTRO will work independent of the angle of incidence (Fig. 3.35).

Windowed Time Reversal Limit

As implied in Sec. 3.3.1 the SNR from the wTRO reaches a limit where it enhances the return from the 2 cm target. I wish to elaborate some on this point in this section. Figure 3.36 shows the SNR using Eq. (3.2) for the 2 cm diameter iron sphere buried in the Harbor Station sediment at 35° incidence from the source. This figure looks almost identical to the SNR from the 10 cm sphere in Fig. 3.35 with the exception of the vertical scale. The wTRO is not doing a good job of assisting in the enhancement of the target return in this case, which is apparent from Fig. 3.37 where we have used Eq. (3.3) for the SNR and a frequency sampling step of 5 kHz. We see that there is no dominant frequency peak in the SNR in any return, which implies that the wTRO is working with noise. If there was a distinguishable return from the 2 cm sphere the plots in Fig. 3.37 would look more like those in Fig. 3.38 for the 10 cm sphere under the same conditions. From this we can conclude that the wTRO not only needs a return from a target, but the target return must have a higher SNR than that of the sediment to use Eqs. (3.2) and (3.3) to calculate the SNR of the sphere.

3.3.3 Sediment Comparison

The sediments have different behaviors with respect to the signals due to differences in sound speed, density, size of embedded scatterers, and attenuation. For the two sediments studied Tab. 3.2 lists the differences between sound speed, density, and attenuation. These are the most influential parameters in any acoustic model. The return spectra for the tenth return at normal incidence for the 10 cm sphere using the 170 μs wTRO, Fig. 3.39, shows that the differences in the sediment have an effect on the returns. The changes in attenuation and sound speed are reflected in the location of the two peaks since the Harbor Station sediment, red line, allows the higher frequencies to propagate more easily than for the sand-silt sediment, black line. Keeping the 170 μs wTRO and changing the angle of incidence shows that the angle of incidence can be treated as a blue shift in frequency (Fig. 3.40). The difference in sound speed in the two sediments of 50 m/s can introduce a small error in the location of the target that translates to a temporal shift of 0.2 ms per 1 cm position shift. Since the time reversal window used in these simulations were approximately 13.3 to 13.5 ms for normal incidence and 16.3 to 16.4 ms for 35° incidence, it would stand to reason that there would be small discrepancies in the exact location of the center of the sphere from the return time series. However, the figures show the robustness of the time reversal operator to converge to the backscattered signal of a sphere in an inhomogeneous environment.

3.4 Concluding Remarks

The results presented in this chapter show that the windowed time reversal operator has the potential to be a useful tool to determine a target that is acoustically hard compared to the embedded environment. The idea that the time reversal window needs to match exactly the location of the target has been disproved by changing not only the start time for the recording of the sampled signal, but also changing the duration of the recording process. Time reversal in this study did not reproduce

the original pulse from the backscattered return, which was not to be expected from the theory presented in the previous chapter. The result of the iterative TRO is to enhance the Fourier-Bessel response to the incident field when the spherical target is present. This implies that the wTRO can be used to obtain target geometry from the backscattered return that has been corrupted by the inhomogeneities in the sediment. The fact that the wTRO is independent of incident angle shows that this process can be used for targets that not on the normal axis defined by the source and seafloor. The SNR as defined by Eq. (3.2) shows that the wTRO converges to the optimal return after the SNR has reached the maximum for short duration initial pulses. This convergence and the accompanying stability is to be expected from the theory of the iterative TRO [28], [29], [12]. The SNR as defined by Eq. (3.3) shows that the wTRO does enhance the signal from the target.

3.5 Figures and Tables

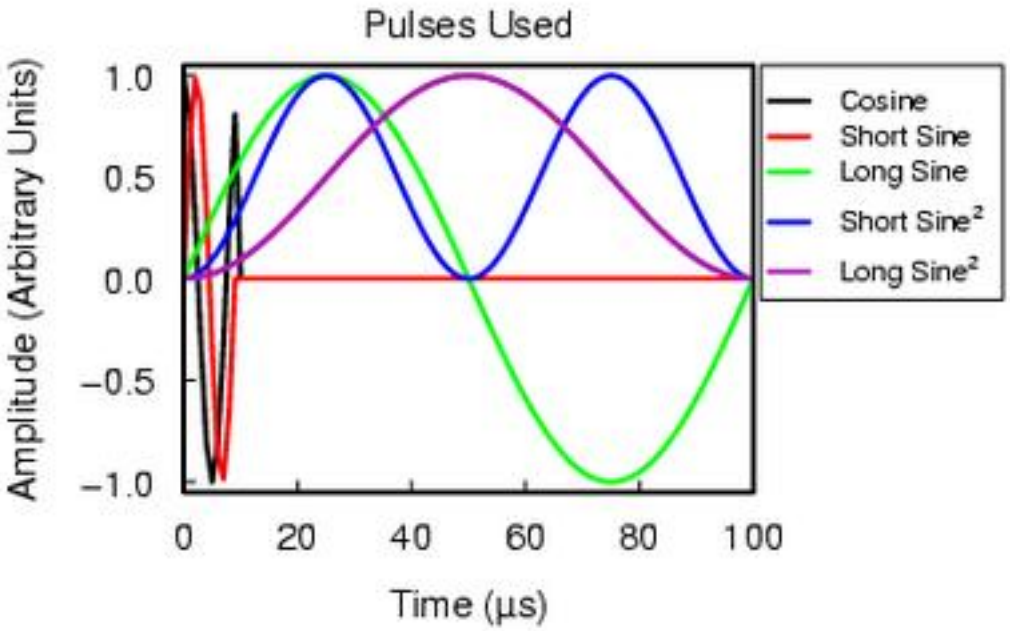

Figure 3.1: Pulses used for the simulations range from a one-cycle cosine pulse of 0.1 ms duration to a one-cycle-squared sine pulse of duration 1.0 ms. After several iterations of the time reversal operator all the initial pulses converge to yield similar results.

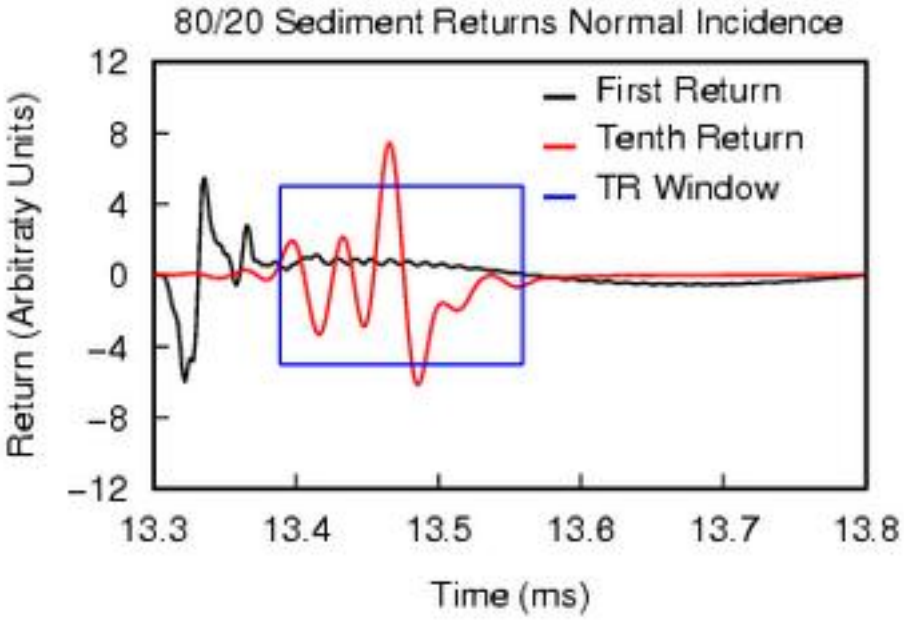

Figure 3.2: Output from the BoRIS simulation using 80% sand and 20% silt without a target for the conditions described in the text. The black solid line is the first return, the red solid line is the tenth return after nine iterations of the time reversal operator. The box shows the temporal boundary used for the time reversal operation.

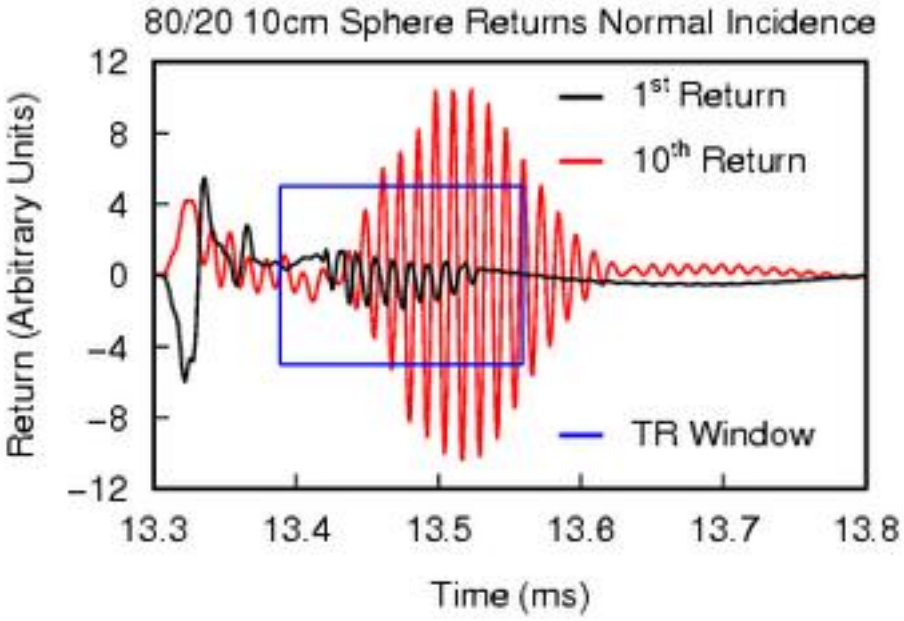

Figure 3.3: Output from the BoRIS simulation with the configuration of Fig 3.2 but also containing a 10 cm diameter sphere. The black solid line is the first return, the red solid line is the tenth return after nine iterations of the time reversal operator. The box shows the temporal boundary used for the time reversal operation.

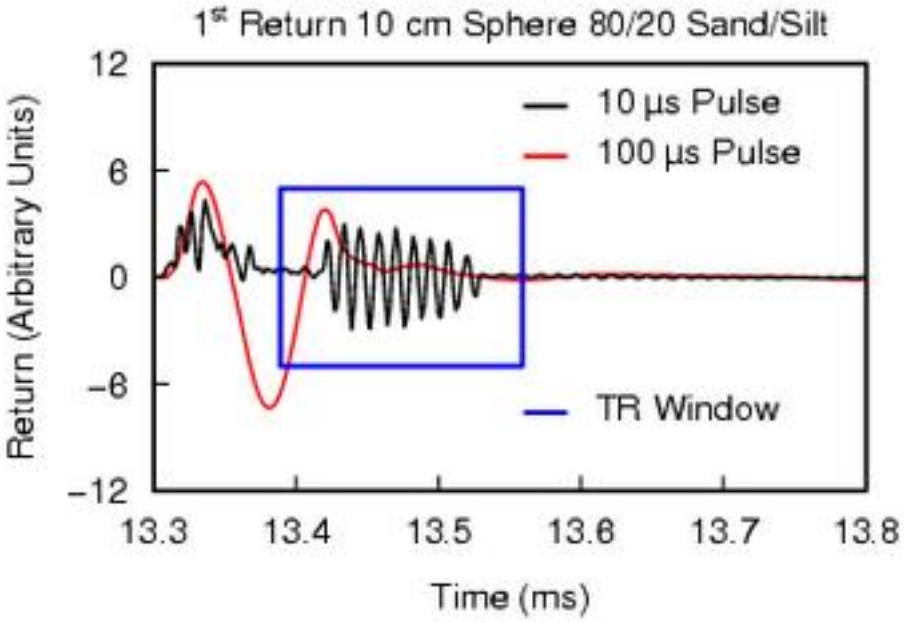

Figure 3.4: To study the behavior of the time-reversal operator for different pulses I looked at the returns from single-cycle 10 and 100 μs sine pulses at normal incidence to the sphere. The figure shows the first return from the 10 μs pulse, black line, and the 100 μs pulse, red line. The shorter pulse detects the sphere where as the longer pulse appears not to detect it within the time-reversal window.

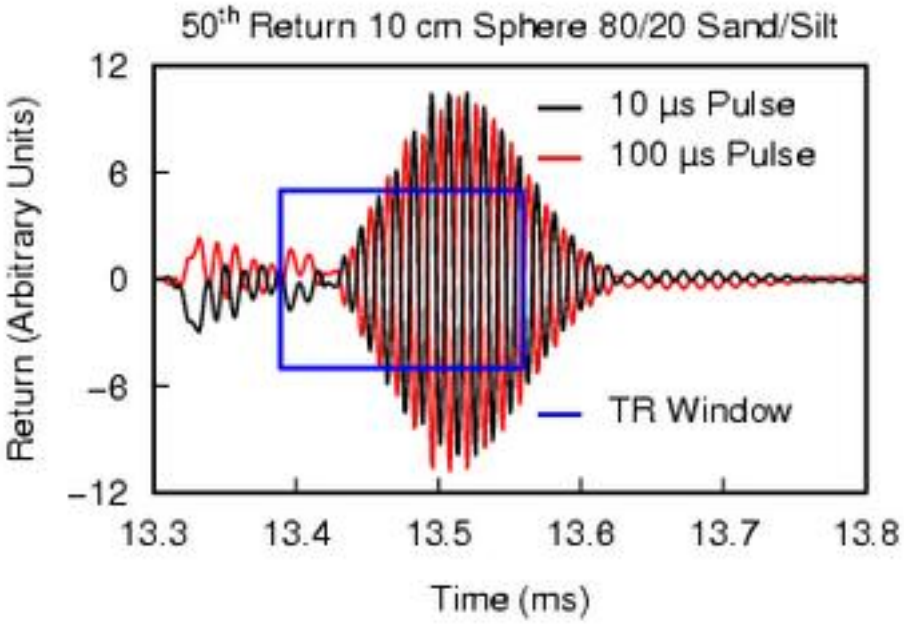

Figure 3.5: The result of forty nine iterations of the time-reversal operator for the single-cycle 10 and 100 μs sine pulses at normal incidence. The sphere is detected by both which converge to the same wave packet, with a small difference in phase that is dependent on the iteration that first has some high frequency components. This alone demonstrates that time-reversal can be useful for the detection of buried targets.

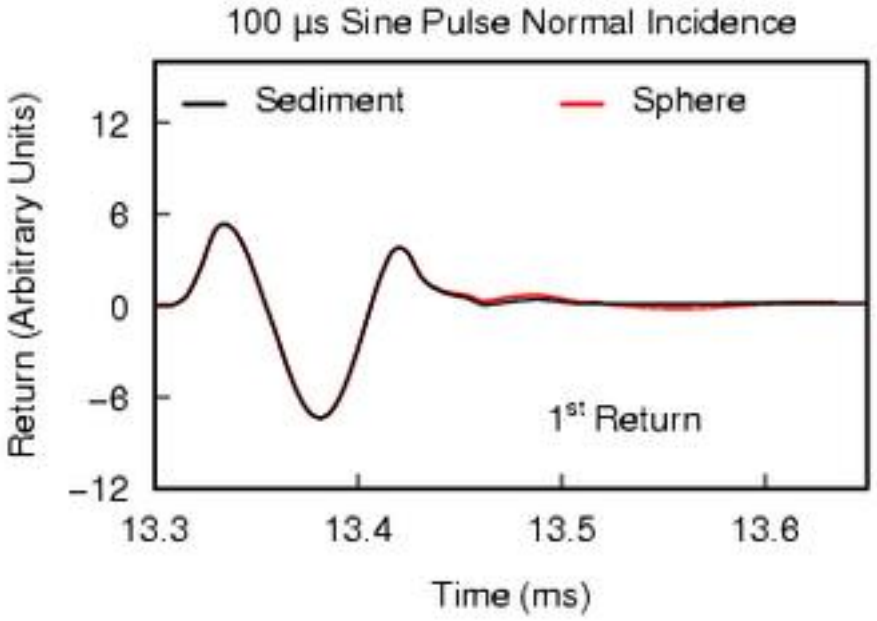

Figure 3.6: First return for a 100 μs single-cycle sine pulse normally incident to the seafloor with (red) and without (black) the presence of a 10 cm sphere. Super resolution may be present, but it only provides a small amount of assistance.

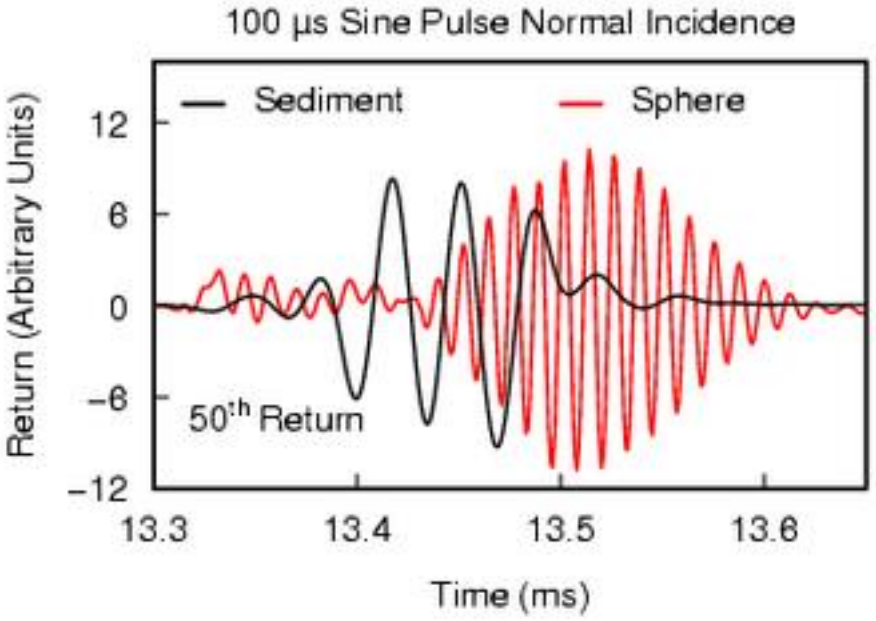

Figure 3.7: The fiftieth returns from the sediment only, black line, and with the 10 cm diameter iron sphere present, red line, show a significant difference. The high frequency wave packet is generated by the scattering response from the sphere.

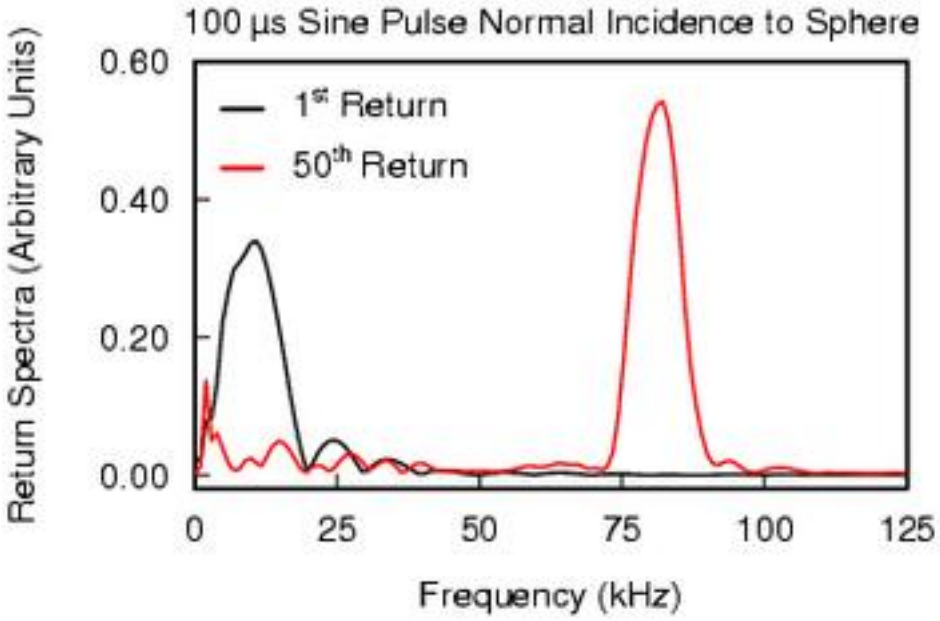

Figure 3.8: Fourier spectra of the results from the 10 cm sphere shown in Figs. 3.6 (first return) and 3.7 (fiftieth return). The TRO process detects the sphere as evident by the peak centered about 82.2 kHz.

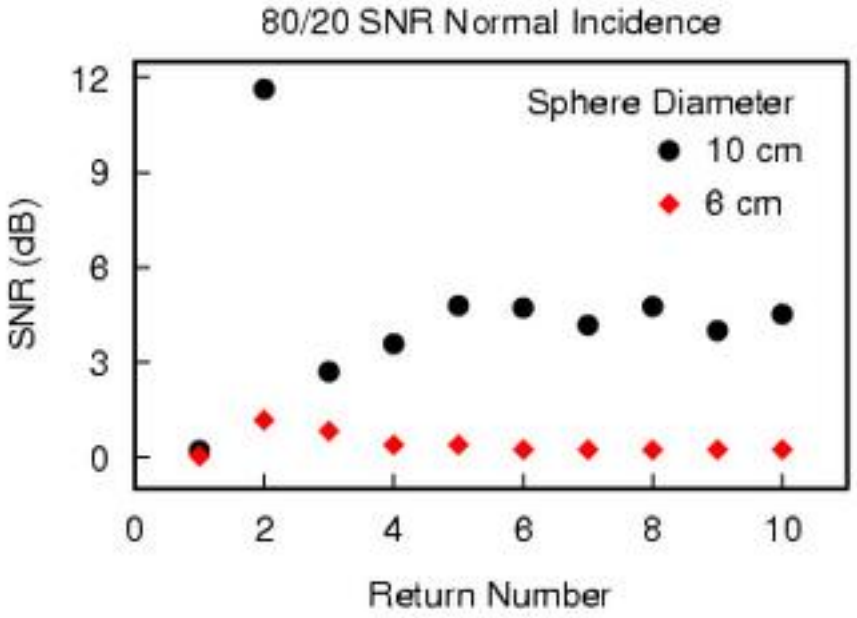

Figure 3.9: The SNR for the 10 μs one-cycle cosine pulse normally incident to the 6 (diamonds) and 10 cm (circles) spheres using Eq. (3.2). Both the spheres show similar behavior. There is an initial boost to the SNR of the 10 cm sphere after which the SNR then it converges to a smaller value.

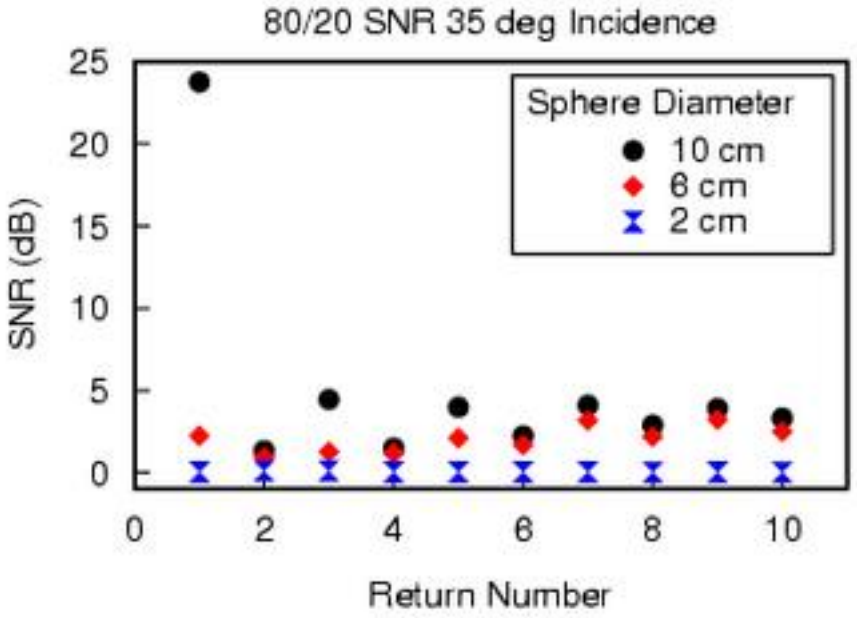

Figure 3.10: The SNR using Eq. (3.2) for the target off-axis from the source. Comparison with Fig. 3.9 shows that the time-reversal operator degrades the return from the target.

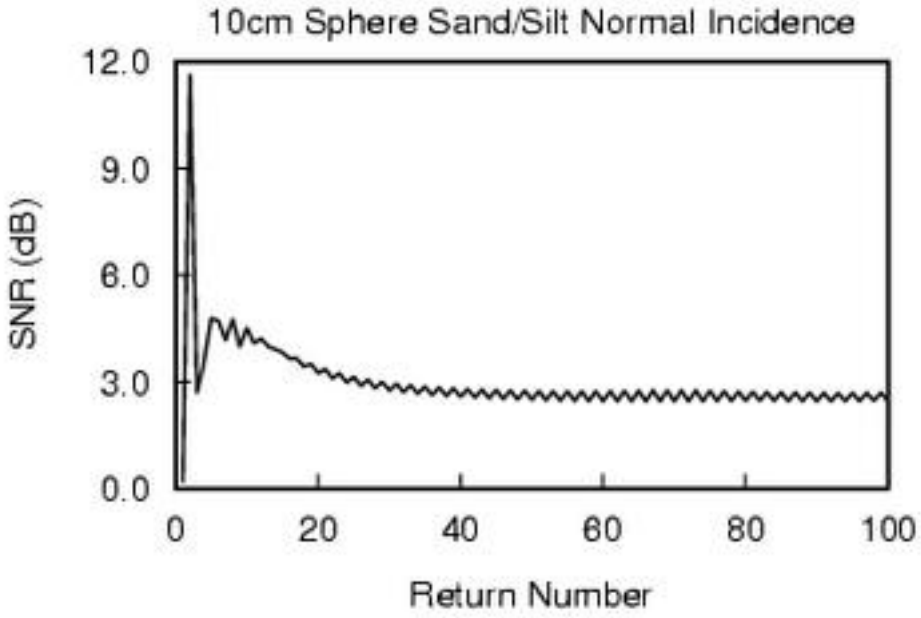

Figure 3.11: With the 10 cm sphere at normal incidence the SNR converges rapidly to approximately 1.14 dB and remains centered about that value for 1000 iterations of the wTRO. Only the first 100 returns are plotted.

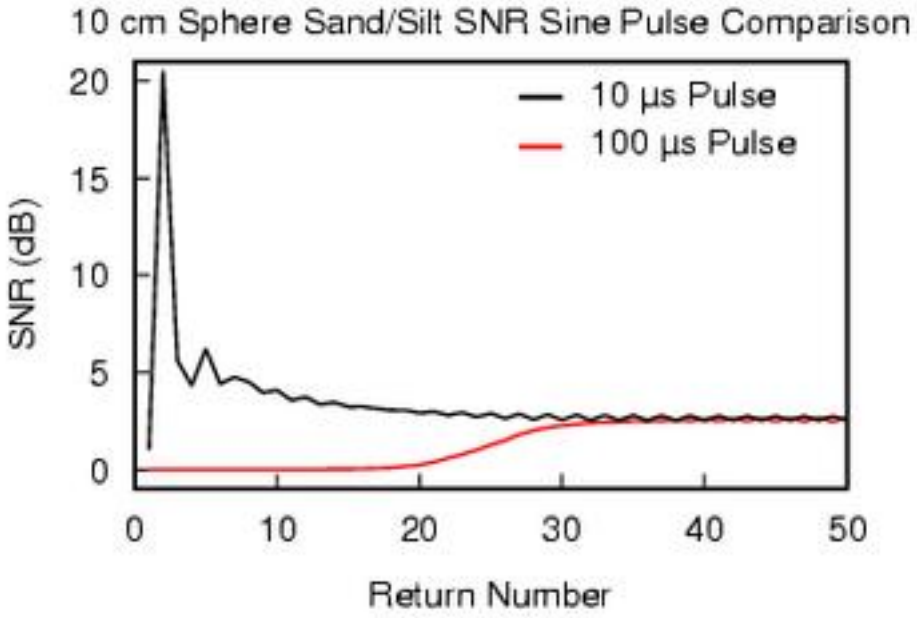

Figure 3.12: Convergence of the SNR of the 10 and 100 μs single-cycle sine pulses to the same value independent of the pulse length and shape as shown here is an important result that supports the idea that the TRO acts as a full-pass filter.

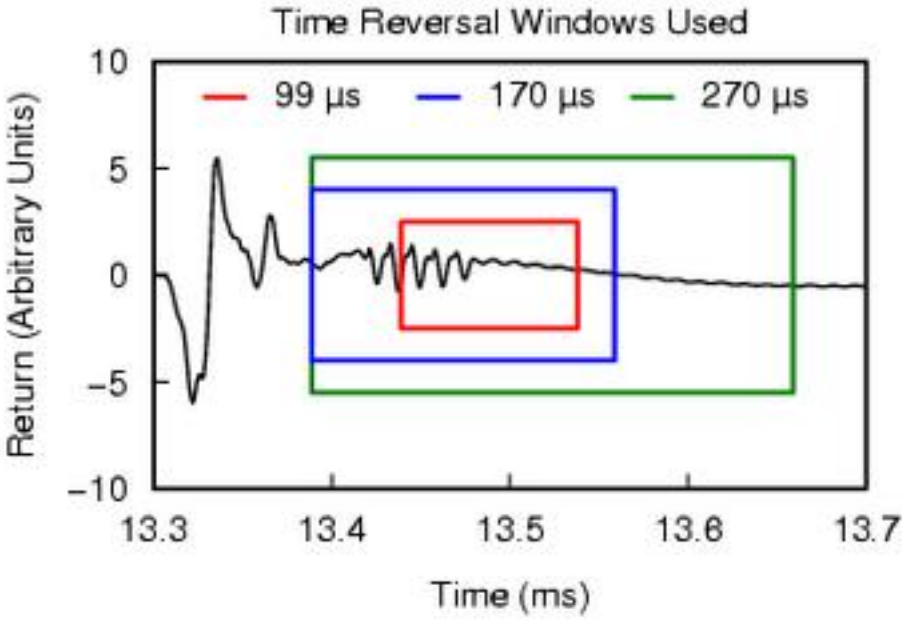

Figure 3.13: The three windows used for the time reversal operator on the 6 and 10 cm diameter targets. All windows enclose some of the return from the 10 cm diameter sphere at normal incidence.

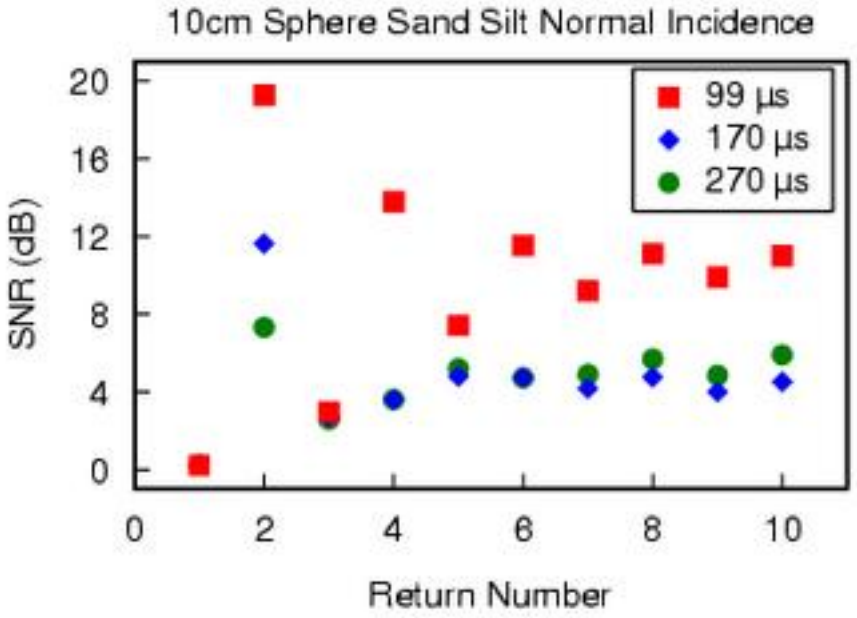

Figure 3.14: These SNRs show that no dependence on window duration, but a dependence on the start time.

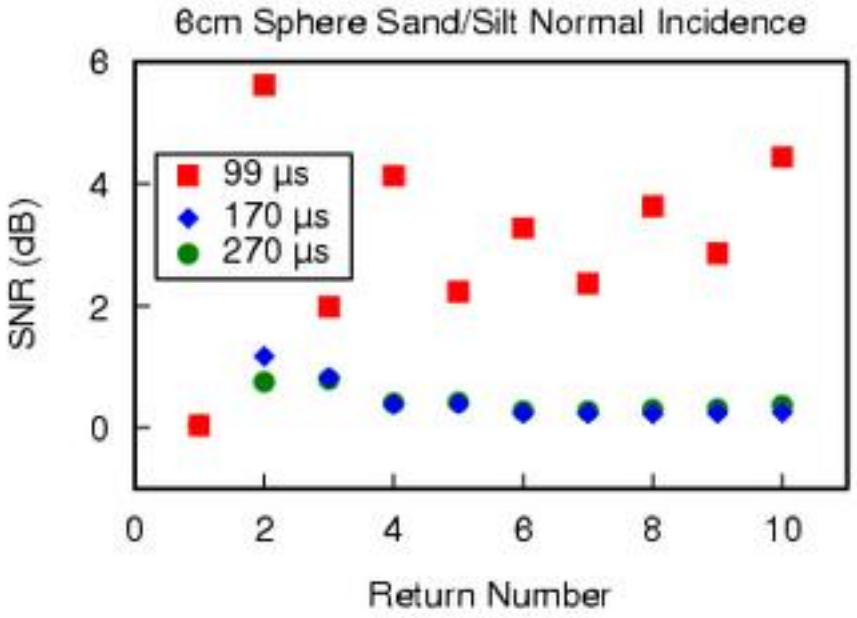

Figure 3.15: As Fig. 3.14 for the 6 cm sphere.

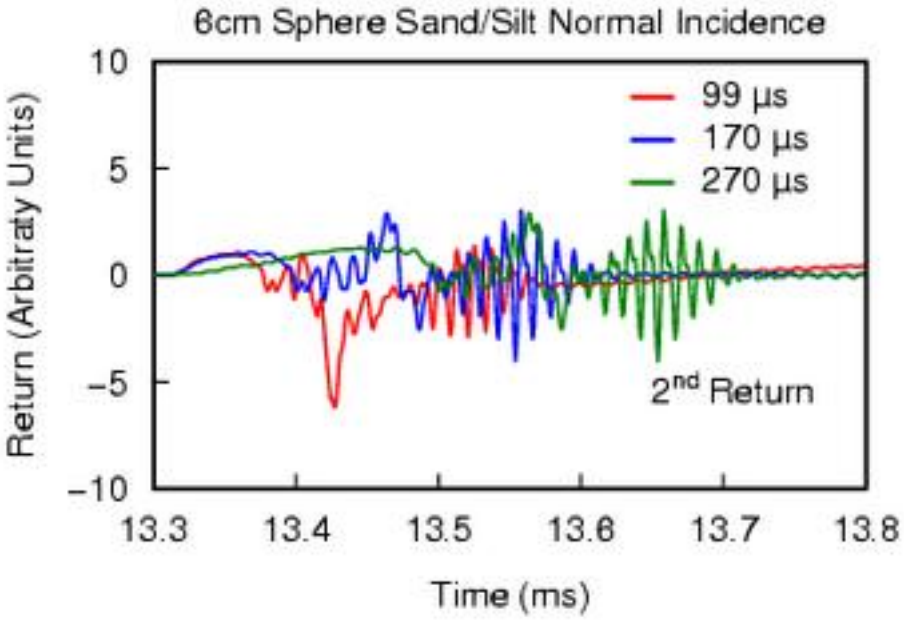

Figure 3.16: The time series for the return changes depending on when the wTRO starts and ends. The second return for the 6 cm sphere given here shows that the start time of the wTRO affects the waveform while the duration of the record affects the location of characteristics of the waveform.

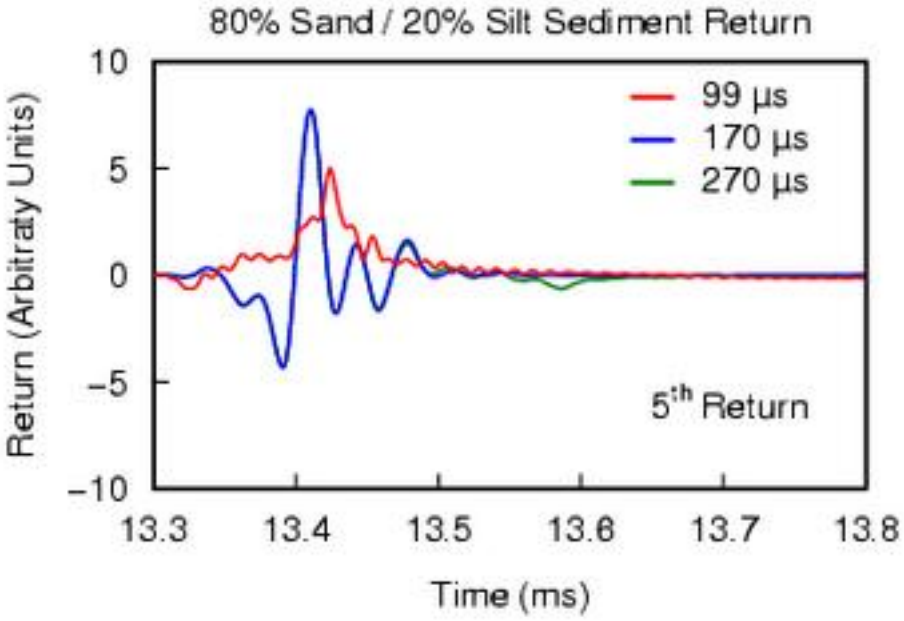

Figure 3.17: Sediment return for the various windows. The red line shows very little return from the sediment as compared to the other two lines. This is an artifact of both the start time and duration.

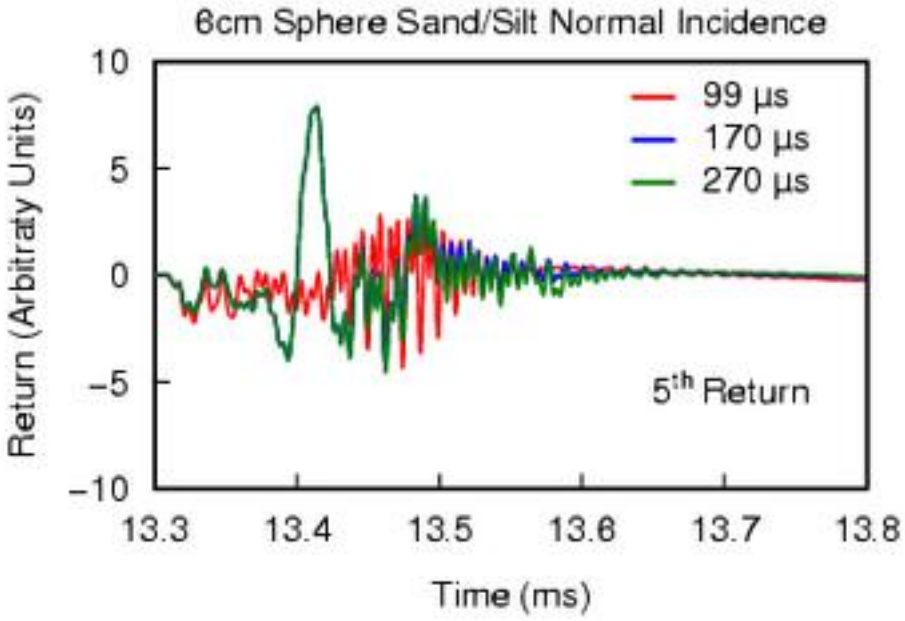

Figure 3.18: Comparing the returns for the 6 cm sphere (above) and the sediment (Fig. 3.17) shows that the amount of information about the sediment can be decreased by the proper choice of start time.

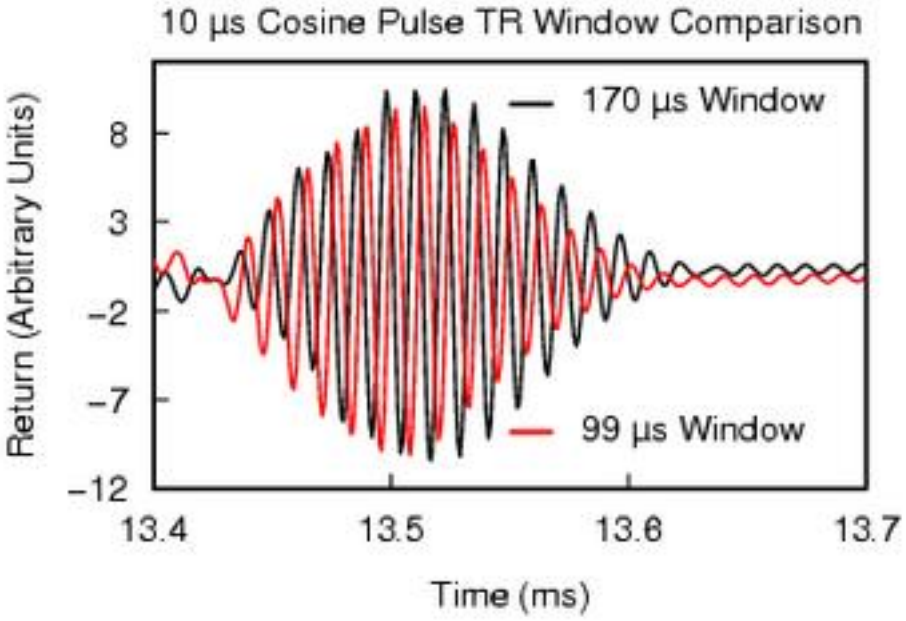

Figure 3.19: The TRO signal for the 10 cm diameter iron sphere converges to nearly identical waveforms after nine iterations for both windows, demonstrating the robustness of the TRO for different windows.

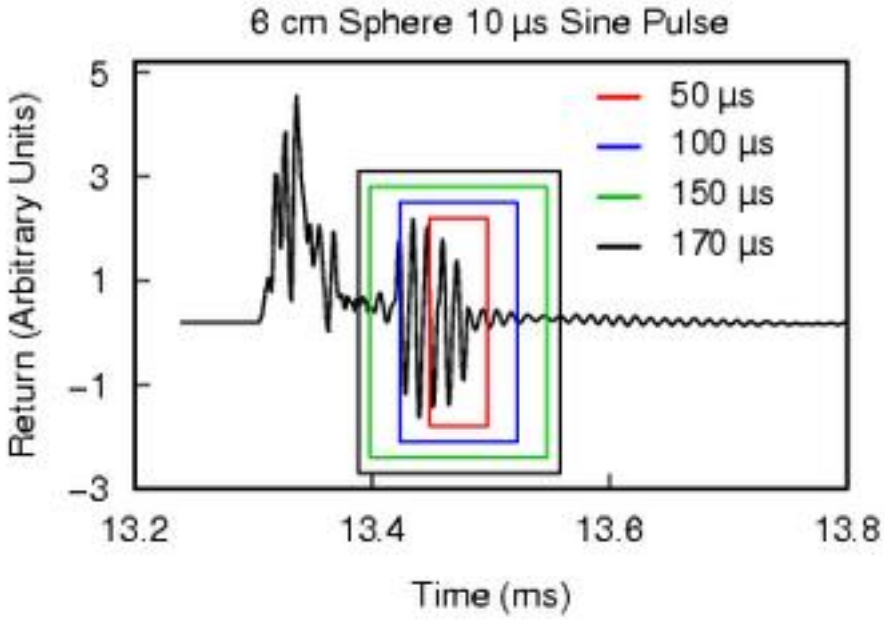

Figure 3.20: Time-reversal windows imposed on the first return from the 6 cm diameter iron sphere with the 10 μs single-cycle sine pulse at normal incidence. The windows are centered at the same time point in the return.

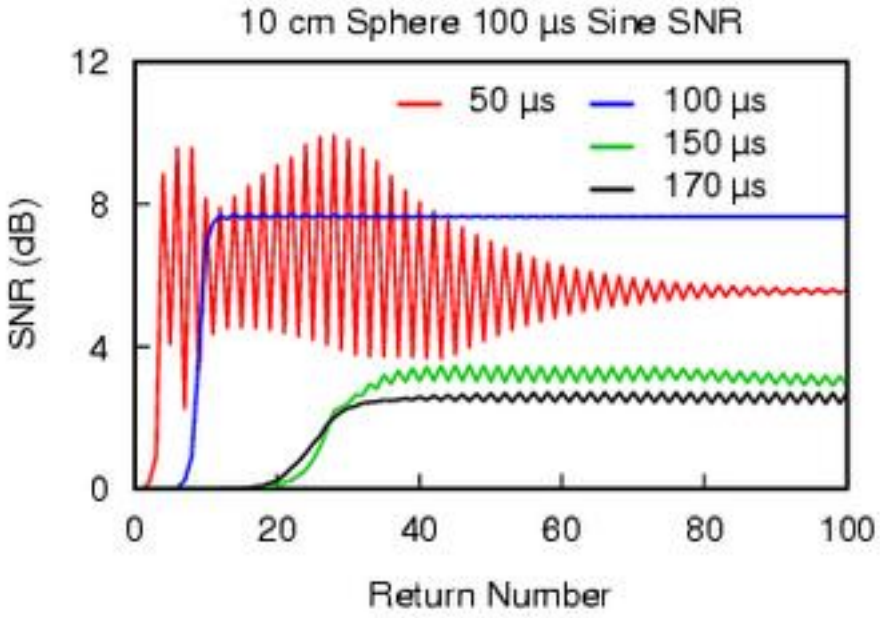

Figure 3.21: Different windows affect the signal-to-noise ratio in ways that are surprising. There exists an optimal window giving the best SNR depending on target dimension and initial pulse duration. This behavior is independent of gain or initial pulse amplitude. This figure uses the 10 cm diameter iron sphere in the sand/silt sediment with a 100 μs single-cycle sine.

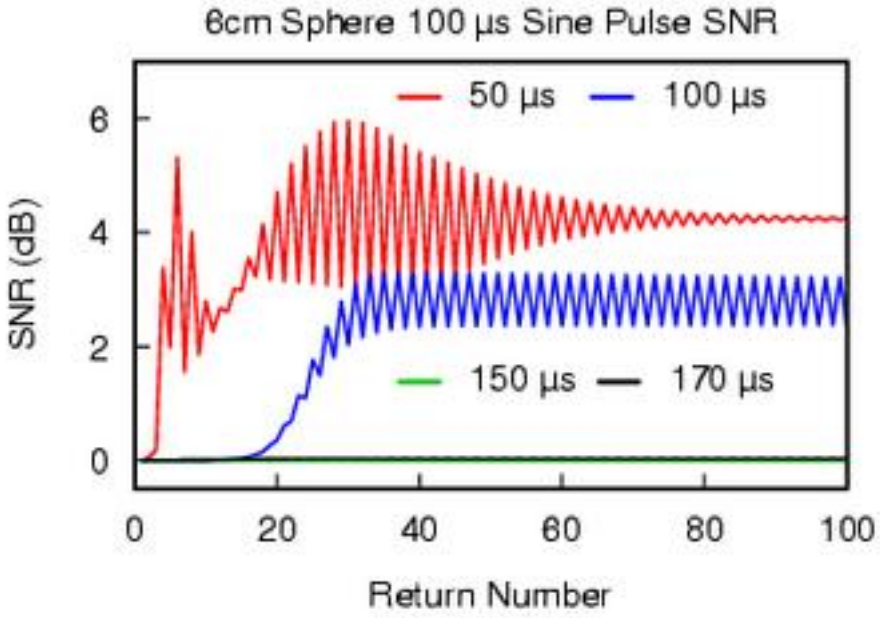

Figure 3.22: As Fig. 3.21 for the 6 cm sphere. We expect no return. However, the time-reversal operator can be tuned to enhance the signal from the sphere and increase the SNR. The smaller windows detects the sphere while the longer windows do not since the longer windows include more sediment return.

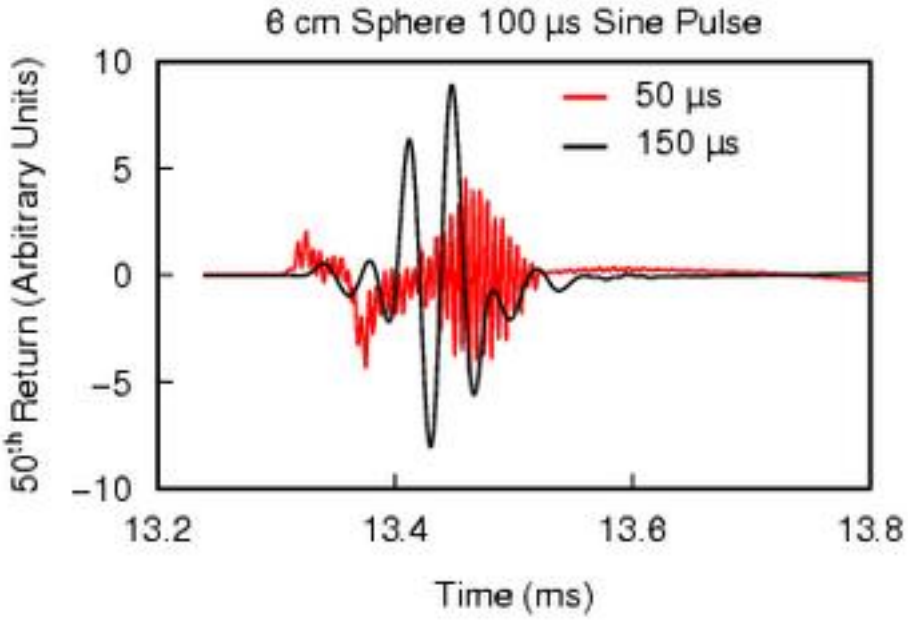

Figure 3.23: Using the 100 μs single-cycle sine pulse normally incident on the 6cm diameter iron sphere we can see that the fiftieth return from the 50 μs TRW detects the sphere while the 150 μs TRW just detects the sediment. So setting the center and durations of the TRW are the important factors in target detection using initial pulses with wavelengths greater than the dimension of the target.

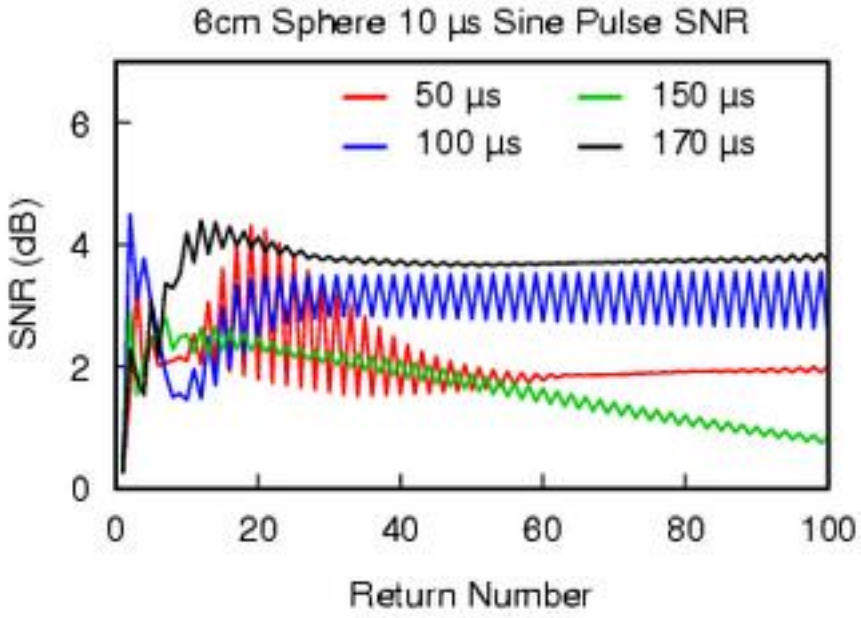

Figure 3.24: SNRs for a 10 μs single-cycle sine pulse normally incident on the 6cm diameter iron sphere. All TRWs allow the sphere to be detected. The longer the TRW the higher the SNR, except for the 150 μs TRW, which appears to be an anomaly. This could be an artifact of phase matching between the sediment-only return and the target-sediment returns.

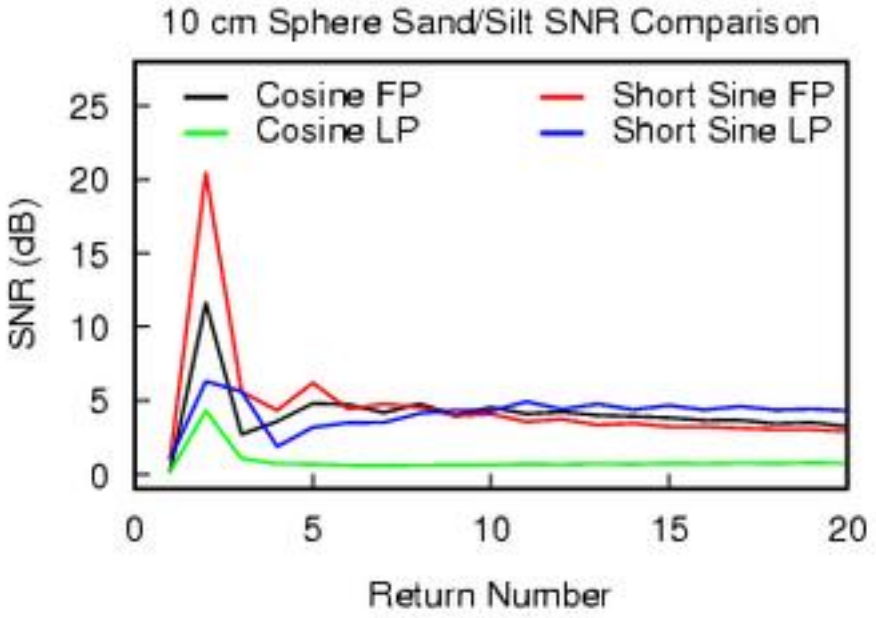

Figure 3.25: SNRs for the one-cycle cosine pulse of 10 μs duration and the corresponding sine pulses of the same duration. The black line is the SNR for the 10 cm diameter sphere from the cosine pulse using a full pass (FP) filter, the red is the same for the sine pulse, and the green and blue lines are from the low pass (LP) filter on the returns from the cosine pulse (green) and the sine pulse (blue).

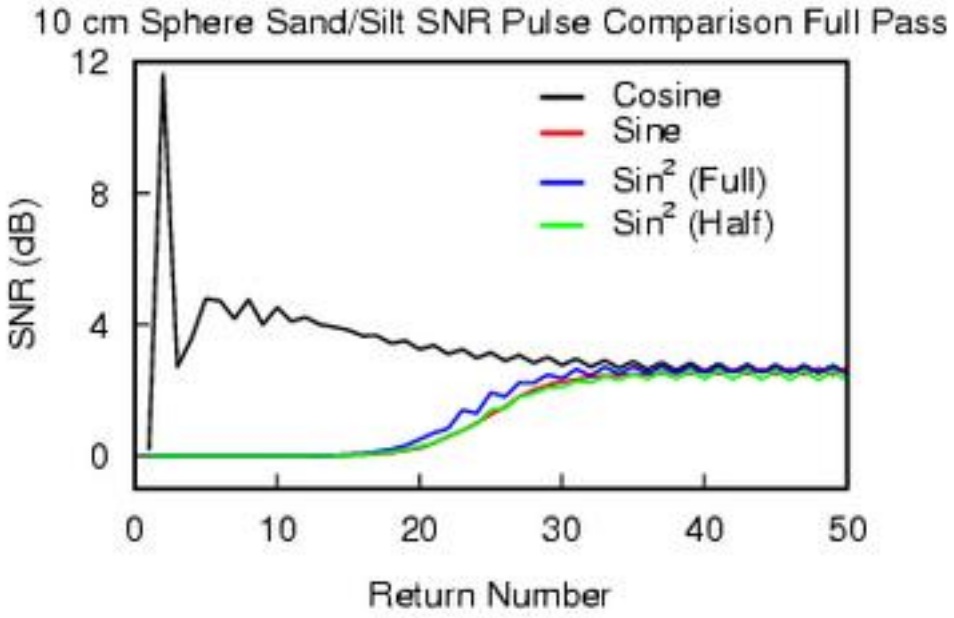

Figure 3.26: Except for the 10 μs sine, all pulses incident on the 10 cm diameter sphere whose closest surface is 10.1 m away from the source converge to the same SNR after approximately 35 iterations. The black line is for the 10 μs one-cycle cosine pulse, red for the 100 μs one-cycle sine pulse, blue for the 100 μs one-cycle squared-sine pulse, and the green for the 50 μs two-cycle squared-sine pulse.

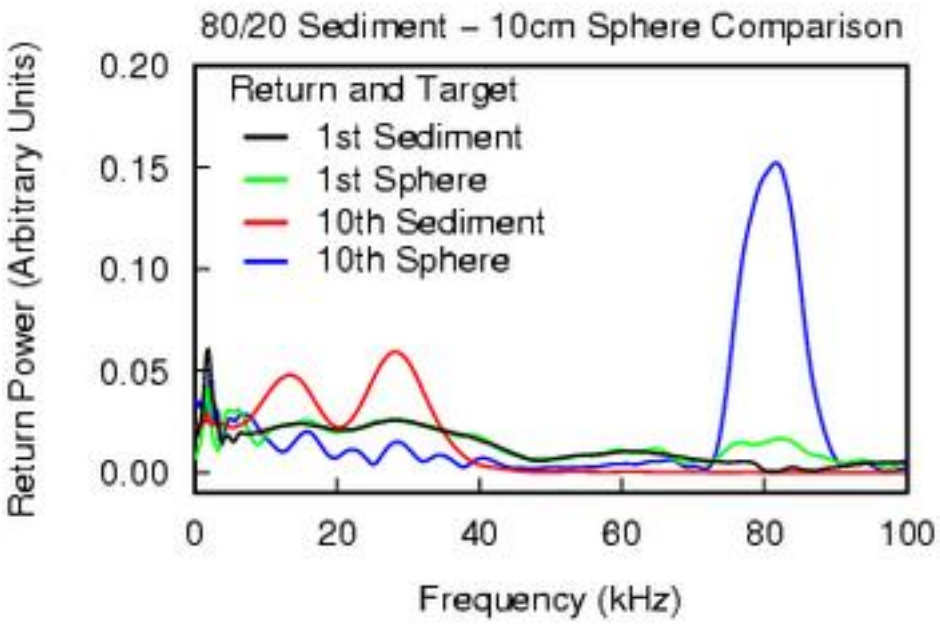

Figure 3.27: Frequency spectrum of the returns with and without the 10 cm diameter sphere. The spectra depend not only on iteration, but also on the target.

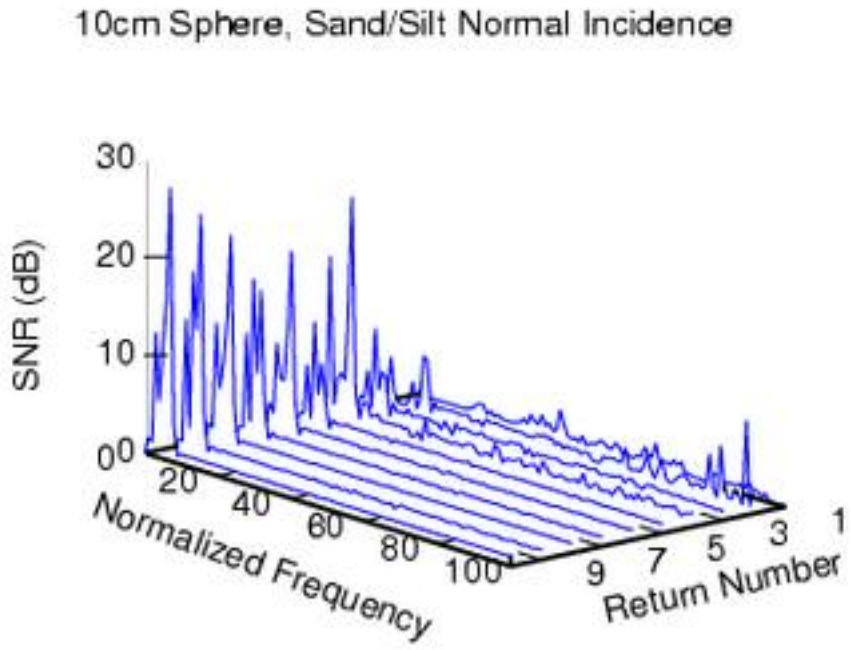

Figure 3.28: The frequency dependence of the SNR provides more information about the target for the second and higher returns. The higher frequencies are suppressed for the sixth and higher returns. The sphere information is contained in the lower frequencies. The frequency interval for the above is 5 kHz.

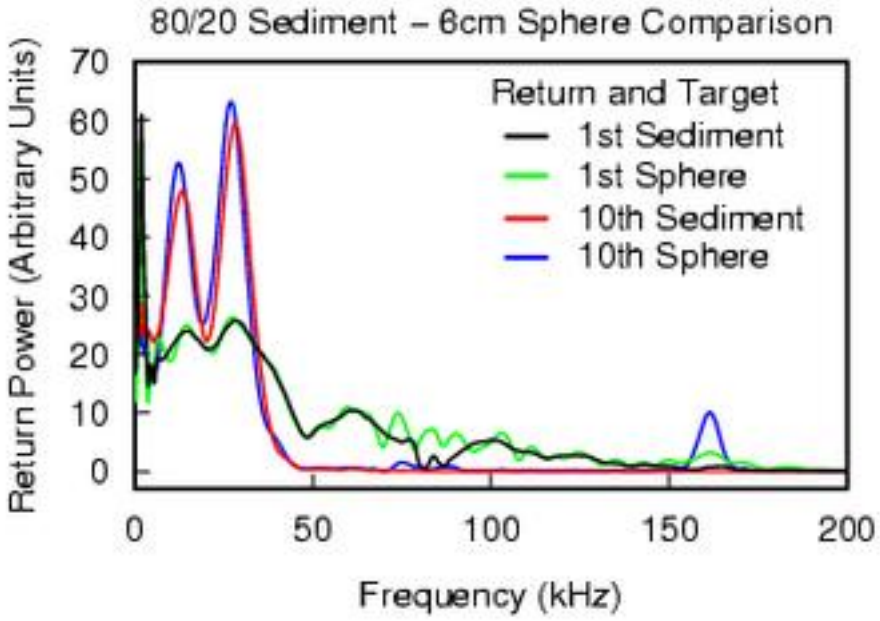

Figure 3.29: As Fig. 3.27, but for the 6 cm sphere.

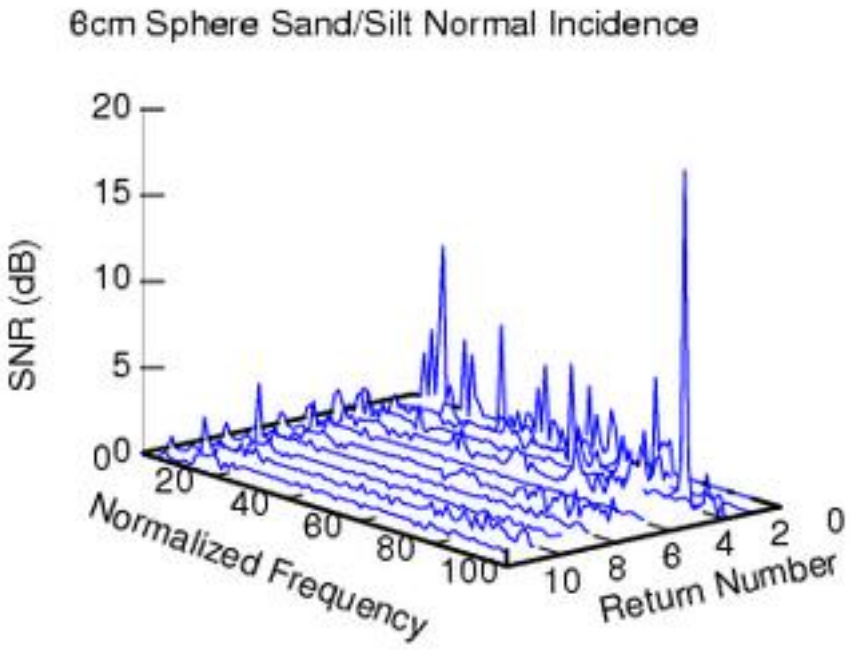

Figure 3.30: As Fig. 3.28, but for the 6 cm sphere. Most information is contained in the third and fourth return.

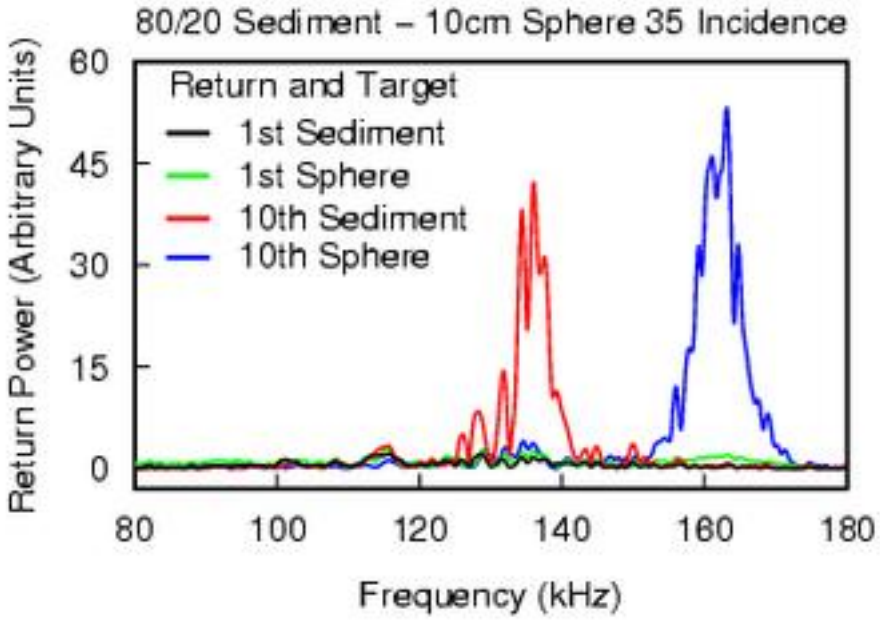

Figure 3.31: A comparison of the power spectra with and without the sphere for non-normal-incidence returns. There is a shift in frequency as compared with normal incidence. The red line is the tenth return without a sphere, blue is with the sphere.

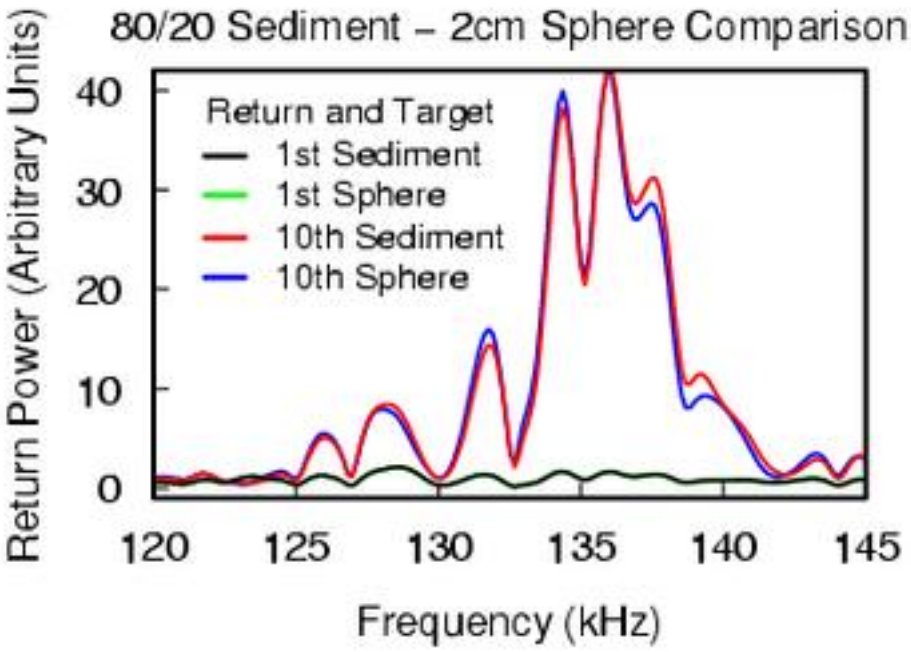

Figure 3.32: As Fig. 3.31, but for the 2 cm sphere. The 2 cm sphere behaves as a small perturbation in the sediment.

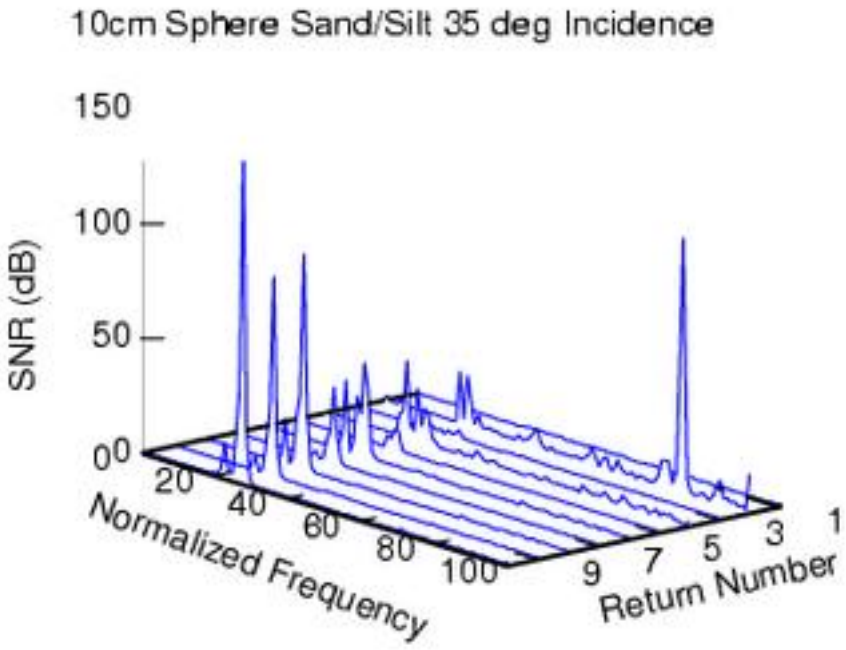

Figure 3.33: SNR for off-axis detection, 10 cm sphere.

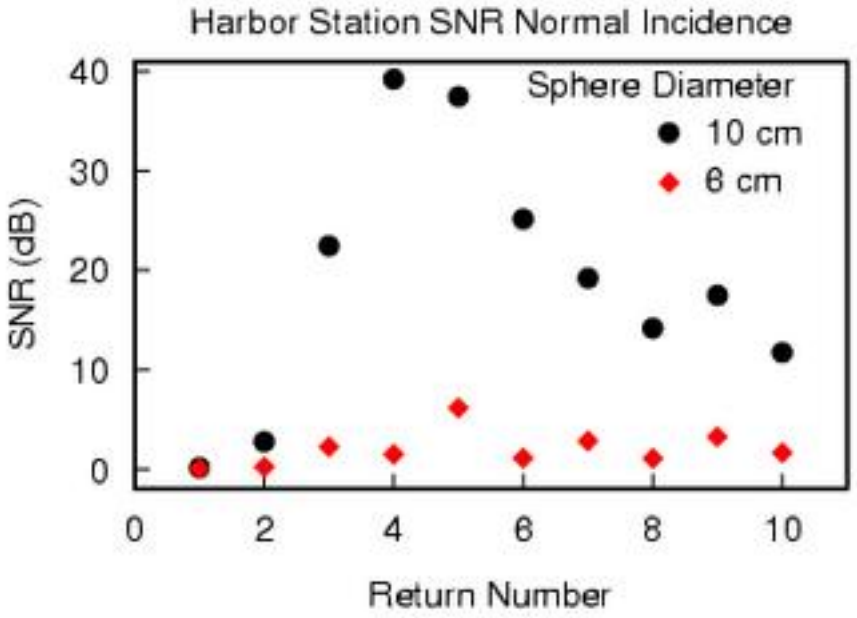

Figure 3.34: SNR for returns from the Harbor Station sediment for normal incidence. The 6 cm sphere shows similar behavior to that of the 80/20 sand/silt. The 10 cm sphere shows that the SNR improves with iteration.

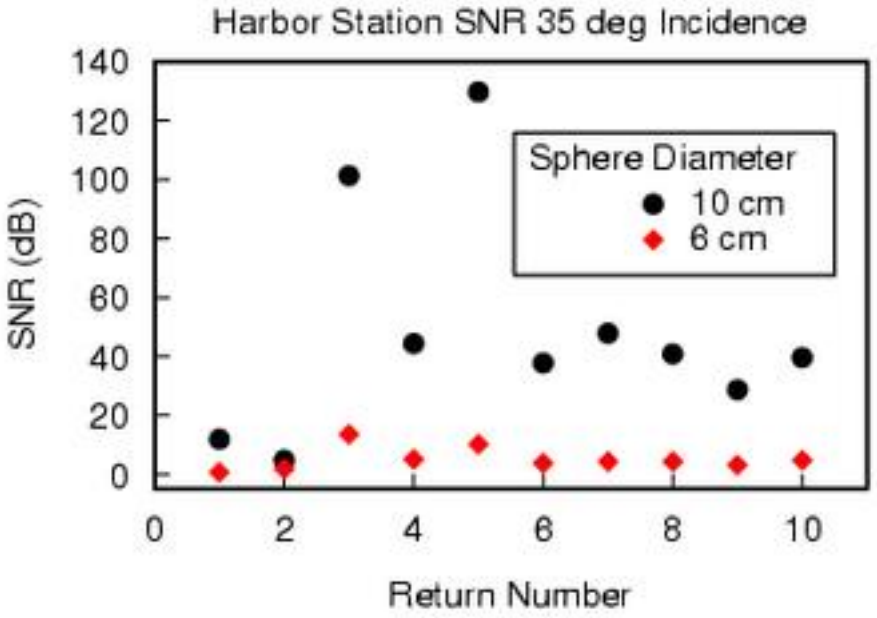

Figure 3.35: As Fig. 3.34, but for non-normal incidence.

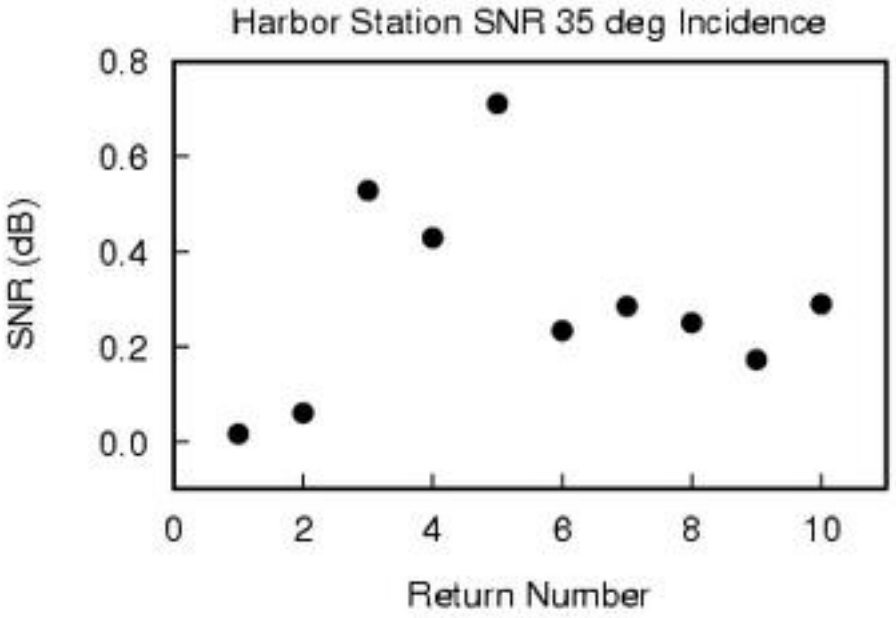

Figure 3.36: As Fig. 3.35, but for the 2 cm sphere. The 2 cm sphere is detected.

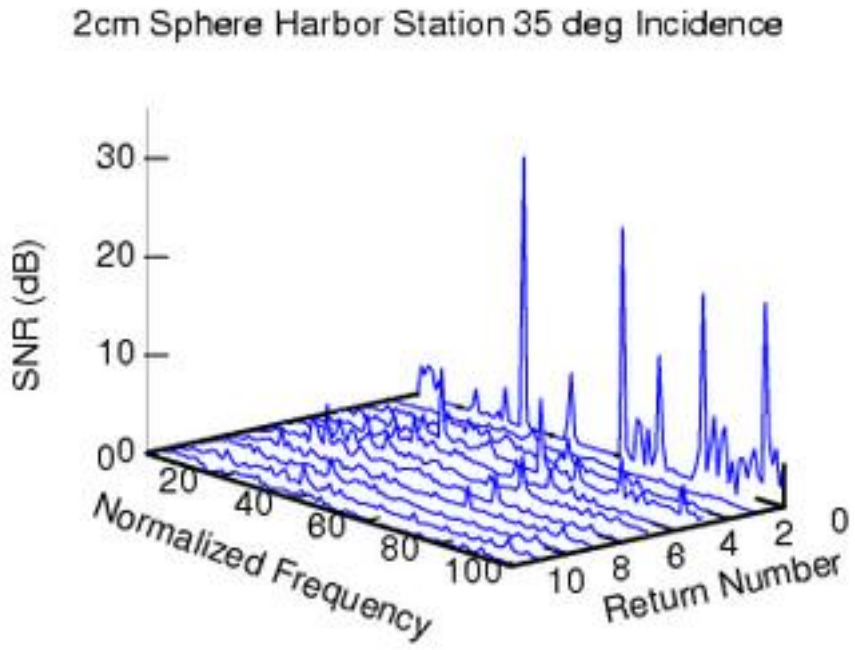

Figure 3.37: The SNR from the 2 cm sphere in the Harbor Station sediment at 35° incidence.

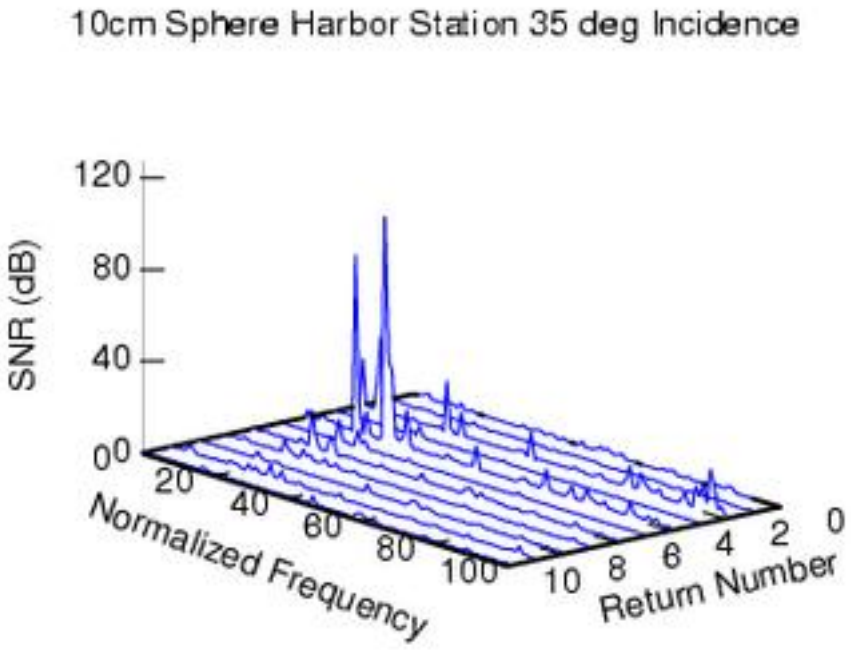

Figure 3.38: As Fig. 3.37, but for the 10 cm sphere.

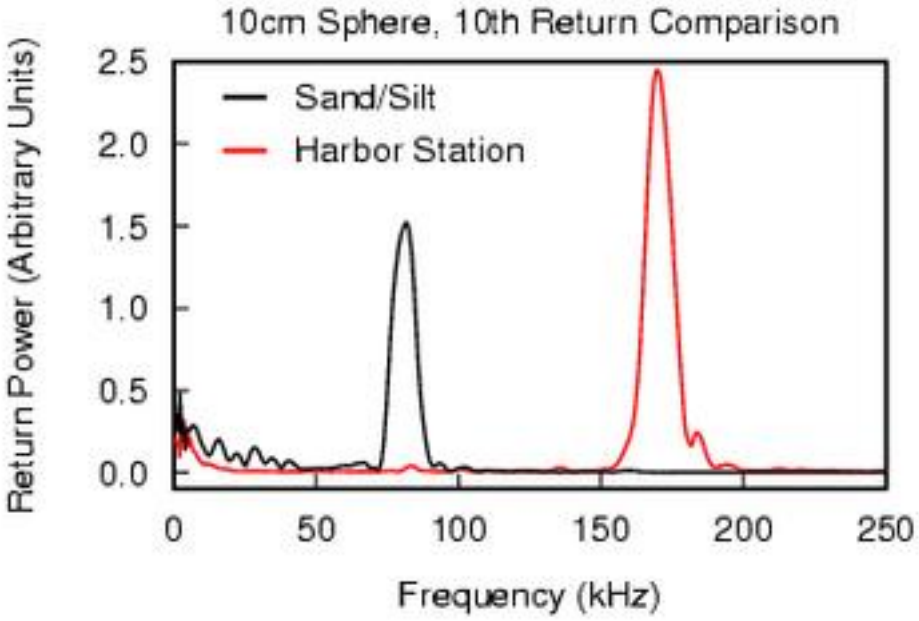

Figure 3.39: The power spectrum of tenth return from the 10 cm sphere in normal incidence using the 10 μs single-cycle cosine pulse for Harbor Station sediment (red line) and the 80% sand / 20% silt sediment (black line). The peak is from the sphere while the shifts of the peaks are from the acoustical properties of the sediment.

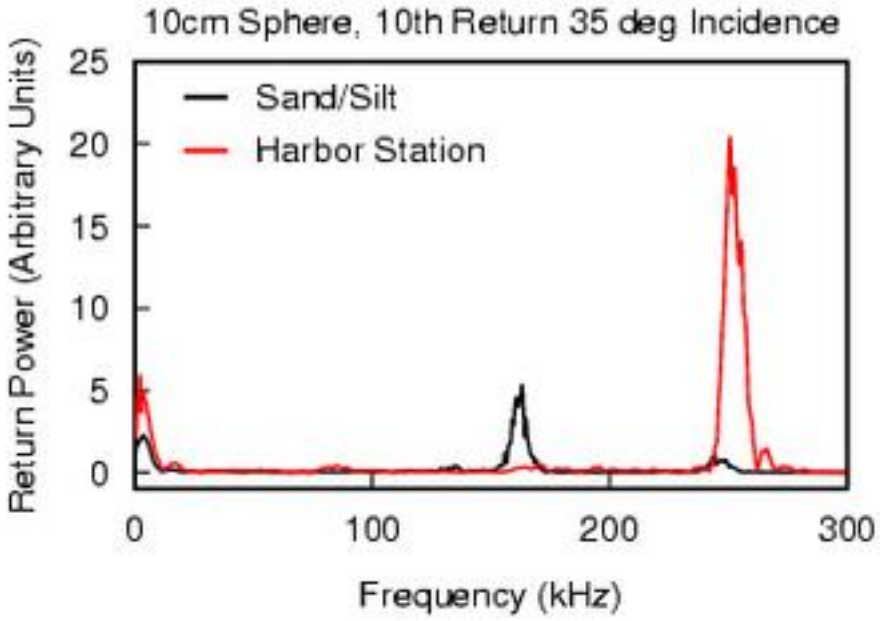

Figure 3.40: As Fig. 3.39, but for 35° incidence.

Table 3.1: Properties of the constituents of the different sediments. The percentages of each in the Harbor Station sediment are also given [38], [5], [41].

Type	%	ρ	c (m/s)	α(dB/λ)
Sand	71.23%	1.9	1650	0.8
Gravel	25.82%	2.0	1800	0.6
Clay	2.53%	1.5	1500	0.2
Silt	0.42%	1.7	1575	1.0

Table 3.2: Comparison of the three parameters that have the greatest affect on the backscattered returns [38], [5], [41].

Parameter	Sand-Silt	Harbor Station
Sound Speed (m/s)	1635	1685
Density ($\times\rho_{H_2O}$)	1.86	1.92
Attenuation (dB/λ)	0.84	0.74

Chapter 4

Conclusion and Closing

4.1 Concluding Remarks

Time reversal operating on the backscattered return does not behave in the same way as time-reversal does on forward scattered signals as I have shown by deriving Eq. (2.68) and through the simulations I have performed. I have shown that time-reversal can effectively detect and obtain target information using a single point transceiver. By performing time-reversal on a window of the return the backscattered signal will converge to a waveform consistent with the Fourier-Bessel impulse response from the target as in Fig. 3.4. Figure 3.4 shows the first return from a 10 cm diameter iron sphere buried in the 80% sand / 20% silt sediment where the surface of the sphere is 10 cm from the surface of the seafloor. The red line is the first return using a single-cycle sine wave 10 μs in duration and the black line is the first return using a single-cycle sine wave 100 μs in duration. Both responses are recorded by the point transceiver located 10 m above the seafloor at normal incidence. After forty-nine iterations of the time-reversal operator (TRO), the fiftieth return will have the shape as those in Fig. 3.5. Again the red line is the response using the single-cycle 10 μs sine pulse and the black is the response using the 100 μs single-cycle sine pulse. What is important to notice is that both waveforms are nearly identical and both contain the Fourier-Bessel components consistent with scattering from a sphere. In contrast

to Fig. 3.4, Fig. 3.5 shows that the 10 cm diameter iron sphere is detected using the 100 μs one-cycle sine pulse. This is a striking result since the 100 μs pulse has a spatial resolution of 0.16 m assuming a median sound speed of 1600 m/s. The target sphere has a diameter of 0.1 so any backscattered response from the sphere will be negligible.

The reason time-reversal is able to detect this sphere is rather simple. The time-reversal operator uses the complete return sampled over the recording phase of the operation with a sharp cutoff in the time domain. This generates high frequency components, which enter the next probing signal and increase the resolution. In this respect the time-reversal operator acts as a full-pass filter that changes the temporal order of the received signal. The limiting factor of this procedure is the sampling rate for the transceiver, which I have set to 1 MHz (1 μs) for all simulations studied here. It has been shown in other work that the TRO converges to a waveform such that the energy focuses to the acoustically hardest scatterer and does so by converging to the Green's function of the environment that has the shortest path between the source and scatterer, [29], [30]. That is evidenced by the wave packet in Fig. 3.5 which remains in approximately the same temporal location with small oscillations about a median position due to the iterative TRO itself, recall the discussion following Eq. (2.100).

Since I have complete control over the environment in these simulations, I can perform the iterative TRO on the the seabed with and without the target sphere present. Taking advantage of this I define a signal-to-noise ratio (SNR) as

$$SNR = \frac{\int_T (S(t) - N(t))^2 dt}{int_T N^2(t) dt} \tag{4.1}$$

where S is the return with the sphere present, N is the return of the sediment only, T is the time duration of the TRO window. This definition of the SNR states that the backscatter from the sphere is the signal of interest while all other components of the recorded signal are noise. Using the above definition for the SNR on the returns that give Fig. 3.4 and Fig. 3.5 results in the plots of Fig. 3.12, where I calculate the SNR for

each iteration of the TRO. The black line is the SNR from the 10 μs single-cycle sine pulse and the red is from the 100 μs single-cycle sine pulse. Notice that both curves converge to the same SNR values as the number of iterations of the TRO increases. Consistent with the previous paragraph, this convergence is independent of the initial pulse shape used and only depends on the strength of the reflected signal. At low iteration numbers, there is a significant difference in the SNR from the two pulses used, which is an artifact of the difference in the frequencies of the initial pulses.

Calculation of the temporal spectrum of the returns confirm the presence of a sphere. The backscattered responses in Fig. 3.4 and Fig. 3.5 give spectra as in Fig. 3.8 where I have plotted the spectra of the first return, solid black line, and the fiftieth return, solid red line, using the 100 μs single-cycle sine pulse normally incident on the sphere. Recall the wave packets in Fig. 3.5 due to the sphere, they contribute the peak at 82.2 kHz in the spectrum while the peak 28.4 kHz is due to the sediment only. The peak at 82.2 kHz from the sphere using the iterative TRO for the 100 μs single-cycle sine pulse is not the result of super-resolution through the inhomogeneous sediment, but is due to the full-pass filtering property of the TRO. If this peak in the spectra was removed after each iteration, the response from the sphere would be diminished as is shown in Fig. 3.25 where I plot the SNR using Eq. (3.2) for the 10 μs single-cycle cosine and sine pulses normally incident on the 10 cm diameter sphere. In this figure, the low-pass filter used was a cosine fall-off starting at 4.9 kHz and ending at 17.6 kHz removing all frequencies higher than 17.6 kHz. Super-resolution may provide some small assistance to the initial detection of the sphere if the return is small as in Fig. 3.6 where the black line is the first return from the sediment only and the red line is the first return from the 10 cm diameter sphere using the 100 μs single-cycle sine pulse normally incident to the seafloor in both cases. The small difference in the returns may be the result of super-resolution, but is unlikely since the median size of an inhomogeneity in the sediment is on the order of the sphere. After forty-nine iterations of the TRO, shown in Fig. 3.7, shows that the 10 cm diameter iron sphere is detected by the red line and looks nothing like the return from the

sediment without the sphere represented by the black line.

Another interesting behavior from the iterative TRO is shown in Fig. 3.39 where I compare the tenth return from the 10 cm diameter sphere using a single-cycle 10 μs cosine pulse normally incident to the target while using two different sediment types. The black line represents the return using the 80 % sand / 20% silt sediment and the red line is from the Harbor Station sediment model. Since I used the same geometry and time-reversal window for both series, the shifts in frequency between the two peaks come from the properties of the sediments. This is substantiated by Fig. 3.19 where I plot the tenth return from the single-cycle cosine pulse normally incident to the 10 cm sphere for the 80 % sand / 20% silt sediment using the 99 μs time-reversal window (TRW), the solid black line, and the 170 μs TRW, solid red line. The TRW has little affect on the response from the sphere, as long as the sphere response is in the window to some extent the iterative TRO will give consistent results independent of the window start time and duration. The major contributing factor to the frequency shifts is due to the acoustical properties of the sediment.

All the conclusions discussed leave two important questions. One is "What is the time-reversal of a signal?", and the other is "What good is it and what advantages does it have over other signal processing techniques?" Time-reversal can be thought of as a full-pass filter that acts along acoustical ray paths. This idea is consistent with the evidence I present and with other experiments and theories, [19], [29], [12], [17]. For backscattered signals, time-reversal provides a method to obtain target information that may not be easily discernible for the background. Time-reversal does not require any inversion or matched-field processing techniques thus eliminating the need for environmental information or computationally complex calculations that may be solved after the environment has changed. It also provides a method to use sonar systems for purposes other than those for which they were originally designed. Side-scan sonar systems that are traditionally used to generate high resolution images of the seafloor can be used to locate buried targets with minor changes made to the control software.

What is the future of time-reversal in acoustics and this work in particular? Even though time-reversal has been studied for several years in academia, it was thought of as a "solution looking for a problem" or as an interesting experiment to demonstrate the properties of systems and a physical demonstration of Green's functions. Now it can be thought of as a tool that can provide information about targets independent of the structure or properties of the propagating environment as long as that propagating environment is static relative to the time of signal propagation.

List of References

[1] J. S. Jaffe, K. D. Moore, D. Zawada, B. L. Ochoa, and E. Zege. Underwater optical imaging: New hardware and software. *Sea Tech.*, 39(7):70–74, July 1998.

[2] K. D. Moore, J. S. Jaffe, and B. L. Ochoa. Development of a new underwater bathymetric laser imaging system: L-bath. *J. Atmos. Ocean. Tech.*, 17(8):1106–1117, August 2000.

[3] K. D. Moore and J. S. Jaffe. Time-evolution of high-resolution topographic measurements of the sea floor using a 3-d laser line scan mapping system. *IEEE J. Oceanic Eng.*, 27(3):525–545, July 2002.

[4] I. Tolstoy and C. S. Clay. *Ocean Acoustics: Theory and Experiment in Underwater Sound*. AIP for ASA, New York, NY, 1987.

[5] F. B. Jensen, W. A. Kuperman, M. B. Porter, and H. Schmidt. *Computational Ocean Acoustics*. Springer-Verlag for AIP Press, New York, NY, 2000.

[6] S. Griffin, J. Bradley, M. Thiele, C. Tran, F. Grosz, and M. Richardson. An improved subsequent burial instrumented mine. In *Proceedings of Oceans '02 MTS/IEEE*, volume 1, pages 72–77. MTS/IEEE, IEEE, October 2002.

[7] Director Expeditionary Warfare, editor. *U. S. Navy Mine Warfare Plan*, Washington, D. C., February 1994. Office of the Chief of Naval Operations. Fiscal Year 1994-1995 Programs.

[8] Ocean Studies Board National Research Council. *Oceanography and Mine Warfare*. National Academy Press, Washington, D. C., 2000.

[9] R. C. Spindel. Oceanographics and navigational instruments. In M. J. Crocker, editor, *Handbook of Acoustics*, chapter 38, pages 457–465. John Wiley and Sons, New York, N. Y., 1998.

[10] E. I. Thorsos, K. L. Williams, N. P. Chotiros, J. T. Christoff, K. W. Commander, C. F. Greenlaw, D. V. Holliday, D. R. Jackson, J. L. Lopes, D. E. McGehee, J. E. Piper, M. D. Richardson, and D. Tang. An overview of sax99: Acoustic measurements. *IEEE J. Oceanic Eng.*, 26(1):4–25, January 2001.

[11] M. Fink. Time-reversal mirrors. *J. Phys. D: Appl. Phys.*, 26(9):1333–1350, September 1993.

[12] M. Fink, D. Cassereau, A. Derode, C. Prada, P. Roux, M. Tanter, J.-L. Thomas, and F. Wu. Time-reversed acoustics. *Rep. Prog. Phys.*, 63(12):1933–1994, December 2000.

[13] W. S. Hodgkiss, H. C. Song, W. A. Kuperman, T. Akal, C. Ferla, and D. R. Jackson. A long-range and variable focus phase-conjugation experiment in shallow water. *J. Acoust. Soc. Am.*, 105(3):1597–1604, March 1999.

[14] H. C. Song, W. A. Kuperman, W. S. Hodgkiss, T. Akal, and C. Ferla. Iterative time reversal in the ocean. *J. Acoust. Soc. Am.*, 105(6):3176–3184, June 1999.

[15] K. B. Smith, A. A. M. Abrantes, and A. Larraza. Examination of time-reversal acoustics in shallow water and applications to noncoherent underwater communications. *J. Acoust. Soc. Am.*, 113(6):3095–3110, June 2003.

[16] M. Heinemann, A. Larraza, and K. B. Smith. Experimental studies of applications of time-reversal acoustics to noncoherent underwater communications. *J. Acoust. Soc. Am.*, 113(6):3111–3116, June 2003.

[17] S. K. Lehman and A. J. Devaney. Transmission mode time-reversal super-resolution imaging. *J. Acoust. Soc. Am.*, 113(5):2742–2753, May 2003.

[18] M. Fink and J. de Rosny. Time-reversed acoustics in random media and in chaotic cavities. *Nonlinearity*, 15(1):R1–R18, January 2002.

[19] L. Borcea, G. Papanicolaou, C. Tsogka, and J. Berryman. Imaging and time reversal in random media. *Inverse Problems*, 18(5):1247–1279, 2002.

[20] A. Derode, A. Tourin, and M. Fink. Limits of time-reversal focusing through multiple scattering: Long-range correlation. *J. Acoust. Soc. Am.*, 107(6):2987–2998, June 2000.

[21] S. R. Khosla and D. R. Dowling. Time-reversing array retrofocusing in noisy environments. *J. Acoust. Soc. Am.*, 109(2):538–546, Feburary 2001.

[22] M. R. Dungan and D. R. Dowling. Computed narrow-band time-reversing array retrofocusing in a dynamic shallow ocean. *J. Acoust. Soc. Am.*, 107(6):3101–3112, June 2000.

[23] M. R. Dungan and D. R. Dowling. Computed narrow-band azimuthal time-reversing array retrofocusing in shallow water. *J. Acoust. Soc. Am.*, 110(4):1931–1942, October 2001.

[24] D. R. Dowling D. R. Jackson. Phase conjugation in underwater acoustics. *J. Acoust. Soc. Am.*, 89(1):171–181, January 1991.

[25] D. M. Pepper. Nonlinear optical phase conjugation. In M. L. Stitch and M. Bass, editors, *Laser Handbook*, volume 4, pages 333–485. North-Holland Physics Publishing, New York, NY, 1985.

[26] D. Marx, M. Nelson, E. Chang, W. Gillespie, A. Putney, and K. Warman. An introduction to synthetic aperture sonar. In M. Amin, editor, *Proceedings of the*

Tenth IEEE Workshop on Statistical Signal and Array Processing, pages 717–721. IEEE, August 2000.

[27] C. Draeger and M. Fink. One-channel time-reversal in chaotic cavities: Theoretical limits. *J. Acoust. Soc. Am.*, 105(2):611–617, February 1999.

[28] D. H. Chambers and A. K. Gautesen. Time reversal for a single spherical scatterer. *J. Acoust. Soc. Am.*, 109(6):2616–2624, June 2001.

[29] D. H. Chambers. Analysis of the time-reversal operator for scatterers of finite size. *J. Acoust. Soc. Am.*, 112(2):411–419, August 2002.

[30] C. Prada. Detection and imaging in complex media with the dort method. In M. Fink, W. A. Kuperman, J. P. Montagner, and A. Tourin, editors, *Imaging of Complex Media with Acoustic and Seismic Waves*, volume 84 of *Topics in Applied Physics*, pages 107–133. Springer Verlag, New York, NY, April 2002.

[31] G. Canepa, O. Bergem, and E. Pouliquen. *The implementation of BORIS-3D: bottom response from inhomogeneities and surface.* SACLANTCEN, 1997.

[32] N. G. Pace E. Pouliquen, O. Bergem. Time-evolution modeling of seafloor scatter. i. concept. *J. Acoust. Soc. Am.*, 105(6):3136–3141, June 1999.

[33] O. Bergem, E. Pouliquen, G. Canepa, and N. G. Pace. Time-evolution modeling of seafloor scatter. ii. numerical and experimental evaluation. *J. Acoust. Soc. Am.*, 105(6):3142–3150, June 1999.

[34] A. L. Fetter and J. D. Walecka. *Theoretical Mechanics of Particles and Continua.* McGraw-Hill, New York, NY, 1980.

[35] A. D. Pierce. *Acoustics: An Introduction to Its Physical Principles and Applications.* McGraw-Hill, New York, NY, 1991.

[36] C. Feuillade and C. S. Clay. Anderson (1950) revisited. *J. Acoust. Soc. Am.*, 106(2):553–564, August 1999.

[37] N. A. Gumerov and F. Duraiswami. Computation of scattering from n spheres using multipole reexpansion. *J. Acoust. Soc. Am.*, 112(6):2688–2701, December 2002.

[38] G. M. Battisto and C. T. Friedrichs. Preliminary water column profile surveys and sediment grabs of a mixed-sediment moun cape fear, north carolina may 2001. report, January 2002. Report for Evans-Hamilton, Inc.

[39] P. M. Morse and K. U. Ingard. *Theoretical Acoustics*. Princeton University Press, Princeton, NJ, 1986.

[40] L. M. Brekhovskikh and Y. P. Lysanov. *Fundamentals of Ocean Acoustics*. Springer-Verlag, New York, NY, second edition, 1991.

[41] D. R. Lide, editor. *CRC Handbook of Chemistry and Physics*. CRC Press, New York, NY, 83rd edition, 2002.

[42] J. D. Jackson. *Classical Electrodynamics*. Wiley, New York, NY, 2 edition, 1975.

Appendix A

Derivation of the Linear Sound Equation

A.1 Equations of Fluid Dynamics

The linear acoustic equation can be derived from the conservation of mass and the equation of motion (Euler's equation) for a fluid. Consider a fluid with density ρ and velocity $\vec{v}$, the conservation of mass states for a given fixed volume the amount of fluid in equals the amount of fluid out. In mathematical formalism it is

$$\frac{\partial \rho}{\partial t} + \nabla \cdot (\rho \vec{v}) = 0 \tag{A.1}$$

where $\rho\vec{v}$ is the mass current. Euler's equation states that for a given volume of fluid that is moving, the sum of all the forces is equal to the time rate change of momentum of that fluid, which is Newton's second law for a fluid. If we neglect all body forces such as gravity and set pressure as the only surface force acting on the volume $\vec{f_S} = -p\hat{n}$, then the total force on the volume is given by

$$\rho \frac{\partial \vec{v}}{\partial t} + \rho(\vec{v} \cdot \nabla)\vec{v} = -\nabla p. \tag{A.2}$$

A.2 Linearization

There are several approaches to linearize Eqs. (A.1) and (A.2), a straightforward approach [34] is to set the variables of density, velocity and pressure to a median

value plus a perturbation

$$\rho = \rho_0 + \rho' \qquad \vec{v} = \vec{v}_0 + \vec{v}' \qquad p = p_0 + p'. \tag{A.3}$$

Substitution of the above into the conservation of mass, Eq. (A.1), gives

$$\frac{\partial(\rho_0 + \rho')}{\partial t} + \nabla \cdot ((\rho_0 + \rho')(\vec{v}_0 + \vec{v}')) = 0 \tag{A.4}$$

which reduces to

$$\frac{\partial \rho'}{\partial t} + (\nabla \rho') \cdot \vec{v}_0 + \rho_0(\nabla \vec{v}') = 0 \tag{A.5}$$

where only the first order perturbations were retained. Euler's equation, Eq. (A.2), becomes

$$(\rho_0 + \rho')\frac{\partial(\vec{v}_0 + \vec{v}')}{\partial t} + (\rho_0 + \rho')[(\vec{v}_0 + \vec{v}') \cdot \nabla](\vec{v}_0 + \vec{v}') = -\nabla(p = p_0 + p'). \tag{A.6}$$

Retaining only terms that are first order in perturbation, the above reduces to

$$\rho_0 \frac{\partial \vec{v}'}{\partial t} + \rho_0(\vec{v}_0 \cdot \nabla)\vec{v}' = -\nabla p'. \tag{A.7}$$

A further simplification can be made by setting the average fluid velocity to zero. To avoid confusion, the primes will be dropped from Eq. (A.5) and Eq. (A.7). This leaves for Eq. (A.5)

$$\frac{\partial \rho}{\partial t} + \rho_0(\nabla \cdot \vec{v}) = 0 \tag{A.8}$$

and Eq. (A.7)

$$\frac{\partial \vec{v}}{\partial t} = -\frac{1}{\rho_0}\nabla p. \tag{A.9}$$

The curl of equation A.9 is

$$\nabla \times \frac{\partial \vec{v}}{\partial t} = -\frac{1}{\rho_0}\nabla \times \nabla p \tag{A.10}$$

which implies that the fluid is irrotational. As a result the velocity is the gradient of a potential $\vec{v} = \nabla\psi$. Using this and defining the speed of sound from $p = c^2\rho$, we can

now derive the linear wave equation in terms of the velocity potential. This gives

$$\begin{aligned} \vec{v} &= \nabla\psi \\ p &= -\rho_0 \frac{\partial\psi}{\partial t} \\ \nabla^2\psi - \frac{1}{c^2}\frac{\partial^2\psi}{\partial t^2} &= 0 \end{aligned} \tag{A.11}$$

for the velocity, pressure and linear acoustic equation in terms of on scalar potential. It should be noted that there is no need to single out the velocity of the field, the above derivation would give the same equation if the displacement vector or pressure was used [35],[4]. In the case of the displacement vector, ψ would be the displacement potential and the linear acoustic equation would be written in terms of pressure. Also, this equation is for free space, a source could be incorporated by setting the homogeneous equation to a forcing term $f(\vec{r}, t)$ associated with the source.

Appendix B

Solutions

B.1 Separation of Variables

The linear acoustic equation is a Sturm-Liouville equation where the solutions are obtained by several methods. Separation of variables can be used to gain some insight into the relationship between the spatial and temporal parts of the solution. We can assume that the solution to Eq. (2.1) can be written as $\psi(\vec{r},t) = R(\vec{r})T(t)$, where $R(\vec{r})$ is the spatial component and $T(t)$ is the temporal component. Using this turns the linear acoustic equation to

$$\frac{\nabla^2 R(\vec{r})}{R(\vec{r})} - \frac{1}{c^2 T(t)}\frac{d^2T(t)}{dt^2} = 0. \tag{B.1}$$

Setting

$$\frac{1}{c^2 T(t)}\frac{d^2T(t)}{dt^2} = -\alpha^2 \tag{B.2}$$

we find the the temporal part of $\psi(\vec{r},t)$ is a harmonic function with the spatial part satisfying the equation

$$\nabla^2 R(\vec{r}) + \alpha^2 R(\vec{r}) = 0. \tag{B.3}$$

Solutions to Eq. (B.2) are of the form

$$T(t) = \sum_{\alpha=-\infty}^{\infty} A_\alpha e^{(i\alpha ct)} \tag{B.4}$$

Setting $\beta = \alpha c$, we now have a Fourier series of the form

$$T(t) = \sum_{\beta=-\infty}^{\infty} A_\beta e^{(i\beta t)}. \tag{B.5}$$

So now we can find the coefficients A_β as

$$A_\beta = \int_{-\infty}^{\infty} T(t) e^{-i\beta t} dt. \tag{B.6}$$

What makes this interesting is the fact that as long as the temporal and spatial components are separable, the temporal solution to Eq. (2.1) can be expressed as a Fourier series of the type (B.5) allowing us to write the general solution to Eq. (2.1) as

$$\psi(\vec{r}, t) = \sum_{\alpha=-\infty}^{\infty} A_\alpha R(\vec{r}) e^{(i\alpha c t)}. \tag{B.7}$$

B.1.1 Approach to a Solution: Green's Function

As stated earlier, Eq. (2.1) can have an external forcing term $f(\vec{r}, t)$ included to make it more general resulting in an equation of the form

$$\nabla^2 \psi - \frac{1}{c^2} \frac{\partial^2 \psi}{\partial t^2} = -f(\vec{r}, t). \tag{B.8}$$

Green's theorem states that the solution to (B.8) can be obtained through a second function $G(\vec{r}, t; \vec{r}\,', t\,')$ which must satisfy the following conditions:

1. $G(\vec{r}, t; \vec{r}\,', t\,')$ must be a solution to the following inhomogeneous linear acoustic equation.

$$\nabla'^2 G(\vec{r}, t; \vec{r}\,', t\,') - \frac{1}{c^2} \frac{\partial^2 G(\vec{r}, t; \vec{r}\,', t\,')}{\partial t'^2} = -4\pi \delta(\vec{r} - \vec{r}\,') \delta(t - t\,') \tag{B.9}$$

2. $G(\vec{r}, t; \vec{r}\,', t\,')$ must satisfy the boundary condition

$$\alpha \hat{n} \cdot \nabla' G(\vec{r}, t; \vec{r}\,', t\,') - \beta G(\vec{r}, t; \vec{r}\,', t\,') = 0 \tag{B.10}$$

for $\vec{r}\,'$ on the surface S and for all time $t\,'$ and α and β both constants.

3. $G(\vec{r},t;\vec{r}\,',t\,')$ must have reciprocity between the primed and unprimed coordinates.

$$G(\vec{r},t;\vec{r}\,',t\,') \equiv G(\vec{r}\,',t\,';\vec{r},t) \tag{B.11}$$

With the above conditions on $G(\vec{r},t;\vec{r}\,',t\,')$ met, $\psi(\vec{r},t)$ can be solved using

$$\begin{aligned}\psi(\vec{r},t) = &\iiiint_V G(\vec{r},t;\vec{r}\,',t\,')f(\vec{r}\,',t\,')dV'dt\,' \\ &+ \iiint_S (\psi(\vec{r}\,',t\,')\nabla' G(\vec{r},t;\vec{r}\,',t\,'))\cdot d\vec{S}\,'dt\,' \\ &- \iiint_S (G(\vec{r},t;\vec{r}\,',t\,')\nabla'\psi(\vec{r}\,',t\,'))\cdot d\vec{S}\,'dt\,'\end{aligned} \tag{B.12}$$

where the boundary is defined by V and S. For free space with sound speed c, the Green's function is

$$G(\vec{r},t;\vec{r}\,',t\,') = \frac{\delta(t-t\,'-R/c)}{R}. \tag{B.13}$$

where $R = |\vec{r}-\vec{r}\,'|$ is the distance between the source $\vec{r}\,'$ and the observation point $\vec{r}$.

Consider a point source located at the point $\vec{r}_O$ that sends an impulse at time t_O. The forcing term $f(\vec{r}\,',t\,')$ is given by

$$f(\vec{r}\,',t\,') = A\delta(\vec{r}\,'-\vec{r}_O)\delta(t\,'-t_O). \tag{B.14}$$

Setting the bounding surface to infinity and setting both the boundary condition on $\psi(\vec{r}\,',t\,')$ and its normal derivative to zero at infinity, we have using the Green's function Eq. (B.13) in Eq. (B.12)

$$\begin{aligned}\psi(\vec{r},t) &= \iiiint_V G(\vec{r},t;\vec{r}\,',t\,')f(\vec{r}\,',t\,')dV'dt\,' \\ \Longrightarrow &\iiiint_V \frac{\delta(t-t\,'-\frac{|\vec{r}-\vec{r}\,'|}{c})}{|\vec{r}-\vec{r}\,'|}A\delta(\vec{r}\,'-\vec{r}_O)\delta(t\,'-t_O)dV'dt\,'.\end{aligned} \tag{B.15}$$

The above integration give the final form of $\psi(\vec{r},t)$ as

$$\psi(\vec{r},t) = A\frac{\delta(t-t\,'-|\vec{r}-\vec{r}_O|/c)}{|\vec{r}-\vec{r}_O|}. \tag{B.16}$$

B.2 Interactions With Boundaries

In general, any acoustic wave will encounter a boundary. The simplest boundary is smooth, homogeneous, and infinite such as in Fig. 2.1 separating two regions that can be either fluid or solid. Two configurations discussed in this work are fluid-fluid and fluid-solid.

B.2.1 Boundary Conditions

In the case of a fluid-fluid interface, the boundary conditions are:

1. Normal component of velocity is continuous across the boundary.
2. Pressure is continuous across the boundary.

While for the fluid-solid interface the conditions are:

1. Normal component of velocity is continuous across the boundary.
2. Normal component of stress tensor is continuous across the boundary. This is nothing more than the pressure condition.
3. Tangential component of the stress tensor is zero at the boundary. The shear forces go to zero since ideal fluids have no viscous effects.

B.2.2 Fluid-Solid Interface

The fluid-fluid model is used to describe sound propagation in the underwater sound channel (USC). It is also used to describe sound propagation within the first few meters of the ocean floor. The reason is that the ocean floor can be treated as a fluid that the sediments that make up the ocean floor do not behave exactly like a true solid. However, for completeness and to demonstrate why the fluid-fluid approach is used in this study, we will solve the case of a fluid-solid interface. Solids experience both stressses (forces acting normal to the surface, pressures) and strains

(forces acting tangential to the surface, shear forces) [34]. As a result, there are two modes of waves propagating in a solid with two different sound speeds. Ocean sediments to exhibit this behavior, but the difference in the two sound speeds is on the order of a magnitude (see Tab. B.1).

Since the solid will respond to small perturbations elastically, Hooke's law applies in three dimensions giving the strain tensor of the solid

$$T_{ij} = -\lambda\delta_{ij}\nabla\cdot\vec{u} - \mu\left(\frac{\partial u_i}{\partial x_j} + \frac{\partial u_j}{\partial x_i}\right) \tag{B.17}$$

where $\vec{u}$ is the displacement vector. The negative signs are the result of Hooke's law in the solid stating that the solid will respond to the forces so as to return to its original state. The constant λ is the Lamé constant and μ is the rigidity of the solid. The Lamé constant can be thought of as a spring constant between a mass point in the solid and its next nearest neighbors and μ can be thought of as related to the torques about the mass point. Stress and strain disturbances propagate at different speeds within the solid with the speed of propagation of these disturbances given by

$$c_L^2 = \frac{\lambda + 2\mu}{\rho} \qquad c_T^2 = \frac{\mu}{\rho} \tag{B.18}$$

where c_L is the stress (longitudinal) sound speed and c_T is the shear (transverse) sound speed [40]. In nearly every solid c_L is 3 to 10 times larger than c_T and as a result, the transverse waves tend to be ignored in many theories including the present work. However, for completeness of this part, it is included here and ignored for the time reversal theory.

The longitudinal wave is described by a scalar velocity potential, ϕ, while the transverse wave needs to be described by a vector velocity potential $\vec{\psi}$. So the velocity of the wave is described by

$$\vec{v}(\vec{r},t) = \nabla\phi(\vec{r},t) + \nabla\times\vec{\psi}(\vec{r},t). \tag{B.19}$$

Mathematically, this is equivalent to the scalar potential describing the electric field and the vector potential describing the magnetic field in electrodynamics [42].

It is instructive to compare the results of the solid-fluid interface with the fluid-fluid interface. To start, we will derive the reflected and transmitted potentials of a point source located at $\vec{r}_O$ in the fluid medium transmitting an impulse with velocity given by $\vec{v}_1 = \nabla\phi_1$. The second medium is a solid with a velocity given by $\vec{v}_2 + \nabla\phi_2 + \nabla \times \vec{\psi}_2$. To make this problem more tractable, we will set $\vec{\psi}_2 = \psi_2\hat{y}$ using Cartesian coordinates. We set potential in the fluid medium as

$$\phi_1(\vec{r},t) = \frac{A\delta\left(t - t_O - \frac{\sqrt{(x-x_O)^2+(z-z_O)^2}}{c_1}\right)}{\sqrt{(x-x_O)^2+(z-z_O)^2}} + \frac{A\mathfrak{R}\delta\left(t - t_O - \frac{\sqrt{(x-x_O)^2+(z+z_O)^2}}{c_1}\right)}{\sqrt{(x-x_O)^2+(z+z_O)^2}} \tag{B.20}$$

where c_1 is the sound speed in the fluid and $\mathfrak{R}$ is the reflection coefficient for the interface. For the solid medium, we set the scalar and vector potentials as

$$\phi_2(\vec{r},t) = \frac{B\delta\left(t - t_O - \frac{\sqrt{(x-x_L)^2+(z-z_L)^2}}{c_L}\right)}{\sqrt{(x-x_L)^2+(z-z_L)^2}} \tag{B.21}$$

$$\psi_2(\vec{r},t) = \frac{D\delta\left(t - t_O - \frac{\sqrt{(x-x_T)^2+(z-z_T)^2}}{c_T}\right)}{\sqrt{(x-x_T)^2+(z-z_T)^2}} \tag{B.22}$$

where the subscripts L and T correspond to longitudinal and transverse waves respectively. Also notice that in the both Eqs. (B.21) and (B.22) that the location of the image sources for the two separate modes are treated as if the waves originate from two different locations which is a result of the two different sound speeds c_L and c_T. Recall the boundary conditions for this problem:

- Normal component of velocity is continuous across the boundary.
- Normal component of stress tensor is continuous across the boundary. This is nothing more than the pressure condition.
- Tangential component of the stress tensor is zero at the boundary. The shear forces go to zero since ideal fluids have no viscous effects.

We shall approach each in turn. First, consider causality at the surface of the boundary. This enforces that no matter how far away the real and image sources are from the boundary, the signal from all the sources must be at the boundary at one time. This results in setting the terms in the delta functions of Eqs. (B.20), (B.21) and (B.22) equal at the boundary giving us:

$$\sqrt{(x-x_L)^2+z_L^2} = \left(\frac{c_L}{c_1}\right)\sqrt{(x-x_O)^2+z_O^2} \tag{B.23}$$

$$\sqrt{(x-x_T)^2+z_T^2} = \left(\frac{c_T}{c_1}\right)\sqrt{(x-x_O)^2+z_O^2} \tag{B.24}$$

for the location of the image sources in terms of the real source.

Causality and Geometry

To gain insight into the causality condition, consider Fig. B.1. The source point labeled P is in the fluid medium with sound speed c_1 while the image point labeled L is in the solid medium with sound speed c_L. The point L corresponds to the source of the longitudinal waves seen by the observer at point $\vec{r}$. We can treat the longitudinal waves separate from the transverse waves since they are orthogonal modes in the solid. This treatment also works with the transverse waves. At the point labeled X the signals from P and L must arrive at the same time from the causality condition stated above. The sine of the angles γ_O and γ_L are given by

$$\sin\gamma_O = \frac{x-x_O}{\sqrt{(x-x_O)^2+z_O^2}} \qquad \sin\gamma_L = \frac{x-x_L}{\sqrt{(x-x_L)^2+z_L^2}}. \tag{B.25}$$

Multiplication and division of both by their respective sound speeds gives

$$\sin\gamma_O = \frac{x-x_O}{c_1}\frac{c_1}{\sqrt{(x-x_O)^2+z_O^2}} \qquad \sin\gamma_L = \frac{x-x_L}{c_L}\frac{c_L}{\sqrt{(x-x_L)^2+z_L^2}}. \tag{B.26}$$

Now isolate the ratio that is constant due to causality gives

$$\frac{c_1}{\sqrt{(x-x_O)^2+z_O^2}} = \frac{\sin\gamma_O}{(x-x_O)/c_1} \qquad \frac{c_L}{\sqrt{(x-x_L)^2+z_L^2}} = \frac{\sin\gamma_L}{(x-x_L)/c_L}. \tag{B.27}$$

Setting the two terms in Eq. (B.27) gives us the Snell's law relationship for each point x on the surface

$$\frac{\sin\gamma_O}{(x-x_O)/c_1} = \frac{\sin\gamma_L}{(x-x_L)/c_L}. \tag{B.28}$$

Using cosines gives a similar result

$$\frac{\cos\gamma_O}{z_O/c_1} = \frac{\cos\gamma_L}{z_L/c_L}. \tag{B.29}$$

Both Eqs. (B.28) and (B.29) also hold for the transverse waves in the solid. Now using the trigonometric identity $\cos^2\gamma + \sin^2\gamma = 1$, we find for γ_L in terms of γ_O

$$\begin{aligned} \cos^2\gamma_L + \sin^2\gamma_L &= 1 \\ \Rightarrow \left(\frac{c_1 z_L}{c_L z_O}\right)^2 \cos^2\gamma_O + \left(\frac{c_1(x-x_L)}{c_L(x-x_O)}\right)^2 \sin^2\gamma_O &= 1. \end{aligned} \tag{B.30}$$

The only way the last line above can be true is if both the coefficients in front of the cosine and sine terms equal 1. As a result, we get these useful relationships.

$$\frac{z_L}{c_L} = \frac{z_O}{c_1} \qquad \frac{x-x_L}{c_L} = \frac{x-x_O}{c_1}. \tag{B.31}$$

Now we consider the normal component of velocity across the boundary. Using Cartesian coordinates we have on the boundary z = 0

$$\frac{\partial\phi_1}{\partial z} = \frac{\partial\phi_2}{\partial z} + \frac{\partial\psi_{2y}}{\partial x} - \frac{\partial\psi_{2x}}{\partial y}. \tag{B.32}$$

Using the potentials given in Eq. (B.20) through Eq. (B.22), the above reduces to

$$\frac{\partial\phi_1}{\partial z} = \frac{\partial\phi_2}{\partial z} + \frac{\partial\psi_2}{\partial x}. \tag{B.33}$$

The derivatives of each are

$$\frac{\partial\phi_1}{\partial z} = \frac{A(1-\Re)z_O}{((x-x_O)^2+z_O^2)^{3/2}}, \tag{B.34}$$

$$\frac{\partial\phi_2}{\partial z} = \frac{Bz_L}{((x-x_L)^2+z_L^2)^{3/2}}, \tag{B.35}$$

and

$$\frac{\partial \psi_2}{\partial x} = \frac{-D(x - x_T)}{((x - x_T)^2 + z_T^2)^{3/2}}. \tag{B.36}$$

Using the causality condition results in

$$\frac{A(1 - \Re)\cos\gamma_O}{c_1^2} = \frac{B\cos\gamma_L}{c_L^2} - \frac{D\sin\gamma_T}{c_T^2} \tag{B.37}$$

$$A(1 - \Re) = B\left(\frac{c_1}{c_L}\right)^2 - D\left(\frac{c_1}{c_T}\right)^2 \tan\gamma_O \tag{B.38}$$

Where we used

$$\cos\gamma_i = \frac{z_i}{\sqrt{(x - x_i)^2 + z_i^2}} \tag{B.39}$$

and

$$\sin\gamma_i = \frac{x - x_i}{\sqrt{(x - x_i)^2 + z_i^2}} \tag{B.40}$$

for i equal to O, L, or T. And we used the relations (B.31) to go from Eq. (B.37) to Eq. (B.38).

Next we shall consider the normal component of the stress tensor. In order to set this condition, we need to take the partial derivative of the stress tensor with respect to time which writes Eq. (B.17) as

$$\frac{\partial T_{ij}}{\partial t} = -\lambda\delta_{ij}\nabla\cdot\vec{v} - \mu\left(\frac{\partial v_i}{\partial x_j} + \frac{\partial v_j}{\partial x_i}\right). \tag{B.41}$$

So the condition on normal T_{ij} in Cartesian coordinates with normal along positive z axis becomes

$$\lambda_1\nabla^2\phi_1 = \lambda_2\nabla^2\phi_2 + 2\mu_2\frac{\partial}{\partial z}\left(\frac{\partial\phi_2}{\partial z} + \frac{\partial\psi_{2y}}{\partial x} - \frac{\partial\psi_{2x}}{\partial y}\right). \tag{B.42}$$

Notice that the only place where the vector potential exists is in the term multiplied by μ_2. The coefficients 1 and 2 correspond to the fluid and solid half spaces respectively. For the specific potentials from Eqs. (B.20), (B.21), and (B.22); Eq. (B.42) reduces to on the z = 0 plane

$$\lambda_1\nabla^2\phi_1 = \lambda_2\nabla^2\phi_2 + 2\mu_2\frac{\partial^2\phi_2}{\partial z^2} + 2\mu_2\frac{\partial^2\psi_2}{\partial z\partial x}. \tag{B.43}$$

The derivatives are

$$\nabla^2\phi_1 = \frac{A(1+\mathfrak{R})}{((x-x_O)^2+z_O^2)^{3/2}} \tag{B.44}$$

$$\nabla^2\phi_2 = \frac{B}{((x-x_L)^2+z_L^2)^{3/2}} \tag{B.45}$$

$$\frac{\partial^2\phi_2}{\partial z^2} = \frac{B(3\cos^2\gamma_L - 1)}{((x-x_L)^2+z_L^2)^{3/2}} \tag{B.46}$$

$$\frac{\partial^2\psi_2}{\partial z\partial x} = \frac{-3D\cos\gamma_T\sin\gamma_T}{((x-x_T)^2+z_T^2)^{5/2}} \tag{B.47}$$

where we have used the definition of γ_i. Putting Eqs. (B.44) through (B.47) into Eq. (B.43) gives

$$\begin{aligned} \frac{\lambda_1(1+\mathfrak{R})A}{c_1^3} &= \frac{B[\lambda_2+2\mu_2(3\cos^2\gamma_L-1)]}{c_L^3} - \frac{3\mu_2 D\sin(2\gamma_T)}{c_T^3} \\ \Rightarrow \frac{\lambda_1(1+\mathfrak{R})A}{c_1^3} &= \frac{B[\lambda_2+2\mu_2(3\cos^2\gamma_O-1)]}{c_L^3} - \frac{3\mu_2 D\sin(2\gamma_O)}{c_T^3} \end{aligned} \tag{B.48}$$

where we have used the causality condition and Eq. (B.31).

The continuity of the tangential component of the stress tensor, we have in the solid in Cartesian coordinates is

$$\frac{\partial v_z}{\partial x} + \frac{\partial v_x}{\partial z} = 0 \tag{B.49}$$

where we have already set $\frac{\partial\vec{u}}{\partial t} = \vec{v}$. Using the general geometry described in this section, the above reduces to

$$2\frac{\partial^2\phi_2}{\partial z\partial x} + \frac{\partial^2\psi_2}{\partial x^2} - \frac{\partial^2\psi_2}{\partial z^2} = 0 \tag{B.50}$$

Using the potentials in the solid given by Eqs. (B.21) and (B.22), the derivatives are:

$$\frac{\partial^2\phi_2}{\partial z\partial z} = \frac{-3B\sin\gamma_L\cos\gamma_L}{((x-x_L)^2+z_L^2)^{3/2}} \tag{B.51}$$

$$\frac{\partial^2\psi_2}{\partial x^2} = \frac{D[3\sin^2\gamma_T - 1]}{((x-x_T)^2+z_T^2)^{3/2}} \tag{B.52}$$

$$\frac{\partial^2\psi_2}{\partial z^2} = \frac{D[3\cos^2\gamma_T - 1]}{((x-x_T)^2+z_T^2)^{3/2}} \tag{B.53}$$

Combining Eqs. (B.51) through (B.53) into Eq. (B.50) gives

$$D = -B\left(\frac{c_T}{c_L}\right)^3 \frac{\sin(2\gamma_L)}{\cos(2\gamma_T)}$$
$$\Rightarrow D = -B\left(\frac{c_T}{c_L}\right)^3 \tan(2\gamma_O). \tag{B.54}$$

Using Eq. (B.54) in Eq. (B.37) results in

$$\frac{A(1-\Re)\cos\gamma_O}{c_1^2} = \frac{B\cos\gamma_L}{c_L^2} - B\left(\frac{c_T}{c_L}\right)^3 \frac{\sin(2\gamma_L)}{\cos(2\gamma_T)}\frac{\sin\gamma_T}{c_T^2} \tag{B.55}$$

which reduces to

$$B = \frac{A(1-\Re)c_L^3\cos\gamma_O\cos(2\gamma_T)}{c_1^2[c_L\cos(2\gamma_T)\cos\gamma_L + c_T\sin\gamma_T\sin(2\gamma_L)]} \tag{B.56}$$
$$\Rightarrow B = A(1-\Re)\left(\frac{c_L}{c_1}\right)^2 \frac{c_L\cos(2\gamma_O)}{c_L + 2(c_T - c_L)\sin^2\gamma_O}. \tag{B.57}$$

This is the amplitude of the longitudinal field in the solid. Using Eq. (B.56) in Eq. (B.54) gives

$$D = -\frac{A(1-\Re)c_T^3\cos\gamma_O\sin(2\gamma_L)}{c_1^2[c_L\cos(2\gamma_T)\cos\gamma_L + c_T\sin\gamma_T\sin(2\gamma_L)]} \tag{B.58}$$

or using Eq. (B.31) gives

$$D = -A(1-\Re)\left(\frac{c_T}{c_1}\right)^2 \frac{c_T\sin(2\gamma_O)}{c_L + 2(c_T - c_L)\sin^2\gamma_O}. \tag{B.59}$$

Rewriting Eqs. (B.56) and (B.58) gives

$$B = \beta c_L^3\cos(2\gamma_T) \tag{B.60}$$
$$D = -\beta c_T^3\sin(2\gamma_L) \tag{B.61}$$

where

$$\beta = \frac{A(1-\Re)\cos\gamma_O}{c_1^2[c_L\cos(2\gamma_T)\cos\gamma_L + c_T\sin\gamma_T\sin(2\gamma_L)]}. \tag{B.62}$$

Or using Eq. (B.57) and Eq. (B.59) gives

$$B = \beta c_L^3\cos(2\gamma_O) \tag{B.63}$$
$$D = -\beta c_T^3\sin(2\gamma_O) \tag{B.64}$$

where

$$\beta = \frac{A(1-\Re)}{c_1^2[c_L + 2(c_T - c_L)\sin^2\gamma_O]}. \tag{B.65}$$

Inserting Eqs. (B.63) and (B.64) into Eqs. (B.21) and (B.22) gives the total potential in the solid as

$$\phi_2(\vec{r},t) = \beta c_1 c_L^2 \cos(2\gamma_O)\frac{\delta\left(t - t_O - \frac{\sqrt{(x-x_O)^2+(z-z_O)^2}}{c_1}\right)}{\sqrt{(x-x_O)^2+(z-z_O)^2}} \tag{B.66}$$

and

$$\psi_2(\vec{r},t) = -\beta c_1 c_T^2 \sin(2\gamma_O)\frac{\delta\left(t - t_O - \frac{\sqrt{(x-x_O)^2+(z-z_O)^2}}{c_1}\right)}{\sqrt{(x-x_O)^2+(z-z_O)^2}} \tag{B.67}$$

using Eq. (B.65) for β.

Analysis of B and D

Using Eqs. (B.63) and (B.64), there are a few interesting behaviors. When the angle γ_O is equal to zero,there are only longitudinal waves in the solid. As the angle of incidence increases, the longitudinal waves decrease in amplitude and the transverse waves increase in amplitude. This continues until the angle of incidence increases to 45° which at that point the waves in the solid are purely transverse.

The ratio D/B is given by

$$\frac{D}{B} = -\left(\frac{c_T}{c_L}\right)^3 \tan(2\gamma_O). \tag{B.68}$$

To keep this ratio as close to zero as possible, a small angle is required which means setting γ_O to near normal incidence, we can treat the solid as fluid-like. Note that c_T/c_L is always smaller than 1, for most metals it is less than 0.75 and is less than 0.5 for most polymers. Consider a stainless steel sphere, c_L for 347 stainless steel is 5790 m/s and c_T is 3100 m/s [41] resulting in $|D| \leq |B|0.044\tan(2\theta_S)$. Now consider a more geologically realistic second medium such as clay, sand or silt, the sound speeds are given in table B.1 [5] and [41]. Since $(c_T/c_L)^5$ is much less than one, it will be acceptable to ignore the shear waves in all calculations involving geologic sediments.

Table B.1: The sound speeds below are given in m/s. It should be noted that c_T for both sand and silt are functions of depth as c $\tilde{z}^{0.3}$ where $\tilde{z}$ is the depth and c is the sound speed constant.

Material	c_L	c_T	$(c_T/c_L)^5$
clay	1500	< 100	1.32×10^{-6}
sand (1m)	1650	110	1.32×10^{-6}
silt (1m)	1575	80	3.38×10^{-7}
Cast Iron	4994	2809	5.63×10^{-2}
347 Stainless Steel	5790	3100	4.40×10^{-2}
Rolled Copper	5010	2270	1.90×10^{-2}

B.3 Figures

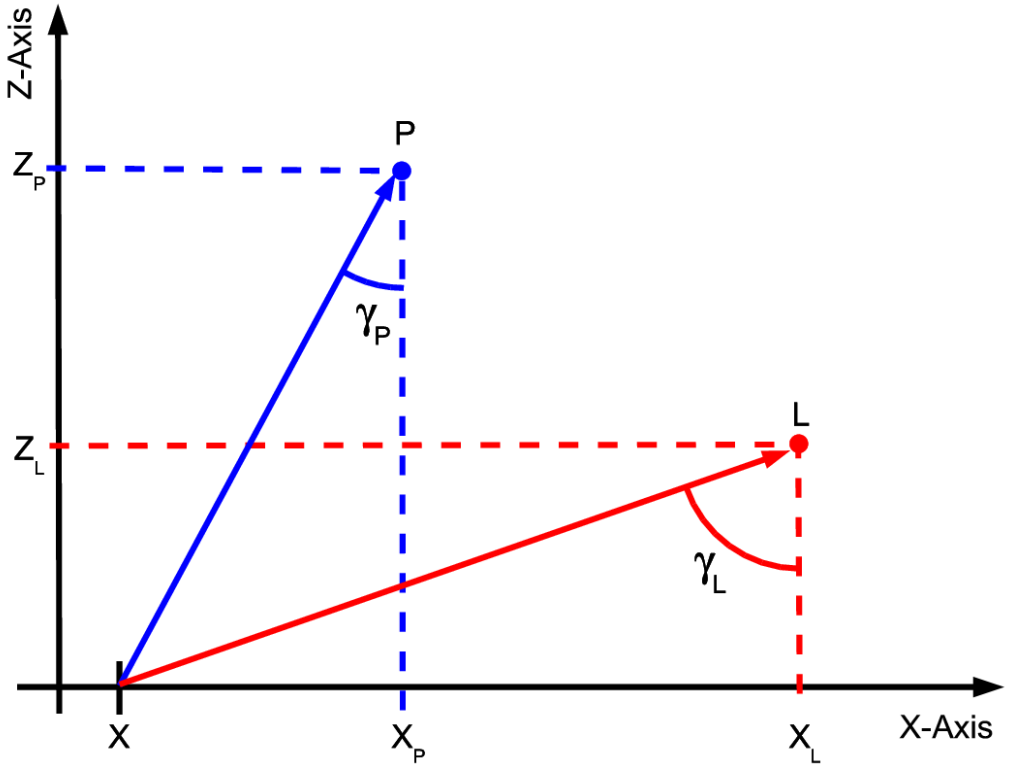

Figure B.1: Justification of the use of a "Snell's law" relation follows from the boundary geometry. The point P is the source in medium 1 with sound speed c_1 and point L is the image in medium 2 with sound speed c_L. Because of causality the signal at X from both P and L must arrive at the same time. As a result the median time of travel between X and either point must be the same when multiplied by the appropriate sound speed.